

# LLE Review

## Quarterly Report



**January–March 1993**

Laboratory for Laser Energetics  
College of Engineering and Applied Science  
University of Rochester  
250 East River Road  
Rochester, New York 14623-1299



# LLE Review

## Quarterly Report

*Editor:* D. D. Meyerhofer  
(716) 275-0255

**January–March 1993**

---

Laboratory for Laser Energetics  
College of Engineering and Applied Science  
University of Rochester  
250 East River Road  
Rochester, New York 14623-1299



This report was prepared as an account of work conducted by the Laboratory for Laser Energetics and sponsored by New York State Energy Research and Development Authority, the University of Rochester, the U.S. Department of Energy, and other agencies.

Neither the above named sponsors, nor any of their employees, makes any warranty, expressed or implied, or assumes any legal liability or responsibility for the accuracy, completeness, or usefulness of any information, apparatus, product, or process disclosed, or represents that its use would not infringe privately owned rights.

Reference herein to any specific commercial product, process, or service by trade name, mark, manufacturer, or otherwise, does not necessarily constitute or imply its endorsement, recommendation, or favoring by the United States Government or any agency thereof or any other sponsor.

Results reported in the LLE Review should not be taken as necessarily final results as they represent active research. The views and opinions of authors expressed herein do not necessarily state or reflect those of any of the above sponsoring entities.

## IN BRIEF

This volume of the LLE Review covers the three-month period January–March 1993. The OMEGA laser facility was decommissioned during this quarter to make room for the OMEGA Upgrade laser facility. The decommissioning is described in this volume. Electron thermal transport in the corona and laser-irradiation uniformity are related issues for direct-drive laser fusion. Thermal transport can affect the laser-irradiation uniformity requirements. The status of Fokker-Planck modeling of electron transport at LLE is reviewed and is followed by a description of a new technique for achieving high laser uniformity using zero-correlation phase masks. The use of fast, optically triggered, superconducting opening switches can, in principle, reduce the peak electrical load requirements of systems like the OMEGA Upgrade. Recent research in this area is described. The last three articles discuss vacuum ultraviolet and x-ray emission from short-pulse, laser-matter interactions. The generation of a high spectral brightness, picosecond  $K_{\alpha}$  source is described. The subsequent articles describe the generation of high-order harmonics of a high-intensity laser system in low-density, laser-atom interactions and the novel gas target used.

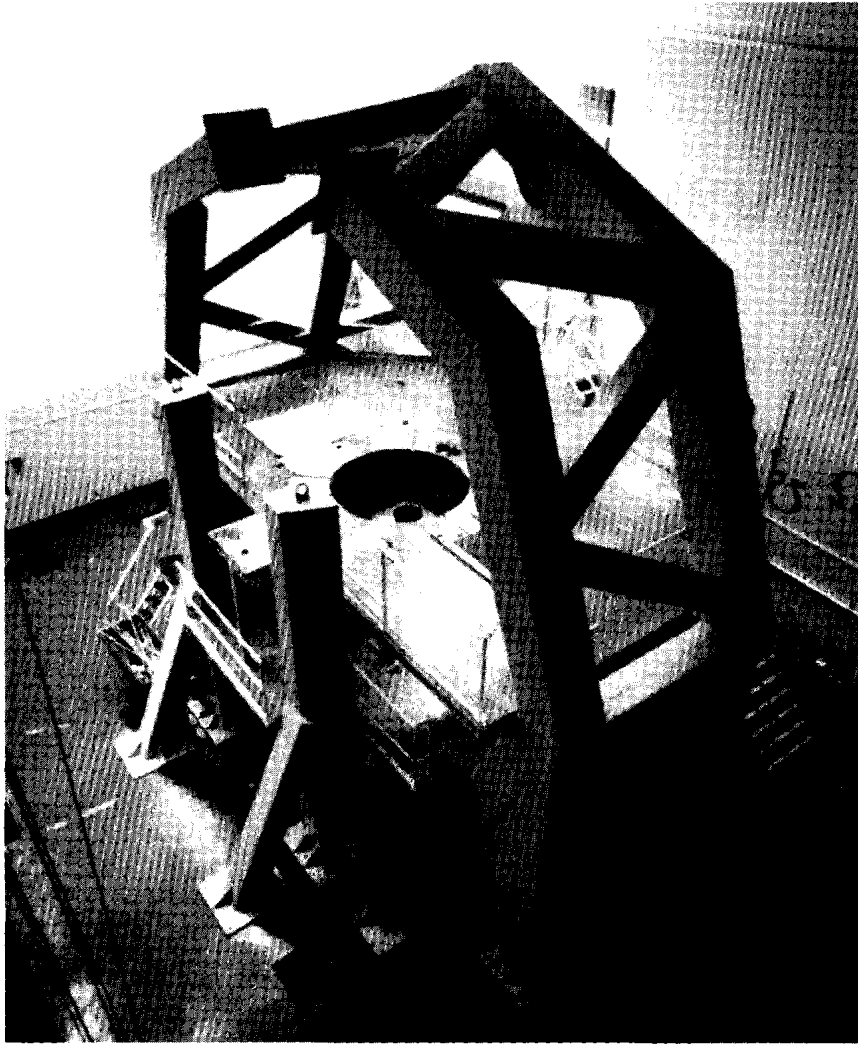
Highlights of the research reported in this issue include

- The *SPARK* Fokker-Planck code is described in detail. It incorporates fluid ions and solves for transport on either a two-dimensional (2-D) Eulerian grid or a one-dimensional (1-D) Lagrangian grid. Simulations of a laser-driven CH foil in 1-D planar geometry and of laser filamentation in a 2-D planar plasma are presented.

- Phase plates have been used in laser fusion to produce a well-defined, far-field intensity envelope that is relatively independent of the input-beam profile. Superposed on this envelope is unwanted, highly modulated speckle from the interference of the different phase-plate elements. A technique for choosing the phase-plate elements (in combination with polarization rotation) such that these intensity fluctuations approach zero in the limit of plane-wave, near-field irradiation is presented.
- High- $T_c$ , superconducting thin films are used in a new type of opening switch. The superconducting film screens the magnetic flux linkage between the primary and secondary coils of a transformer. Short laser pulses are used to trigger the transition of the superconductor to its normal state, allowing the flux produced in the primary current to couple to the secondary. Experiments have confirmed the feasibility of this inductively coupled switch, and rise times of 50 ns have been observed for the secondary voltage pulse.
- Strong  $K_\alpha$  emission is observed from a plasma produced by a high-intensity-contrast, picosecond, p-polarized laser pulse. The  $K_\alpha$  emission is found to be induced by hot electrons having a temperature of around 5 keV and carrying up to 20% of the laser energy.
- The angular distributions of high-order harmonics generated in low-density gas targets of Xe, Kr, and Ar have been measured. In this experiment, the phase-matching effects are minimized. It is found that most of the harmonic angular distributions show a central region similar to that predicted by lowest-order perturbation theory.
- A thin (1-mm), low-pressure (<1-T) gas target for high-order, harmonic-generation experiments has been developed. It operates on the principle of free molecular flow rather than the principle of viscous flow, as does a gas jet. The device is a small, cylindrical, double-ended hole through which the focused laser beam passes. Monte-Carlo simulations of the density and flow of the gas within the nozzle are in good agreement with the experimental measurements of the gas-density profile.

# CONTENTS

	<i>Page</i>
IN BRIEF .....	iii
CONTENTS .....	v
Section 1 OMEGA DECOMMISSIONING .....	61
Section 2 ADVANCED TECHNOLOGY DEVELOPMENTS .....	63
2.A Fokker-Planck Modeling of Electron Transport .....	63
2.B Strategies for Ultra-High Laser Uniformity Using Zero-Correlation Phase Masks .....	77
2.C Fast, Optically Triggered, Superconducting Opening Switches .....	86
2.D Strong $K_{\alpha}$ Emission in Picosecond Laser-Plasma Interactions .....	91
2.E Angular Distribution of High-Order Harmonics from Low-Density Gas Targets .....	100
2.F Novel Gas Target for Use in Laser Harmonic Generation .....	109
PUBLICATIONS AND CONFERENCE PRESENTATIONS	



The OMEGA laser system was decommissioned during January–March 1993. The cover photographs show the laser bay before (left) and near the end of the decommissioning. The above photograph shows the target mirror structure after the vacuum chamber and diagnostics were removed. The structure was subsequently disassembled.

# Section 1

## OMEGA Decommissioning

On 18 December 1992 the final shot was fired on the OMEGA laser system. OMEGA was then decommissioned during the first quarter of 1993 to make room for the OMEGA Upgrade.<sup>1</sup> The decommissioning task was completed on 10 February 1993, several weeks ahead of schedule.

The operational OMEGA system was surrounded by 15 years' worth of storage. Every area planned for use by the OMEGA Upgrade was occupied with experimental hardware, documentation storage, and spare parts. The first task was to establish a schedule for decommissioning that would be integrated with the facility modification plan. This task was estimated to take approximately 14 weeks. The second task was the selection of the team to execute the decommissioning plan. This team brought together the expertise of the operations group with the OMEGA Upgrade engineering team for each critical area to be decommissioned. The plan was generated and reviewed with the directors, team roles and responsibilities were outlined, tools and storage material were procured, storage areas were defined, and a rigging contractor was selected.

The concern for safety was always utmost in the planning and each task was evaluated to insure that the correct procedure was used and appropriate equipment handling was available.

The readiness planning paid off as the execution went well and safely, the teams were swift, and area by area was cleared and cleaned.

### **OMEGA Decommissioning**

The following is a summary of the structures, components, and miscellaneous material removed from the facility to make room for the OMEGA Upgrade:

- 250 skids (4 ft × 4 ft wooden pallets) each containing approximately 64 cu ft. of material weighing 500 pounds;
- Six dumpsters (30 cu yd.) for metal scrap;
- Ten dumpsters (30 cu yd.) for material scrap;
- 16,000 sq. ft. used for structures and components storage at the Center for Optoelectronics and Imaging and Boulter Carting Co.;
- 140,000 lb of structures for metal salvage.

Excluding the 140,000 lb of structures that were scrapped, the total volume of material stored or scrapped via dumpsters is equal to approximately 109,000 cu ft.

The material in storage was inventoried into the vault via the property-control process. Material and components intended for reuse in the OMEGA Upgrade design were assigned six-digit identification numbers that will be used to retrieve the hardware when required for assembly into the Upgrade program.

The early closure of the decommissioning allowed the facility contractor to start the internal building modifications at an early date, which in turn will enhance the overall OMEGA Upgrade schedule. The excellent effort put forth by the decommissioning team coupled with the cooperative spirit of all the LLE staff was key to the success of this effort.

The preparation and planning for the integration of the OMEGA Upgrade system is now well underway. Building modifications are proceeding and supporting the start date for structures installation on 23 August 1993.

### **REFERENCES**

1. LLE Review **39**, 114 (1989).

## Section 2

# ADVANCED TECHNOLOGY DEVELOPMENTS

### 2.A Fokker-Planck Modeling of Electron Transport

Just over a decade ago Bell *et al.*<sup>1</sup> produced one of the first Fokker-Planck (FP) simulations of electron-energy transport in an idealized laser-produced plasma. As a result of improvements in numerical techniques and computational speeds available from modern computers, it is now possible to routinely run FP codes under conditions directly relevant to inertial confinement fusion (ICF).<sup>2-5</sup> The relevance of such simulations is that ICF plasmas can exhibit conditions where classical fluid transport theory<sup>6,7</sup> is inadequate.

Well-known manifestations of the breakdown of fluid theory occur in the presence of strong temperature gradients, where the Spitzer-Härm (SH) heat flow  $\mathbf{q}_{SH} = -\kappa_{SH}\nabla T$  ( $\kappa_{SH}$  being the SH thermal conductivity and  $T$  the electron temperature) overestimates the magnitude of the maximum heat flux and fails to predict the preheat caused by long-mean-free-path electrons ahead of the main heat front.<sup>1</sup> Although the first inadequacy can be overcome to some extent by limiting the heat flow to some fraction  $f$  of its “free-streaming” limit  $q_f$ ,<sup>8</sup> i.e.,  $\mathbf{q} = \mathbf{q}_{SH} / (1 + |\mathbf{q}_{SH}|/fq_f)$ , the second one can only be properly corrected by means of a nonlocal heat-transport model such as the FP equation.

A more subtle heat-flow reduction effect has also been shown to arise<sup>9</sup> even for arbitrarily small levels of heat flow (i.e.,  $|\mathbf{q}_{SH}| \ll fq_f$ ), provided that the characteristic wavelength of the temperature modulation is less than about  $200 \lambda_e$ , where  $\lambda_e$  is the delocalization length or mean free path of a thermal electron.<sup>3,10,11</sup> This phenomenon has been shown to have important consequences for laser filamentation instabilities,<sup>10</sup> as confirmed by recent simulations of experiments,<sup>4,12</sup> and to stimulated Brillouin scattering.<sup>13-15</sup>

This article addresses some of the computational issues involved in solving the FP equation. Particular emphasis will be given to the development of codes applicable to laser-fusion problems of the type previously mentioned. The FP equation is first introduced; the two-dimensional (2-D) electron FP code (*SPARK*) is described; this is followed by numerical simulations and a discussion of future directions.

### The Fokker-Planck Equation

The Fokker-Planck equation for Coulomb collisions between species  $a$  and  $b$  with respective distribution functions  $f_a(\mathbf{r}, \mathbf{v}, t)$  and  $f_b(\mathbf{r}, \mathbf{v}, t)$  can be written as<sup>16</sup>

$$\begin{aligned} \frac{\partial f_a}{\partial t} + \mathbf{v} \cdot \nabla f_a + \frac{Z_a e}{m_a} \mathbf{E} \cdot \nabla_{\mathbf{v}} f_a \\ = Y_{ab} \left[ -\nabla_{\mathbf{v}} \cdot (f_a \nabla_{\mathbf{v}} H_{ab}) + \frac{1}{2} \nabla_{\mathbf{v}} \nabla_{\mathbf{v}} : (f_a \nabla_{\mathbf{v}} \nabla_{\mathbf{v}} G_{ab}) \right], \quad (1) \\ + Y_{aa} \left[ -\nabla_{\mathbf{v}} \cdot (f_a \nabla_{\mathbf{v}} H_{aa}) + \frac{1}{2} \nabla_{\mathbf{v}} \nabla_{\mathbf{v}} : (f_a \nabla_{\mathbf{v}} \nabla_{\mathbf{v}} G_{aa}) \right], \end{aligned}$$

where

$$Y_{ab} = 4\pi \left( \frac{Z_a Z_b e^2}{m_a} \right)^2 \ln \Lambda, \quad (2)$$

$$H_{ab}(\mathbf{v}) = \frac{m_a + m_b}{m_b} \int \frac{f_b(\mathbf{v}')}{|\mathbf{v} - \mathbf{v}'|} d\mathbf{v}', \quad (3a)$$

and

$$G_{ab}(\mathbf{v}) = \int f_b(\mathbf{v}') |\mathbf{v} - \mathbf{v}'| d\mathbf{v}', \quad (3b)$$

where  $\nabla$  is the configuration space gradient operator,  $\nabla_{\mathbf{v}}$  is the velocity space gradient operator,  $\ln \Lambda$  is the Coulomb logarithm (for simplicity assumed to be the same for both particles),  $e$  is magnitude of the electronic charge,  $Z_a$  and  $Z_b$  are the respective charge numbers of particles  $a$  and  $b$ , and  $m_a$  and  $m_b$  are their respective masses. The left-hand side of Eq. (1) (usually known as the Vlasov part) represents the collisionless transport of particle  $a$  in the presence of an accelerating field  $Z_a e \mathbf{E} / m_a$ , but in the absence of magnetic field effects. The collisional term on the right-hand side of Eq. (1) assumes the dominance of small-angle scattering, which implies that  $\ln \Lambda \gg 1$ .

### The *SPARK* Code

The basic philosophy behind the *SPARK* code has been to provide an efficient and robust way of solving the FP equation.<sup>17,18</sup> Its main purpose has been to study nonlocal heat-transport problems of interest to ICF.

*SPARK* is not unlike a standard hydrodynamic code, in that it solves the fluid equation for the ions (mass and momentum conservation) and the energy equation for the electrons (neglecting ion-thermal effects). However, the latter is modeled by the FP equation instead of a fluid equation with SH heat flow.

Current versions of the code neglect the effects of magnetic fields and allow for one-dimensional (1-D) Lagrangian transport in planar, cylindrical, or spherical geometry, and 2-D Eulerian transport in either planar or cylindrical geometry. The 2-D version incorporates a paraxial wave-equation approach for laser light transport.<sup>12</sup> In all versions, the fluid-transport equations (with SH electron heat flow) are solved in parallel so as to assess the importance of kinetic effects and provide for an accuracy check of the FP code in the collisional limit.

### 1. Basic Equations

The electron FP equation solved in *SPARK* includes an inverse-bremsstrahlung heating source.<sup>19</sup> By defining the distribution function in the reference frame of the fluid ions (of velocity  $\mathbf{u}_i$ ), and using the expansion  $f = f_0 + \mathbf{v} \cdot \mathbf{f}_1 / v$ , Eq. (1) becomes

$$\begin{aligned}
 & \left( \frac{\partial}{\partial t} + \mathbf{u}_i \cdot \nabla \right) f_0 - (\nabla \cdot \mathbf{u}_i) \frac{v}{3} \frac{\partial f_0}{\partial v} = \nabla \cdot \left[ \chi (\nabla f_0 + \mathbf{a} \alpha f_0) \right] \\
 & \qquad \qquad \qquad (a) \qquad \qquad \qquad (b) \\
 & + \frac{1}{v^2} \frac{\partial}{\partial v} \left[ \chi \left( \mathbf{a} \cdot \mathbf{a} \frac{\partial f_0}{\partial v} + v \boldsymbol{\beta} \cdot \mathbf{a} f_0 \right) + Y_{ee} \left( C_0 f_0 + D_0 \frac{\partial f_0}{\partial v} \right) \right] \\
 & \qquad \qquad \qquad (c) \qquad \qquad \qquad (d) \\
 & + \left. \frac{n_e Z^* Y_{ee} v_0^2}{6v} \frac{\partial f_0}{\partial v} + \frac{H_{\text{vis}}}{v} \frac{\partial f_0}{\partial v} \right], \qquad \qquad \qquad (4) \\
 & \qquad \qquad \qquad (e) \qquad \qquad \qquad (f)
 \end{aligned}$$

where  $v_0$  is the electron oscillatory velocity in the laser field,  $\mathbf{a} = e\mathbf{E}/m_e$ ,  $\alpha = -(\partial_v \ln f_0)/v$ ,  $\boldsymbol{\beta} = -\nabla \ln f_0$ , and  $\chi = v^2/3v_{ei}^*$ . Here, we have introduced an effective  $e$ - $i$  collision frequency defined by  $v_{ei}^* = \phi 4\pi n_e Z^* (e^2/m_e)^2 \ln \Lambda / v^3$ , where  $Z^* = \langle Z^2 \rangle / \langle Z \rangle$  (with  $\langle \rangle$  denoting an average of the ion species), and  $\phi = (Z^* + 4.2)/(Z^* + 0.24)$  is a factor that gives rise to the ‘‘exact’’ SH heat flow (for arbitrary  $Z$ ) when  $f_0$  is a Maxwellian.<sup>3,20</sup> The terms in Eq. (4) can be identified as (a) hydrodynamic advection and compression, (b) electron transport in configuration space, (c) ohmic heating, (d)  $e$ - $e$  thermalization, (e) laser heating, and (f) heating caused by ion viscosity. The computational strategy for dealing with these various terms will be discussed.

Two important moments of Eq. (4) are the particle density moment  $\left( 4\pi \int dv v^2 \right)$

$$\left( \frac{\partial}{\partial t} + \mathbf{u}_i \cdot \nabla \right) n_e + n_e \nabla \cdot \mathbf{u}_i = 0, \qquad (5)$$

and the energy-density moment  $\left(2\pi m_e \int dvv^4\right)$

$$\left(\frac{\partial}{\partial t} + \mathbf{u}_i \cdot \nabla\right) \frac{3}{2} p + \frac{5}{2} p \nabla \cdot \mathbf{u}_i = -\nabla \cdot \mathbf{q} + s_{\text{ib}} + h_{\text{vis}} , \quad (6)$$

where  $n_e = 4\pi \int dvv^2 f_0$  is the electron number density,  $p = (4\pi/3) \int dvv^4 f_0$  is the electron pressure, and  $s_{\text{ib}}$  and  $h_{\text{vis}}$  are the respective inverse-bremsstrahlung and viscous heating. In deriving Eqs. (5) and (6) we have enforced quasi-neutrality by imposing zero current in the plasma. This condition allows us to calculate the electric field as follows:

$$\mathbf{a} = -\frac{\int dvv^2 \chi \nabla f_0}{\int dvv^2 \chi \alpha f_0} = -\frac{\int dvv^2 \chi \mathbf{B} f_0}{\int dvv \chi \frac{\partial f_0}{\partial v}} . \quad (7)$$

An alternative approach for calculating the electric field would be to adopt the implicit-moment method,<sup>21</sup> where one would use charge conservation and the Poisson equation to solve for  $\mathbf{E} = -\nabla \Phi$ . Although this method has been found to improve charge neutrality in FP calculations, it has only a negligible effect on the thermal transport results.<sup>17</sup>

Conservation of ion density and total momentum (assuming cold ions) is given by

$$\left(\frac{\partial}{\partial t} + \mathbf{u}_i \cdot \nabla\right) n_i + n_i \nabla \cdot \mathbf{u}_i = 0 \quad (8)$$

and

$$m_i n_i \left(\frac{\partial}{\partial t} + \mathbf{u}_i \cdot \nabla\right) \mathbf{u}_i = -\nabla(p + Q_{\text{vis}}) + \mathbf{P}_F , \quad (9)$$

respectively, where  $\mathbf{P}_F$  is the ponderomotive force and  $Q_{\text{vis}}$  is the artificial viscosity.<sup>22</sup>

## 2. The Alternating-Direction-Implicit (ADI) Method of Solution

The aim of the ADI method is to provide a time-implicit solution of a multidimensional differential equation by splitting it into 1-D equations,<sup>23,24</sup> which can then be efficiently solved. For a differential equation of the type

$$\frac{\partial f_0}{\partial t} = (F_x + F_y + F_v) f_0 , \quad (10)$$

where  $F_x$ ,  $F_y$ , and  $F_v$  are operators in  $x$ ,  $y$ , and  $v$ , the scheme becomes

$$(1 - \theta \Delta t F_x) (f_0^* - f_0^n) = \Delta t (F_x + F_y + F_v) f_0^n , \quad (11a)$$

$$(1 - \theta \Delta t F_y)(f_o^{**} - f_o^n) = (f_o^* - f_o^n), \quad (11b)$$

and

$$(1 - \theta \Delta t F_v)(f_o^{n+1} - f_o^n) = (f_o^{**} - f_o^n). \quad (11c)$$

Here we have differenced in time as  $\partial f / \partial t = (f^{n+1} - f^n) / \Delta t$  and introduced the implicitness parameter  $\theta$ , such that Eqs. (11a)–(11c) combined become accurate to  $O(\Delta t)^2$ , when  $\theta = 1/2$  (like the Crank-Nicolson scheme).

To put the FPEq. (4) into the form of Eq. (10), we first assume (without loss of generality) that the distribution  $f_o$  is a function of  $x$ ,  $y$ , and  $v$  and neglect the hydrodynamic contribution [term (a) in Eq. (4)]. Since the hydrodynamics usually evolves on a much longer time scale than the electron thermal transport, its contribution can be treated separately.

Next, we assume that operators  $F_x(f_o)$ ,  $F_y(f_o)$ , and  $F_v(f_o)$  are weak functions of  $f_o$ . To deal with the nonlinearities we may choose to (a) iterate at each time step by starting with  $F^n = F(f_o^n)$ ; (b) use a predictor step

$$F = F\left[f_o^n + \theta(f_o^n - f_o^{n-1})\right], \quad (12)$$

followed by iteration;<sup>17</sup> or (c) linearize the operator as follows:<sup>25</sup>

$$F^{n+1} = F^n + \left(\frac{\partial F}{\partial f_o}\right)^n (f_o^{n+1} - f_o^n) + O(\Delta t)^2. \quad (13)$$

The choice between these various options becomes particularly important when dealing with the  $e$ - $e$  thermalization [term (d), Eq. (4)], as will be discussed.

The remaining problem with Eq. (4) lies in the  $E$ -field terms. Not only are they nonlinear [see Eq. (7)], but they also involve mixed derivatives like  $\partial_x \partial_v f_o$ ,  $\partial_y \partial_v f_o$ , ... that cannot easily be incorporated into the ADI scheme. A way around this difficulty has been found by introducing the coefficients  $\alpha(f_o)$  and  $\beta(f_o)$  in Eq. (4), which are then treated as time invariant over a time step  $\Delta t$ .<sup>26</sup> With this transformation the FPEquation can be expressed in the form of Eq. (10), where  $F_x$ ,  $F_y$ , and  $F_v$  are convection-diffusion operators.

To difference Eq. (4) (in the 2-D Eulerian version of *SPARK*), the distribution function is defined on an orthogonal grid  $f_{j,k,l} = f_o(v_j, x_k, y_l)$ , where the indices  $j = 1, \dots, J$ ,  $k = 1, \dots, K$ , and  $l = 1, \dots, L$ , denote cell centers. The cell boundaries are defined by  $v_{j+1/2} = (v_j + v_{j+1})/2, \dots$ , and the cell sizes (not necessarily uniform) by  $\Delta v_j = (v_{j+1/2} - v_{j-1/2}), \dots$ . In the 1-D Lagrangian version, a mesh-centered grid is used in configuration space.<sup>27</sup>

### 3. Hydrodynamic Transport

Since the hydrodynamic evolution of the plasma is normally slow compared with the thermal-transport processes, we are able to solve the left-hand side of Eq. (4) separately. In the 2-D Eulerian version of *SPARK* we adopt a standard

donor-cell scheme<sup>22</sup> for the convective terms in Eqs. (4), (8), and (9) and set  $Q_{\text{vis}} = 0$ . (However, if one wishes to model sharp density gradients and shocks, a less-diffusive numerical scheme would be desirable.)

In the 1-D Lagrangian version, the fluid equations (8) and (9) are solved in the frame of the ions, by introducing the total derivative  $d/dt = (\partial/\partial t + \mathbf{u}_i \cdot \nabla)$ .<sup>22</sup> The left-hand side of Eq. (4) is solved in the form<sup>3</sup>

$$\frac{f_o^{n+1} - f_o^n}{\Delta t} + \frac{d(\ln n_i)}{dt} \left[ \frac{v}{3} \frac{\partial(\ln f_o^n)}{\partial v} \right] f_o^n = 0, \quad (14)$$

where we have made use of the continuity equation  $\nabla \cdot \mathbf{u}_i = -d(\ln n_i)/dt$ .

In both Eulerian and Lagrangian versions of the code the transformation  $\partial_v f_o = f_o \partial_v \ln f_o$  has been used, where  $[\partial_v \ln f_o]_j \approx [\ln(f_{j+1}/f_{j-1})]/2\Delta v_j$ . This formulation gives rise to zero truncation error for a Maxwellian and has been found to minimize departures from quasi-neutrality.

#### 4. Electron Transport in Configuration Space

The electron transport in configuration space [term (b) in Eq. (4)] is differenced in conservative form as follows:

$$\begin{aligned} & \nabla \cdot [\chi(\nabla f_o + \mathbf{a}\alpha f_o)]_{j,k,l} \\ &= \frac{1}{\Delta x_k} \left[ \chi_{k+1/2} \left( \frac{f_{k+1} - f_k}{\Delta x_{k+1/2}} + a_{x,k+1/2} \alpha_{k+1/2} f_{k+1/2} \right) \right. \\ & \quad \left. - \chi_{k-1/2} \left( \frac{f_k - f_{k-1}}{\Delta x_{k-1/2}} + a_{x,k-1/2} \alpha_{k-1/2} f_{k-1/2} \right) \right]_{j,l} \\ & \quad + \frac{1}{\Delta y_l} \left[ \chi_{l+1/2} \left( \frac{f_{l+1} - f_l}{\Delta y_{l+1/2}} + a_{y,l+1/2} \alpha_{l+1/2} f_{l+1/2} \right) \right. \\ & \quad \left. - \chi_{l-1/2} \left( \frac{f_l - f_{l-1}}{\Delta y_{l-1/2}} + a_{y,l-1/2} \alpha_{l-1/2} f_{l-1/2} \right) \right]_{j,k}. \end{aligned} \quad (15)$$

Here, the boundary values of  $f$  are calculated using an interpolation formula of type

$$f_{j,k+1/2,l} = (1 - \epsilon_{j,k+1/2,l}) f_{j,k+1,l} + \epsilon_{j,k+1/2,l} f_{j,k,l}, \quad (16)$$

(and similarly for  $f_{j,k,l+1/2}$ ), where

$$\varepsilon_{j,k+1/2,l} = \left[ 1 - \text{sign}(a_{x,k+1/2,l} \alpha_{x,k+1/2,l}) \right] / 2$$

ensures up-wind differencing for the convection term  $\nabla \cdot (\mathbf{a} \alpha f_0)$ .

The respective values of  $a_{x,k+1/2,l}$  and  $a_{x,k+1/2,l}$  are obtained from

$$a_{x,k+1/2,l} = - \frac{\sum_{j=1}^J \Delta v_j v_j^2 \chi_{j,k+1/2,l} (f_{k+1} - f_k)_{j,l} / \Delta x_{k+1/2}}{\sum_{j=1}^J \Delta v_j v_j^2 \chi_{j,k+1/2,l} \alpha_{j,k+1/2,l} f_{j,k+1/2,l}} \quad (17)$$

[using Eq. (7)] and

$$\alpha_{j,k+1/2,l} = - \frac{1}{2v_j \Delta v_j} \ln \left( \frac{f_{j+1}}{f_{j-1}} \right)_{k+1/2,l}. \quad (18)$$

### 5. *e-e* Thermalization

In the absence of thermal transport and external heating, the usual time-implicit difference version of Eq. (4) is<sup>28</sup>

$$\begin{aligned} \frac{f_j^{n+1} - f_j^n}{\Delta t} = & \frac{Y_{ee}}{\Delta v_j v_j^2} \left[ C_{j+1/2} f_{j+1/2}^{n+1} - C_{j-1/2} f_{j-1/2}^{n+1} \right. \\ & \left. + \frac{D_{j+1/2}}{\Delta v_{j+1/2}} (f_{j+1}^{n+1} - f_j^{n+1}) - \frac{D_{j-1/2}}{\Delta v_{j-1/2}} (f_j^{n+1} - f_{j-1}^{n+1}) \right], \quad (19) \end{aligned}$$

which, with the appropriate boundary conditions, conserves particle numbers exactly. Following the Chang-Cooper method,<sup>28</sup> we use

$$f_{j+1/2} = (1 - \delta_{j+1/2}) f_{j+1} + \delta_{j+1/2} f_j, \quad (20)$$

where

$$\delta_{j+1/2} = \frac{1}{w_{j+1/2}} - \frac{1}{\exp(w_{j+1/2}) - 1} \quad (21)$$

and  $w_{j+1/2} = \Delta v_{j+1/2} C_{j+1/2} / D_{j+1/2}$ . This type of weighting has been designed to preserve positivity and provide the correct equilibrium solution for  $f_0$ .

In order to conserve energy, the  $\Sigma(\Delta v_j v_j^4)$  sum of the right-hand side of Eq. (19) has to vanish. Langdon<sup>29</sup> has shown, through integration by parts, that this can be achieved by calculating the collisional terms as follows:

$$C_{j+1/2} = 4\pi \sum_{i=1}^j (\Delta v v^2 f)_i, \quad (22a)$$

$$(vD)_{j+1/2} = (vD)_{j-1/2} + (\Delta v v^2)_j 4\pi \sum_{i=j}^{J-1} (vf)_{i+1/2} \Delta v_{i+1/2}, \quad (22b)$$

and

$$(vD)_{3/2} = (\Delta v v^2)_1 4\pi \sum_{i=1}^{J-1} (vf)_{i+1/2} \Delta v_{i+1/2}. \quad (22c)$$

This method of solution implicitly assumes that  $C$  and  $D$  are slowly varying functions of time, so they can be calculated iteratively over one time step. However, when the plasma is far from equilibrium and one wishes to use time steps larger than the thermalization time  $\tau_{ee}$ , energy conservation may require too many iterations. One possible solution to this problem is to use a predictor-corrector scheme, whereby one starts the iteration by linearly extrapolating the distribution function from the  $n$  and  $(n-1)$  time levels to the  $(n+1)$  level.<sup>17</sup> An alternative approach is to linearize the full collision operator [Eq. (13)], so that Eq. (19) becomes

$$\begin{aligned} \frac{f_j^{n+1} - f_j^n}{\Delta t} &= \frac{Y_{ee}}{\Delta v_j v_j^2} \left[ C_{j+1/2}^n f_{j+1/2}^{n+1} - C_{j-1/2}^n f_{j-1/2}^{n+1} \right. \\ &\quad \left. + \frac{D_{j+1/2}^n}{\Delta v_{j+1/2}} (f_{j+1}^{n+1} - f_j^{n+1}) - \frac{D_{j-1/2}^n}{\Delta v_{j-1/2}} (f_j^{n+1} - f_{j-1}^{n+1}) \right] \\ &\quad + \frac{Y_{ee}}{\Delta v_j v_j^2} \left[ C_{j+1/2}^{n+1} f_{j+1/2}^n - C_{j-1/2}^{n+1} f_{j-1/2}^n \right. \\ &\quad \left. + \frac{D_{j+1/2}^{n+1}}{\Delta v_{j+1/2}} (f_{j+1}^n - f_j^n) - \frac{D_{j-1/2}^{n+1}}{\Delta v_{j-1/2}} (f_j^n - f_{j-1}^n) \right] \\ &\quad - \frac{Y_{ee}}{\Delta v_j v_j^2} \left[ C_{j+1/2}^n f_{j+1/2}^n - C_{j-1/2}^n f_{j-1/2}^n \right. \\ &\quad \left. + \frac{D_{j+1/2}^n}{\Delta v_{j+1/2}} (f_{j+1}^n - f_j^n) - \frac{D_{j-1/2}^n}{\Delta v_{j-1/2}} (f_j^n - f_{j-1}^n) \right], \quad (19a) \end{aligned}$$

where the right-hand side of the equation is now a full matrix operator [instead of the tridiagonal matrix in Eq. (19)]. Although a tridiagonal matrix can be more efficiently inverted than a full matrix, there are circumstances when, as a result of time-step constraints, the overall computational effort can be less for Eq. (19a) than Eq. (19).

## 6. Ohmic Heating

The ohmic-heating term [term (c) in Eq. (4)] is differenced in conservative form as follows:

$$\begin{aligned}
 & \frac{1}{v^2} \frac{\partial}{\partial v} \left[ \chi \left( \mathbf{a} \cdot \mathbf{a} \frac{\partial f_0}{\partial v} + v \boldsymbol{\beta} \cdot \mathbf{a} f_0 \right) \right]_{j,k,l} \\
 &= \frac{1}{\Delta v_j v_j^2} \left\{ \chi_{j+1/2} \left[ \left( a_x^2 + a_y^2 \right) \left( \frac{f_{j+1} - f_j}{\Delta v_{j+1/2}} \right) \right. \right. \\
 & \quad \left. \left. + \left( \beta_x a_x + \beta_y a_y \right)_{j+1/2} v_{j+1/2} f_{j+1/2} \right] \right. \\
 & \quad \left. - \chi_{j-1/2} \left[ \left( a_x^2 + a_y^2 \right) \left( \frac{f_j - f_{j-1}}{\Delta v_{j-1/2}} \right) \right. \right. \\
 & \quad \left. \left. + \left( \beta_x a_x + \beta_y a_y \right)_{j-1/2} v_{j-1/2} f_{j-1/2} \right] \right\}_{k,l}, \quad (23)
 \end{aligned}$$

where the interpolation formula for  $f_{j+1/2}$ , as well as the coefficients  $\mathbf{a}$  and  $\boldsymbol{\beta}$ , are calculated as previously shown.

Although the ohmic-heating term is normally included in FP simulations,<sup>17,30,31</sup> Town and Bell<sup>32</sup> recently suggested that since its net heating contribution vanishes for a zero-current plasma, its effect on the thermal transport might be negligible. For all *SPARK* simulations considered, this hypothesis appears to be true.

## 7. Viscous Heating

The total energy density deposited in the plasma, as a result of the viscous pressure  $Q_{\text{vis}}$  [Eq. (9)], is given by  $h_{\text{vis}} = -Q_{\text{vis}} \nabla \cdot \mathbf{u}_i$ . Since the ions are assumed cold, this energy is transferred directly to the electrons [Eq. (6)]. In the FP equation, we achieve this by introducing a collision operation [term (f), Eq. (4)] with a coefficient of the form

$$H_{\text{vis}} = \frac{2h_{\text{vis}}}{\sum_{j=1}^J v_j^2 \left( \frac{f_{j+1} - f_j}{v_{j+1/2} \Delta v_{j+1/2}} - \frac{f_j - f_{j-1}}{v_{j-1/2} \Delta v_{j-1/2}} \right)}. \quad (24)$$

## Simulations

To illustrate the capabilities of *SPARK*, we consider two simulations. The first one is of the 1-D evolution of a laser-driven planar CH foil, and the second one is of the interaction of a spatially modulated laser beam on a 2-D planar CH plasma.

### 1. Laser-Driven CH Foil in 1-D Planar Geometry

The simulation considered here applies to Rayleigh-Taylor instability experiments performed at LLNL.<sup>33</sup> It models a CH foil illuminated by 527-nm laser light, with 1-ns linear rise followed by a 2-ns flat section.

For our initial conditions we assume an 18- $\mu\text{m}$ , fully ionized CH plasma at a temperature of 0.5 eV. The peak laser intensity is chosen to be  $5 \times 10^{13} \text{ W/cm}^2$ . *SPARK* is run in 1-D planar geometry, on a Lagrangian mesh, with the full linearized version of the  $e$ - $e$  collision operator [Eq. (19a)]. The configuration space mesh uses 150 zones, and the velocity mesh uses 35 feathered zones, with  $\Delta v_{j+1} / \Delta v_j = 1.11$  and  $v_j = 266 v_t$  (where  $v_t$  is the initial thermal velocity of the electrons).

Figure 54.1 shows the (a) temperature and (b) density profiles (solid curves) near the ablation front, 2 ns after the start of the laser pulse. The laser is incident from the right, and  $z = 0$  corresponds to the initial position of the target's rear surface. Using a fixed  $\Delta t = 0.5$  ps, the run took 15 min in CPU time on a CRAY Y-MP with an overall energy-conservation error of 1%.

For comparison, Fig. 54.1 also plots (dashed curves) the results based on the fluid-electron equation with SH heat flow [Eq. (6)]. From the temperature curves we note that the fluid model predicts excessive penetration of the main heat front, yet fails to predict the preheat at the rear of the target. This preheat, which is caused by long-mean-free-path electrons coming from the 1.5-keV corona, then has the effect of decompressing the target, as seen by the broader density profile in Fig. 54.1(b).

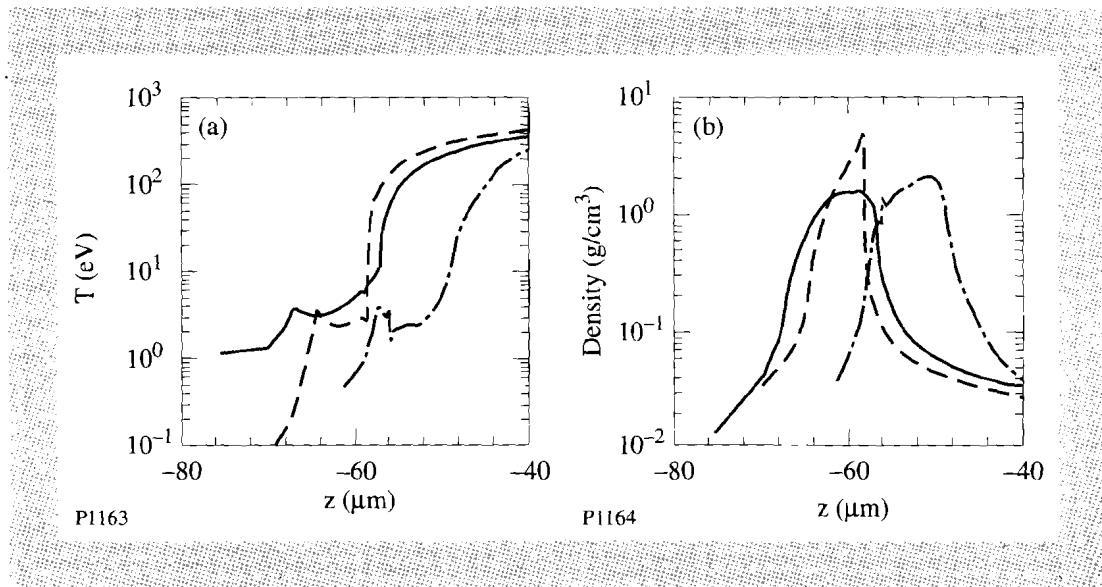


Fig. 54.1

Plots of (a) temperature in eV and (b) density in  $\text{g cm}^{-3}$  as functions of spatial position  $z$  ( $\mu\text{m}$ ) relative to the initial target surface. Solid curves correspond to FP simulation, dashed curves to SH simulation (with ideal gas equation of state, full ionization, and no radiation transport), and dash-dotted curves to *LILAC* simulation (with real equation of state, self-consistent ionization, and radiation transport).

Since the target's acceleration is found to be unaffected by the nonlocal transport, the main implication of these results to hydrodynamic stability is a reduction in peak density and a corresponding increase in ablation velocity ( $V_a$ ), which is plotted in Fig. 54.2 as a function of time. The reduction in the Rayleigh-Taylor growth arising from the increased  $V_a$  is of obvious benefit to ICF.

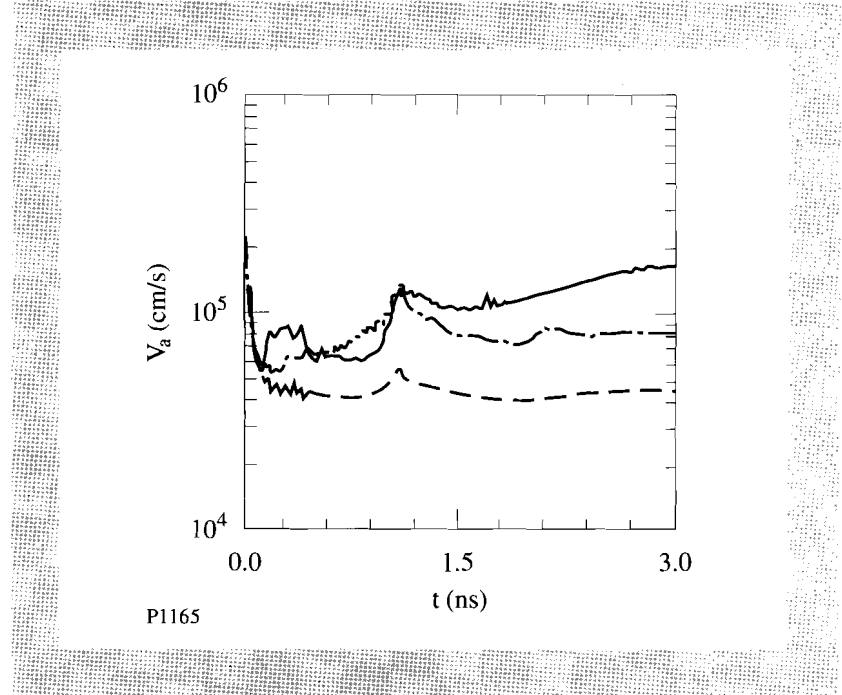


Fig. 54.2  
Plot of ablation velocity  $V_a$  in  $\text{cm s}^{-1}$  as a function of time (ns). Curves are identified as in Fig. 54.1.

However, the comparison previously made may be somewhat exaggerated because *SPARK* neglects radiation transport and ionization physics. To assess the relative importance of these effects, the *LILAC* hydrocode (at LLE) has been run under the same conditions (with no flux limit), but including a Thomas-Fermi equation of state, ionization from astrophysical tables, and radiation transport. The corresponding ablation-region profiles are plotted in Fig. 54.1, and  $V_a$  is plotted in Fig. 54.2 (dash-dotted curves). As observed, there is a significant impact from the additional physical effects included in *LILAC*. From this we may deduce that an accurate modeling of the experiments should include not only nonlocal heat transport, but also radiation and ionization effects.

## 2. Laser Filamentation in a 2-D Planar Plasma

Laser-filamentation experiments have been reported by Young,<sup>34</sup> where a 1.06- $\mu\text{m}$  laser beam with a 100-ps pulse length was intentionally modulated in space and made to interact with a preformed underdense CH plasma. These experiments have been successfully simulated using *SPARK*.<sup>4</sup> Recently, however, Rose and DuBois<sup>35</sup> claimed that Young's experiments should have been linearly stable to filamentation growth, by virtue of the finite  $f$ -number effects of the interaction beam. The motivation for the present simulations is, partly, to address this problem.

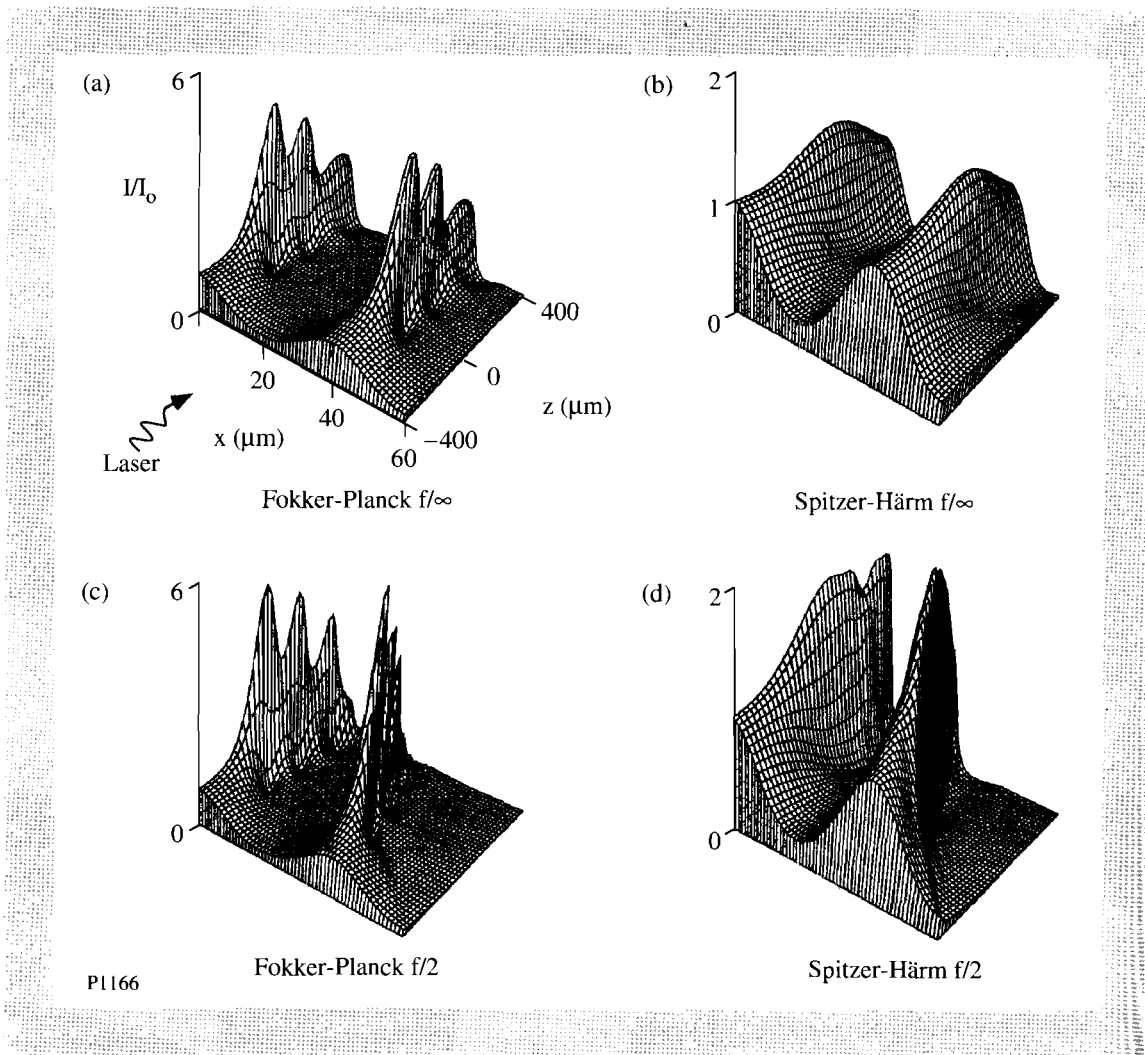
The simulation conditions have been described in detail by Epperlein and Short.<sup>4</sup> The plasma has an initial temperature of 0.8 keV, a uniform density in the  $x$ - $y$  plane,

and a parabolic density profile in the  $z$  direction, with a peak of one-quarter critical density at  $z=0$ . The interaction beam is spatially modulated in the  $x$  direction, with a wavelength of  $40\ \mu\text{m}$ , a peak intensity  $I_0$  of  $5 \times 10^{13}\ \text{W/cm}^2$ , and pulse width of  $100\ \text{ps}$ . Its propagation is calculated via the paraxial wave equation, and the convergence effect caused by the finite  $f$  number is modeled by using a spherical phase front with focus at  $x=0$ .<sup>36</sup> *SPARK* is run in 2-D planar geometry on a Eulerian mesh with  $\Delta x = 1\ \mu\text{m}$ ,  $\Delta z = 20\ \mu\text{m}$ ,  $\Delta v = 0.7v_p$ , and  $\Delta t = 0.01\ \text{ps}$ .

Figure 54.3 shows the surface plot of the normalized laser intensity  $I/I_0$  at the peak of the pulse with  $f/\infty$  and  $f/2$  optics and FP and SH thermal transport. The *SPARK* simulation took 80 min in CPU time on a CRAY Y-MP with an overall energy conservation error of 0.1%.

Fig. 54.3  
Surface plots of normalized laser intensity  $I/I_0$  with (a) FP transport and  $f/\infty$ , (b) SH transport and  $f/\infty$ , (c) FP transport and  $f/2$ , and (d) SH transport and  $f/2$ .

Comparison between FP and SH simulations confirms previous results that nonlocal heat transport enhances the laser filamentation rate.<sup>10,12</sup> More importantly, we find that the convergence effect caused by the  $f/2$  lens actually enhances the level of self-focusing, with the filaments following the ray trajectories, as observed experimentally.<sup>37</sup>



## Discussion and Conclusions

This article has shown that it is possible to write an efficient electron-FP, ion-fluid code to investigate 1-D and 2-D transport problems of interest to ICF. Briefly, to achieve this aim the FP equation is first simplified by means of a two-term angular expansion of the electron-distribution function, and the resultant equation is then solved via an ADI scheme. The *SPARK* code, which incorporates this approach, has been described in detail.

There are currently two main approximations in *SPARK*: it assumes a full ionization and it neglects radiation effects. Although these approximations may hold well in the hot, underdense corona of a laser-driven ICF pellet, the effects of ionization and radiation could be significant in the cold matter ahead of the main heat front. The implications of ionization effects, real equation of state, and radiation have already been demonstrated in Fig. 54.1, for the case of SH thermal transport. Within the FP formalism, the atomic physics would be incorporated in the form of additional collision operators that would model such processes as excitation, ionization, and recombination.

Another possible improvement to *SPARK* would be to introduce spatial mesh rezoning in 2-D transport simulations. This capability would allow for investigations of thermal smoothing and Rayleigh-Taylor instabilities.

## ACKNOWLEDGMENT

This work was supported by the U.S. Department of Energy Office of Inertial Confinement Fusion under Cooperative Agreement No. DE-FC03-92SF19460, the University of Rochester, and the New York State Energy Research and Development Authority. The support of DOE does not constitute an endorsement by DOE of the views expressed in this article.

## REFERENCES

1. A. R. Bell, R. G. Evans, and D. J. Nicholas, *Phys. Rev. Lett.* **46**, 243 (1981).
2. A. Nishiguchi *et al.*, *Phys. Fluids B* **4**, 417 (1992).
3. E. M. Epperlein and R. W. Short, *Phys. Fluids B* **3**, 3092 (1991).
4. E. M. Epperlein and R. W. Short, *Phys. Fluids B* **4**, 2211 (1992).
5. E. M. Epperlein, P. Amendt, L. Powers, and L. J. Suter, Laboratory for Laser Energetics Report No. 232 (1992).
6. S. I. Braginskii, *Reviews of Plasma Physics* (Consultants Bureau, New York, 1965), p. 205.
7. L. Spitzer, Jr. and R. Härm, *Phys. Rev.* **89**, 977 (1953).
8. R. C. Malone, R. L. McCrory, and R. L. Morse, *Phys. Rev. Lett.* **34**, 721 (1975).
9. A. R. Bell, *Phys. Fluids* **26**, 279 (1983).
10. E. M. Epperlein, *Phys. Rev. Lett.* **65**, 2145 (1990).
11. E. M. Epperlein, in *Research Trends in Physics: Nonlinear and Relativistic Effects in Plasmas*, edited by V. Stefan (American Institute of Physics, New York, 1991), p. 43.

12. E. M. Epperlein, *Phys. Fluids B* **3**, 3082 (1991).
13. R. W. Short and E. M. Epperlein, *Phys. Rev. Lett.* **68**, 3307 (1992).
14. E. M. Epperlein and R. W. Short, *Phys. Fluids B* **4**, 4190 (1992).
15. H. A. Rose and D. F. DuBois, *Phys. Fluids B* **4**, 1394 (1992).
16. M. N. Rosenbluth, W. M. MacDonald, and D. L. Judd, *Phys. Rev.* **107**, 1 (1957).
17. E. M. Epperlein, G. J. Rickard, and A. R. Bell, *Phys. Rev. Lett.* **61**, 2453 (1988).
18. E. M. Epperlein, G. J. Rickard, and A. R. Bell, *Comput. Phys. Commun.* **52**, 7 (1988).
19. A. B. Langdon, *Phys. Rev. Lett.* **44**, 575 (1980).
20. J. R. Sanmartin *et al.*, *Phys. Fluids B* **4**, 3579 (1992).
21. R. J. Mason, *J. Comput. Phys.* **41**, 233 (1981).
22. R. D. Richtmyer and K. W. Morton, *Difference Methods of Initial-Value Problems* (Wiley, New York, 1967), p. 313.
23. J. Douglas, Jr., *Numer. Math.* **4**, 41 (1962).
24. J. Douglas, Jr. and J. E. Gunn, *Numer. Math.* **6**, 428 (1964).
25. W. R. Briley and H. McDonald, *J. Comput. Phys.* **34**, 54 (1980).
26. R. J. Wright, *J. Phys. D: Appl. Phys.* **14**, 805 (1981).
27. G. J. Pert, *J. Comput. Phys.* **49**, 1 (1983).
28. J. S. Chang and G. Cooper, *J. Comput. Phys.* **6**, 1 (1970).
29. A. B. Langdon, in *CECAM Report of Workshop on "The Flux Limiter and Heat Flow Instabilities in Laser-Fusion Plasmas"* (Université Paris Sud, France, 1981), p. 69.
30. J. P. Matte, T. W. Johnston, J. Delettrez, and R. L. McCrory, *Phys. Rev. Lett.* **53**, 1461 (1984).
31. T. H. Kho and M. G. Haines, *Phys. Fluids* **29**, 2665 (1986).
32. R. P. J. Town and A. R. Bell, in *CECAM Report of Workshop on "Laser-Plasmas Interactions"* (Université Paris Sud, France, 1991), p. 36.
33. S. G. Glendenning, S. V. Weber, P. Bell, L. B. DaSilva, S. N. Dixit, M. A. Henesian, D. R. Kania, J. D. Kelkenny, H. T. Powell, R. J. Wallace, P. J. Wegner, J. P. Knauer, and C. P. Verdon, *Phys. Rev. Lett.* **69**, 1201 (1992).
34. P. E. Young, *Phys. Fluids B* **3**, 2331 (1991).
35. H. A. Rose and D. F. DuBois, *Phys. Fluids B* **4**, 252 (1992).
36. J. A. Fleck, Jr., *J. Comput. Phys.* **16**, 324 (1974).
37. P. E. Young *et al.*, *Phys. Rev. Lett.* **61**, 2336 (1990).

## 2.B Strategies for Ultra-High Laser Uniformity Using Zero-Correlation Phase Masks

Laser fusion requires highly uniform target irradiation to minimize development of hydrodynamic instabilities. Random phase plates<sup>1,2</sup> have been used routinely to provide a uniform far-field intensity envelope on target that is relatively independent of the input-beam profile. However, superposed on this envelope is highly modulated speckle from the interference among different phase-plate elements. Once a sufficiently large plasma atmosphere has developed around the target, the effects of speckle will be greatly reduced, as nonuniformities in laser-energy deposition will be smoothed by thermal conduction within the target. However, prior to that stage, the irradiation nonuniformities will imprint themselves on the target surface. The resulting surface deformation will act as a “seed” for growth of the Rayleigh-Taylor hydrodynamic instability that can preclude a high-density compression and high thermonuclear yield. Beam-smoothing techniques<sup>3,4</sup> have been developed to change the speckle pattern in time and produce a relatively smooth, time-averaged intensity profile. The main issue is whether the intensity modulations are reduced on a fast-enough time scale to prevent significant beam imprinting on a target in the early stages of irradiation.

Uniformity during the onset of irradiation is more easily addressed for laser configurations such as the OMEGA Upgrade,<sup>5</sup> for which the early-time “foot” of the pulse is spatially separated from the main part of the pulse. (For the OMEGA Upgrade, the foot pulse will contain less than 10% of the pulse energy. It will co-propagate with the main pulse through the same beamlines but occupy only the inner 20%–30% of the aperture radius.) Because of the physical separation between these parts of the pulse, it is possible to apply additional uniformity techniques to the foot pulse that might not be appropriate for the larger, more-energetic main portion of the beam. The strategies discussed here have been specifically designed for the foot pulse to achieve the higher levels of uniformity required at the onset of target irradiation.

To obtain the higher uniformity, we have developed a technique for choosing the phase-plate elements (in combination with polarization rotation) such that the speckle intensity modulations, normally produced from a phase plate, are instantaneously zero, at least in the limit of plane-wave, near-field irradiation. Such phase plates are referred to here as zero-correlation masks (ZCM). For a beam with small phase aberrations, the far-field intensity fluctuations around the envelope will also be small. However, for large phase aberrations the resulting speckle modulation will be the same as for a random phase plate. Some strategies for reducing the sensitivity of a ZCM to phase aberrations and to other near-field imperfections will be discussed.

### Zero-Correlation Mask

A key ingredient for forming a ZCM is polarization rotation across one-half of the phase-plate elements. The interference patterns produced by each of the polarization directions are chosen to be complementary, such that the intensity peaks of one exactly fill the valleys of the other. More formally, the phases are

distributed such that the sum of the autocorrelation functions for the two degrees of polarization are exactly zero for each spatial wavelength of nonuniformity. An algorithm for generating ZCM's is described in Ref. 6.

A comparison between the far-field intensity patterns for a random phase plate and a ZCM is shown in the computer simulations of Figs. 54.4(a) and 54.4(b). Both cases used a  $32 \times 32$  phase plate with phase elements of either  $0$  or  $\pi$ . Both plates were uniformly illuminated and had a  $90^\circ$  polarization rotation across one-half of the elements. The only difference is that in Fig. 54.4(a) the phases were chosen randomly, and in Fig. 54.4(b) the phases were chosen according to the ZCM algorithm of Ref. 6.

The smooth intensity profile calculated for the ZCM in Fig. 54.4(b) requires a very delicate balance among all phase differences across the mask. The calculation assumed ideal illumination conditions such as no spatial variation of phase or amplitude across the phase plate, perfect focusing of the beam, and high-contrast polarization rotation. Large deviations from ideal conditions will destroy the delicate phase balance and introduce speckle structure, similar to Fig. 54.4(a). For small variations from ideal conditions, the modulation of the speckle is proportional to the near-field variation. For instance, when the phase aberration is less than a few tenths of a wave, the rms intensity variation around the smooth envelope is found to be proportional to the rms phase variation of the aberration.

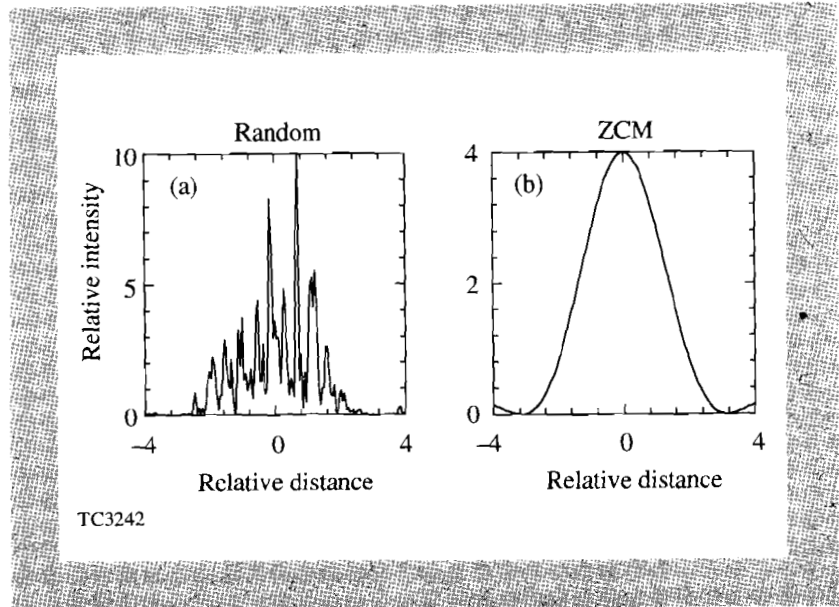


Fig. 54.4  
Far-field intensity profile for (a) a random phase plate with a polarization rotator and (b) ZCM. Both are  $32 \times 32$  phase plates with plane-wave, near-field irradiation.

When a ZCM is used instead of a random phase plate, there is new motivation to construct and maintain high-quality laser beams, i.e., the more uniform the near-field profile, the smoother the target irradiation. Phase-correction techniques can be considered. In contrast, with a random phase plate, highly modulated speckle would be produced even for a plane-wave, near-field beam. Of course, if the near-field profile is perfectly smooth, then a phase plate would not be necessary for uniform target irradiation, providing that the beam was properly apodized to prevent Fresnel ringing. However, there are situations where it is

advantageous to use a phase plate, such as for combining the foot pulse and main pulse on the OMEGA Upgrade laser.

The effects of phase aberrations on a ZCM can be reduced using either of the beam-smoothing techniques, induced spatial incoherence (ISI)<sup>3</sup> or smoothing by spectral dispersion (SSD).<sup>4</sup> To employ ISI, the phase plate would be divided into many ( $N$ ) smaller ZCM's. The time-averaged interference among different ZCM's would be removed by introducing time delays among them, in increments of at least one laser coherence time. Any remaining interference would be the result of phase aberrations across the individual ZCM's. If the aberrations are of long spatial wavelengths across the beam, then the phase variation across each ZCM will be relatively small for moderate values of  $N$ . If these phase variations across each ZCM are all different, then the rms far-field fluctuation, for the superposition of all  $N$  ZCM's, will be reduced by  $1/\sqrt{N}$ , compared to the single ZCM result.

SSD can be used with a ZCM in exactly the same way it has been used with a random phase plate. Since SSD imposes a variation of "instantaneous" frequency (i.e., time-dependent phase) across the beam, the delicate balance of phase required for a ZCM is not satisfied instantaneously. However, when the far-field intensity is averaged over an integral number of modulation times (for sinusoidal phase modulation), then the ZCM phase balance is restored, as is true for the asymptotic time-averaged result. The effect of SSD is shown in Fig. 54.5, which shows the asymptotic result for (a) a random phase plate, (b) a  $32 \times 32$  ZCM with the measured OMEGA phase error,<sup>7</sup> and (c) a ZCM with the OMEGA phase error reduced by 80%. Figure 54.5(b) used the measured phase variation from the central 20% of the OMEGA beam radius to estimate the phase error that might occur for the foot pulse of the OMEGA Upgrade. (The foot pulse in the original design for the Upgrade occupied a slightly larger percentage of the beam aperture; the advantages of using a smaller size will be discussed.) In Fig. 54.5(c), this phase error was reduced by 80% to examine the effect of phase correction that might be possible for the static part of the foot-pulse aberration. In the limit of zero phase error, the time-averaged, far-field beam with SSD is perfectly smooth.

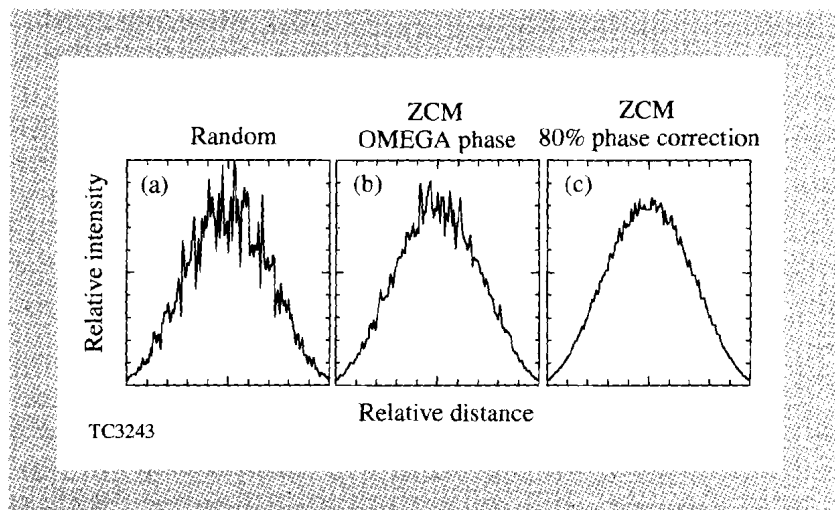


Fig. 54.5  
The result of SSD (with one-dimensional dispersion) on the far-field intensity profiles for (a) a random phase plate with a polarization rotator; (b) a ZCM with the measured OMEGA phase error; and (c) same as (b) but with the phase error reduced by 80%. (SSD bandwidth =  $10 \text{ \AA}$ , frequency = 30 GHz, dispersion =  $300 \text{ \mu rad}$ .)

### Other Instantaneous Smoothing Techniques

We discuss two additional techniques for instantaneously eliminating far-field intensity fluctuations that can arise from interference among phase-plate elements. These techniques are limited to only a selected range of spatial frequencies, unlike the ZCM, which eliminates all spatial wavelengths of nonuniformity. However, these techniques are not sensitive to phase aberrations or other near-field imperfections.

#### 1. Beam-Size Effects

The first of these techniques is relatively trivial but worth taking into consideration when designing a laser system. In most cases, the size of the laser beam is predetermined by energy, damage-threshold, and cost considerations. For those cases, the discussion in this subsection is not relevant. However, if the laser design offers some flexibility with regard to beam size, such as the foot pulse of the OMEGA Upgrade laser, then the following comments would apply.

The smallest possible beam size should be used for those applications that would benefit from elimination of irradiation nonuniformities with very short spatial wavelengths. Short-wavelength structure is produced from interference between phase-plate elements that are far apart. For a small beam, these distant phase-plate elements simply do not exist, and the resultant nonuniformity is limited to the longer wavelengths. For laser-fusion applications, this would mean complete elimination of the fastest-growing modes of the Rayleigh-Taylor hydrodynamic instability driven by laser nonuniformities.

There is considerable flexibility in choosing the size of the foot pulse for the OMEGA Upgrade laser, as the division of the pulse into low-intensity and high-intensity portions is somewhat arbitrary. There are two main constraints from a laser point of view: (1) The foot pulse must be large enough to adequately pass through the spatial filter pinholes. (2) Enough low-intensity light must have been removed from the main pulse that the efficiency for frequency tripling remains relatively high. From a laser-target point of view, the main constraint is that the foot pulse must contain enough energy to create a sufficiently large plasma atmosphere that the short-wavelength structure will be smoothed at the onset of irradiation from the main pulse. These considerations can be met if the foot pulse is several times smaller than in the original OMEGA Upgrade design.

For a ZCM, there is an additional advantage to using the smallest possible foot pulse on the OMEGA Upgrade. The phase variation is often the most uniform near the very center of the aperture. Using only this region minimizes intensity fluctuations produced in the far field of the ZCM. For these reasons, we have assumed a relatively small foot pulse in the examples here.

#### 2. Controlled Amplitude Modulation

A second technique for eliminating interference structure among phase-plate elements is to impose controlled amplitude modulation throughout the pulse, together with time delays across the phase plate, so that only selected elements are illuminated at any one time. Then, of course, there cannot be any interference among phase-plate elements that are not simultaneously illuminated.

A schematic of this concept is illustrated in Fig. 54.6. Regularly spaced amplitude modulation is imposed upon the beam such that, in this example, the pulse is “on” 25% of the time and “off” the remaining 75% of the time. Such modulation could be imposed by spectral pulse-shaping techniques discussed in Ref. 8. At the phase plate, a time delay is introduced across different sections of the beam. In this example, four time-delay steps would be used, with step increments of 1/4 the cycle time between amplitude peaks. Only two of the steps are displayed in the figure. The result is that when one quadrant is being illuminated with a pulse peak, the other quadrants are “off.” This completely eliminates interference among phase-plate elements from different quadrants and, consequently, further reduces the short-wavelength nonuniformity produced from interference among distant elements.

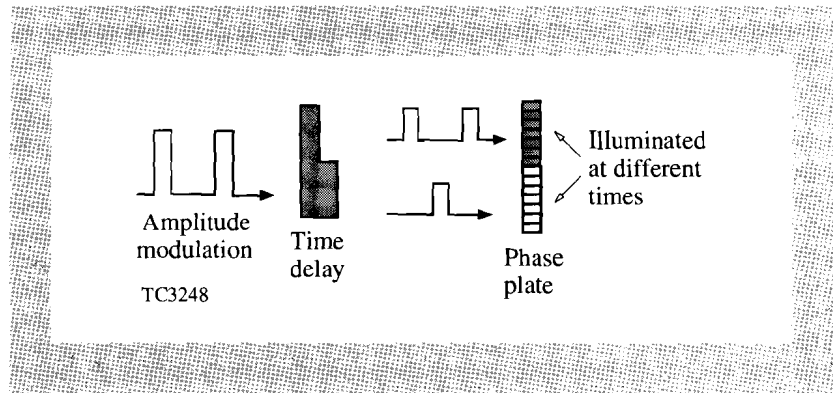


Fig. 54.6

Controlled amplitude modulation. Regularly spaced amplitude modulation is imposed upon the beam early in the laser chain. At the phase plate, time-delay steps are used to segment the beam so that only one section of the phase plate is illuminated with the intensity peak at any time, thereby eliminating all interference among different sections. In the figure, the shortest possible wavelength structure has been eliminated by preventing interference among the most-distant phase-plate elements.

Note that even though the pulse is “off” 75% of the time, the target is still continuously illuminated. At any time during the pulse, light is passing through one of the phase-plate quadrants. Since every phase-plate element completely irradiates the target, continuous uniform target illumination is obtained. Clearly, the intensity in each amplitude spike would have to be four times larger than the average intensity required to drive the target. This is ideal for the foot pulse, as the increased intensity would enhance its frequency-tripling efficiency.

Controlled amplitude modulation can be combined with ZCM’s by choosing each of the phase-plate quadrants to be a separate ZCM. In the limit of perfect near-field conditions, each quadrant would produce a smooth intensity profile on target.

### Combining Several Techniques

An example of combining all the beam uniformity techniques previously discussed is shown in Fig. 54.7. A small beam with a  $32 \times 32$  phase plate is used. The beam is segmented into four parts, each with a different frequency. With this

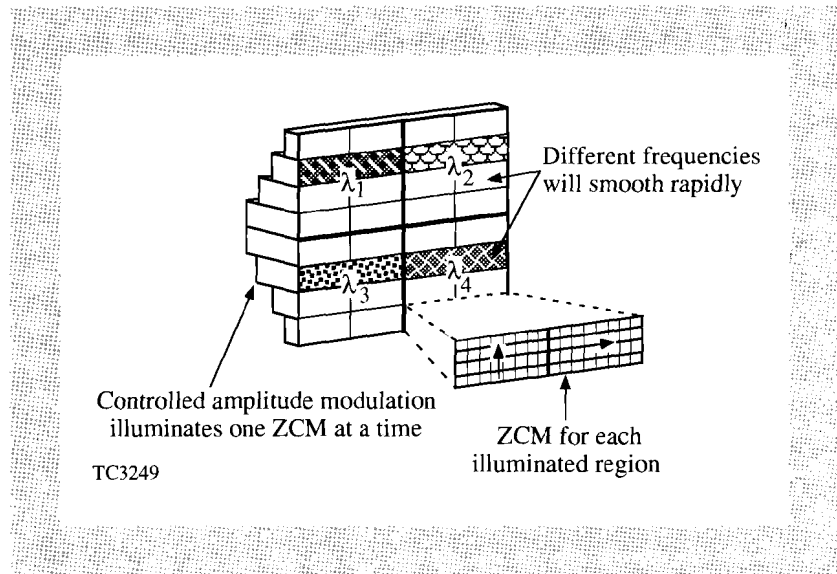


Fig. 54.7

One possible configuration for combining different beam-uniformity techniques. These include ZCM, controlled amplitude modulation, and SSD.

form of SSD using spatially separated frequencies, as opposed to phase-modulated bandwidth, all interference among the different beam segments will be completely smoothed in time, without leaving any residual nonuniformity. Each beam frequency irradiates a  $16 \times 16$  quadrant of phase-plate elements. Each of these quadrants is further subdivided into four sections with the time-delay steps used for implementation of controlled amplitude modulation. Each of these sections is chosen to be a separate  $4 \times 16$  ZCM. Since each ZCM is, in fact, divided into two noninterfering portions by means of a polarization rotation, the full phase plate has now been separated into 32 incoherent, or totally noninterfering, sections, each of dimension  $4 \times 8$ .

The interference structure produced by each  $4 \times 8$  section is cancelled by its ZCM complement for perfect near-field conditions. For significant near-field fluctuations, the asymptotic nonuniformity is similar to the incoherent superposition of 32 intensity patterns from different  $4 \times 8$  random phase plates. The shortest spatial wavelength of any asymptotic nonuniformity structure is determined by the size of the  $4 \times 8$  subsection of the phase plate. Instantaneously, however, there is a shorter-wavelength structure produced by the interference among rays of different frequency from more-distant phase-plate elements. But this interference will smooth to zero as  $1/(\Delta\nu T)$ , where  $\Delta\nu$  is the frequency difference and  $T$  is the averaging time.

We have calculated the nonuniformity that might be expected using these combined techniques on the foot pulse of the OMEGA Upgrade laser. The inner 20% of the measured OMEGA phase aberration was used without assuming any phase correction. The IR beam was assumed to be segmented into four parts, each with a different frequency. The frequencies were in increments of 150 MHz ( $5 \text{ \AA}$ ), which was tripled upon frequency conversion. Controlled amplitude modulation was imposed with a cycle time of 20 ps. The resulting nonuniformity was calculated as the rms variation on a spherical target for 60 overlapping beams.

The time-averaged, rms intensity variation is plotted as a function of averaging time in Fig. 54.8, for three different uniformity techniques, each using a  $32 \times 32$  phase plate with a polarization rotator. The curve marked “current” is with the current form of SSD using 9-GHz sinusoidal phase modulation and  $3 \text{ \AA}$  of bandwidth spectrally dispersed in one dimension. The curve marked “near term” shows the improvement obtained with two-dimensional SSD using 30- to 40-GHz modulation frequencies and  $7\text{-}\text{\AA}$  bandwidth dispersed in two perpendicular directions. Finally, the combination of techniques discussed in this article (using ZCM’s, controlled amplitude modulation, and pure-frequency SSD) is shown as the curve marked “future.” This curve indicates that rms values below  $\sim 1\%$  can be achieved with smoothing times of the order of 10 ps–15 ps, using these combined techniques. This level of uniformity and smoothing time is consistent with currently accepted requirements for startup conditions. It should be emphasized that these calculations have not assumed any additional smoothing by thermal conduction within a plasma atmosphere. The laser irradiation was mapped directly onto the target surface to model startup conditions.

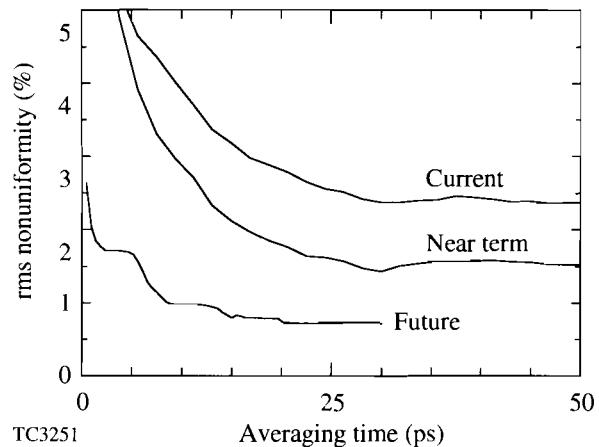


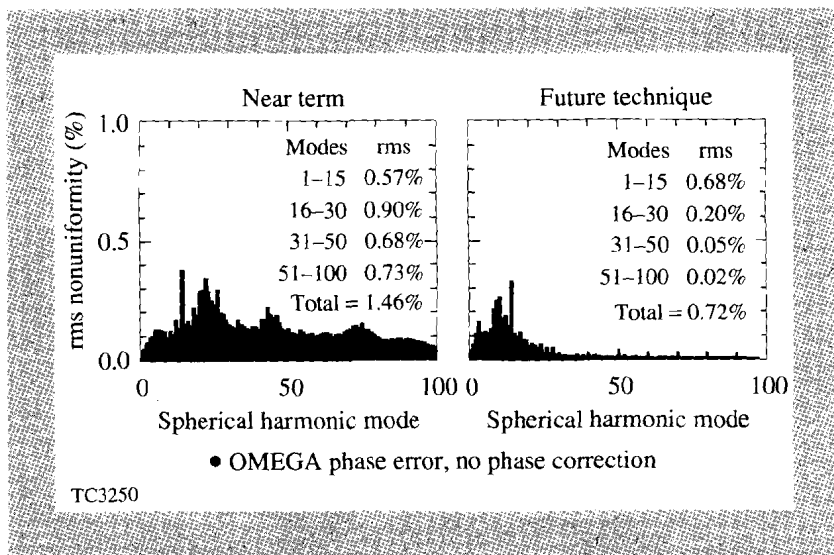
Fig. 54.8

The rms irradiation nonuniformity for 60-beam overlap on a spherical target. (a) current: one-dimensional SSD; (b) near term: two-dimensional SSD; (c) future: combination of ZCM, controlled amplitude modulation, and pure-frequency SSD shown in Fig. 54.7. All configurations used a polarization rotator and the measured OMEGA phase error (without phase correction). No thermal smoothing in a plasma atmosphere was assumed.

A treatment of the startup problem must address not only the magnitude of the irradiation nonuniformity, but also its spatial wavelength. A wavelength decomposition of the asymptotic nonuniformity for the “near-term” and “future” results of Fig. 54.8 is shown in Fig. 54.9, in terms of spherical harmonic mode numbers. The “future” uniformity techniques have essentially eliminated all short-wavelength structure corresponding to modes greater than  $\sim 30$ . These modes are considered the most dangerous for seeding the Rayleigh-Taylor hydrodynamic instability, as they grow the fastest.

Fig. 54.9

A spherical harmonic decomposition of the asymptotic nonuniformity for the “near-term” and “future” results of Fig. 54.8. Note how the future technique has effectively eliminated all short-wavelength nonuniformity. All configurations used a polarization rotator and the measured OMEGA phase error (without phase correction). No thermal smoothing in a plasma atmosphere was assumed.



### Discussion

Several new techniques have been presented here for obtaining the high levels of uniformity required at the onset of laser irradiation. Undoubtedly, new variations of these techniques, as well as entirely new concepts, will be developed over the next few years, adding increased flexibility for achieving the required levels of irradiation uniformity. The methods for implementing and combining these techniques will depend on details of the individual laser system. The greatest flexibility is achieved when the low-energy, early-time portion of the pulse (foot pulse) is physically separated from the main pulse, as in the design for the OMEGA Upgrade laser. The best uniformity techniques might be wasteful of energy and inappropriate for the main pulse, but they could be implemented on the foot pulse where high uniformity is most crucial.

All of the new uniformity techniques discussed here would require some developmental work before they could be implemented on a high-power laser. For a ZCM, the technique for distributing the phases according to a specified pattern is current technology, but the required polarization rotation across half the phase plate has not yet been demonstrated. To date, a polarization rotator in the form of a wedge has been developed, where the polarization changes continuously across the phase plate. The extension to a single step should be straightforward. The technique for generating controlled amplitude modulation across the pulse, with a cycle time of  $\lesssim 25$  ps, has not yet been examined; however, it should be only a small extension of the spectral pulse-shaping techniques currently under investigation. (An array of high-optical-quality, time-delay steps properly registered with the phase plate would also have to be developed.) Finally, implementation of pure-frequency SSD would include developmental work for the following: (1) generating the discrete-frequency beams, (2) co-propagating the beams, and (3) frequency tripling. For example, when different frequencies were used in the calculations, they were spatially separated so that frequency tripling could be accomplished by means of optical wedges that will deflect each component through the tripling crystals at the optimal angle for that frequency. After the crystals, a second set of wedges would recollimate the beams.

Techniques such as these will be developed and implemented to meet the uniformity needs in upcoming experiments.

#### ACKNOWLEDGMENT

This work was supported by the U.S. Department of Energy Office of Inertial Confinement Fusion under Cooperative Agreement No. DE-FC03-92SF19460 and the University of Rochester. The support of DOE does not constitute an endorsement by DOE of the views expressed in this article.

#### REFERENCES

1. Y. Kato *et al.*, *Phys. Rev. Lett.* **53**, 1057 (1984).
2. T. J. Kessler, *LLE Review* **33**, 1 (1987).
3. R. H. Lehmburg, A. J. Schmitt, and S. E. Bodner, *J. Appl. Phys.* **62**, 2680 (1987).
4. S. Skupsky, R. W. Short, T. Kessler, R. S. Craxton, S. Letzring, and J. M. Soures, *J. Appl. Phys.* **66**, 3456 (1989).
5. J. M. Soures, R. L. McCrory, T. R. Boehly, R. S. Craxton, S. D. Jacobs, J. H. Kelly, T. J. Kessler, J. P. Knauer, R. L. Kremens, S. A. Kumpan, S. A. Letzring, W. D. Seka, R. W. Short, M. D. Skeldon, S. Skupsky, and C. P. Verdon, "The OMEGA Upgrade Laser for Direct-Drive Target Experiments," to be published in *Laser and Particle Beams*.
6. S. Skupsky and T. Kessler, "A Speckle-Free Phase Plate (Diffuser) for Far-Field Applications," to be published in *Journal of Applied Physics*.
7. T. J. Kessler, *LLE Review* **31**, 114 (1987).
8. S. Skupsky, T. J. Kessler, S. A. Letzring, and Y.-H. Chuang, *J. Appl. Phys.* **73**, 2678 (1993).

## 2.C Fast, Optically Triggered, Superconducting Opening Switches

In high-power applications, opening switches play an important role. These switches are required to carry high currents (100 A–10 MA) and operate with short switching times (10 ms–10 ns). Moreover, before opening, the switch must conduct current to a parallel circuit branch (load) and withstand the voltage across the load. If there is no load in parallel to the switch, it must absorb all the energy stored in the circuit inductance. For a practical pulsed-power generator employing inductive energy storage, the opening switch has to be operated repeatedly. These diverse requirements make the design of an opening switch a challenging problem.

The existing opening switches include plasma opening switch (POS), plasma erosion opening switch (PEOS), plasma flow switch (PFS), reflex opening switch (ROS), and explosive opening switch (EOS). All these switches are used to interrupt the flow of current in the circuit. An alternative approach to the switching problems is the superconducting, inductively coupled switch (SICS), in which the load is connected to the secondary coil of the transformer while current flows through the primary. The current flow in the primary is uninterrupted. The switching is accomplished by removing a magnetic screen that isolates the secondary from the primary. This approach is particularly suited to superconducting magnetic-energy storage (SMES) applications where a persistent current is required. Since there is no switch in the storage coil (primary), there is no dissipation of energy. The number of times switches like PEOS can be operated is limited because the surface discharge degrades the source. Explosive switches are also not suited for applications requiring repetitive switch operation. The SICS has been operated up to kHz repetition rates using a train of short laser pulses, and no degradation of performance has been observed.

Part of the interest in these switches is their possible use in reducing peak electrical loads in pulsed-power systems. This may have an application in the OMEGA Upgrade charging systems.

Other types of superconducting opening switches have been investigated.<sup>1,2</sup> All superconducting switches involve a transition of the material from the superconducting to the normal state. The transition can be achieved by either heating the material above its critical temperature  $T_c$ , exceeding its critical current density  $J_c$ , or exceeding its critical magnetic field  $H_c$ . High- $T_c$  superconductors appear to be superior to the metallic superconductors as material for the opening switch, as we will discuss in the next section. In our experiments, heating a  $\text{YBa}_2\text{Cu}_3\text{O}_{7-x}$  (YBCO) film by laser pulses was used to perform the switching.

### Principle of Operation

First we will discuss the properties of the superconducting material (YBCO) and then describe the concept of the inductively coupled switching.

### 1. Material Properties of the Switch

Superconducting transitions involve switching from a zero-resistance superconducting state to a finite-resistance “normal” state. High- $T_c$  ceramic superconductors have a normal-state resistance that is orders of magnitude higher than the low- $T_c$  metallic superconductors. An opening switch can be made by using the superconductor to shunt the load. When triggered by short laser pulses, these switches exhibit off-state resistances of the order of 100  $\Omega$ , depending on the switch geometry, and switching times of the order of 50 ns to 100 ns. These are called photoresistive opening switches.<sup>1</sup> The YBCO thin films have critical-current densities in the range of 1–10 MA/cm<sup>2</sup> and a 1-cm-wide, 1-mm-thick film will carry 0.1 kA to 1 kA of current. The high  $J_c$  makes YBCO an attractive material for the opening switch.

High- $T_c$  superconductors are black and absorb light in the visible-near-IR range effectively. Fast heating of the film is necessary to perform the switching; this is accomplished by irradiating the film with laser pulses. Optical triggering provides accurate timing. In a current multiplication circuit using programmed inductive elements (PIE), storage inductors are charged in series and discharged sequentially, in stages that are connected in parallel with the load, through a set of isolating closing switches.<sup>3</sup> This circuit can be used to deliver a large load current using switches rated at a fraction of that current. The most important constraint in such a circuit is the synchronization of the opening switches with the closing switches. If the opening switches are not triggered within a short temporal window, transient high currents or voltages will catastrophically destroy the circuit elements. Optically triggered opening switches can be suitable in circuits with such constraints.

Superconductors behave as perfect diamagnets if the externally applied field is less than  $H_c$ . This means that a superconducting film in a magnetic field will expel the magnetic flux and act as a magnetic screen (Meissner effect). This property is used in our switch. In type-II superconductors such as YBCO, there exists a lower critical field  $H_{c1}$  and a higher critical field  $H_{c2}$ . When the flux penetrates the superconductor following a laser trigger, for  $H_{c1} < H_{\text{applied}} < H_{c2}$ , the flux reaches a stable state, and subsequent cooling of the film in a magnetic field may not exclude the flux. This may prevent the switch from operating repetitively. Primary currents in our experiments produced fields  $H_{\text{applied}}$  lower than  $H_{c1}$ . In this regime the flux penetration and exclusion above and below  $T_c$  are reversible. It is worth mentioning here that YBCO is anisotropic, and the magnetic flux screening is most effective if the field is parallel to the  $c$ -axis of the film. The films used in our experiments are high-quality,  $c$ -axis-oriented epitaxial films with  $J_c$  exceeding 1 MA/cm<sup>2</sup> and  $T_c$  ranging from 85 K to 90 K.<sup>4</sup>

Another advantage of using high- $T_c$  superconductors as compared to low- $T_c$  superconductors is the low cooling cost. Liquid nitrogen is sufficient as the cryogen when YBCO films are used to construct the switch.

We have found no evidence that the superconducting film degrades with repeated operation. The switches have been triggered by 150-ps pulses from a Nd:YAG laser at repetition rates up to 1 kHz. High repetition rates are limited by the switch recovery time, which in this case depends on how fast the heat can be extracted from the film.

## 2. Superconducting, Inductively Coupled Switch

The switch consists of a film of high- $T_c$  superconductor placed between the primary and secondary coil of the transformer (Fig. 54.10). A similar configuration has been used for the measurement of critical current in films.<sup>5</sup> The film, the primary coil, and the secondary coil need not be at the same temperature. For example, in a SMES system the primary coil would be a superconducting magnet. With present technology these magnets, made from low- $T_c$  materials, require cooling below 10 K ( $\text{Nb}_3\text{Sn}$ ,  $T_c = 18.5$  K) or with liquid helium ( $\text{Nb-Ti}$ ,  $T_c = 9.5$  K) for an optimum performance. The film can be at liquid-nitrogen temperature and the secondary coil, which is connected to the load, can be at room temperature. In our experiments, however, we used copper coils for both the primary and secondary coils and placed the film and coils inside a temperature-controlled cryostat cooled by a closed-cycle refrigerator.

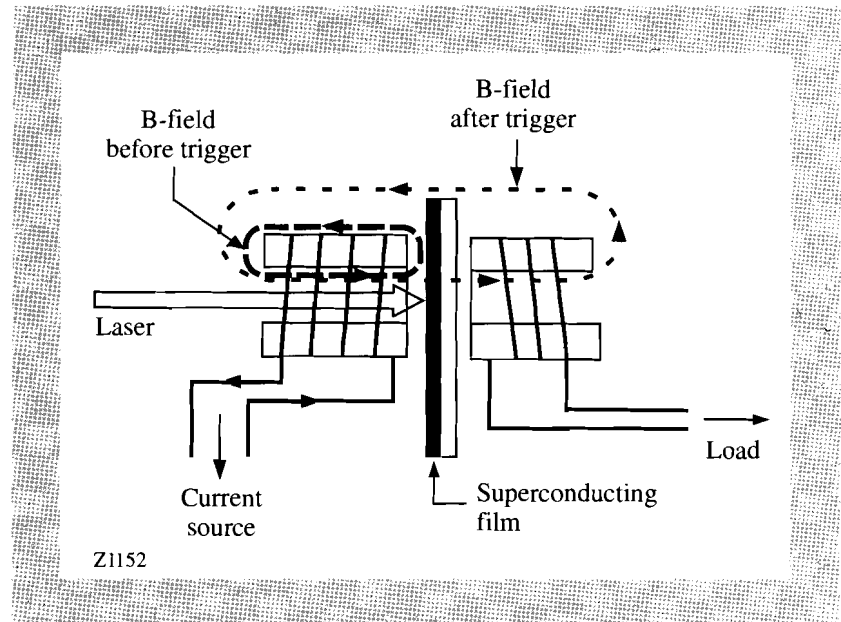


Fig. 54.10  
The superconducting, inductively coupled opening switch.

In the superconducting state the film isolates the secondary coil from the primary coil. Under illumination by a laser pulse the film makes a transition to the normal state, and the magnetic flux produced by the primary current couples to the secondary coil. The temporal change of flux through the secondary coil results in an induced voltage ( $V = d\phi/dt$ ) across the load.

In this switch there are no electrical contacts to the film. Therefore, the problem of low-resistance contacts to the high- $T_c$  superconductor, which limits the performance of the photoresistive switch, does not arise in this design.<sup>1,6</sup>

### Experimental Results

Some preliminary experiments have confirmed the inductively coupled switching. In these experiments, the coils were made from insulated 40 G copper wire. Since the mutual inductance drops drastically with the separation between the coils, flat, washer-shaped coils were used. Thin YBCO films, with thickness varying from 500 nm to 800 nm, were deposited on heated MgO substrates (1 cm  $\times$  1 cm) by rf magnetron sputtering.<sup>4</sup> The film surface was protected by a

12- $\mu\text{m}$  Teflon sheet, and two identical coils were placed on either side of the sample. The inner diameter of each washer-shaped coil was 3 mm and the outer diameter was approximately 6 mm, depending on the number of turns. A 100-turn coil had an inductance of 50  $\mu\text{H}$ .

The switch was mounted on the cold finger inside an optical-access cryostat. Light from a Nd:YAG laser illuminated the film. The voltage across the secondary coil was measured above and below  $T_c$  using sinusoidal input. The output voltage above  $T_c$  was found to be more than 20% of the input voltage indicating 20% coupling for identical primary and secondary coils. As the sample was cooled through the transition, the coupling decreased to less than 1%. For our samples the coupling dropped from 20% (which was found to be the same at room temperature and at the onset of transition) to less than 1% in a temperature range of 2 K. This indicates that at least 95% of the flux coupling to the secondary coil was screened by the superconducting film.

Instead of a dc current, 5- $\mu\text{s}$  pulses at low duty cycle were applied to avoid joule-heating the primary. The current pulse was synchronized in time with the laser pulse such that each laser pulse arrived at the center of a current pulse. The primary current pulse serves two purposes. First, it introduces flux in the primary for a period of 5  $\mu\text{s}$  and then turns it off, producing a positive and a negative voltage pulse across the secondary load corresponding to its leading and trailing edges. Above  $T_c$  these voltage pulses are indicative of the amount of flux coupled to the secondary coil and can be used to compare with the optical response. Second, it is long enough so that the optical effects take place during a time when the primary current produces a constant (dc) flux. When the film was cooled below  $T_c$ , the amplitude of these pulses was greatly reduced because of flux screening by the superconductor. We observed a voltage pulse at the load when the switch was irradiated with a laser pulse. This shows that the optical heating caused a transition of the film to the normal state and the flux to couple to the secondary coil. The amount of flux coupling varied with laser fluence (Fig. 54.11). By varying the laser fluence we were able to vary the amount of heating

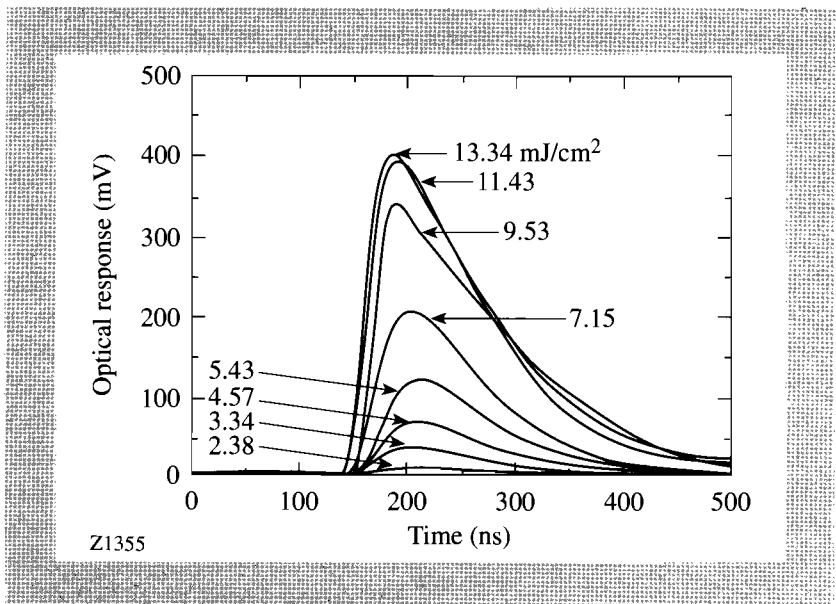
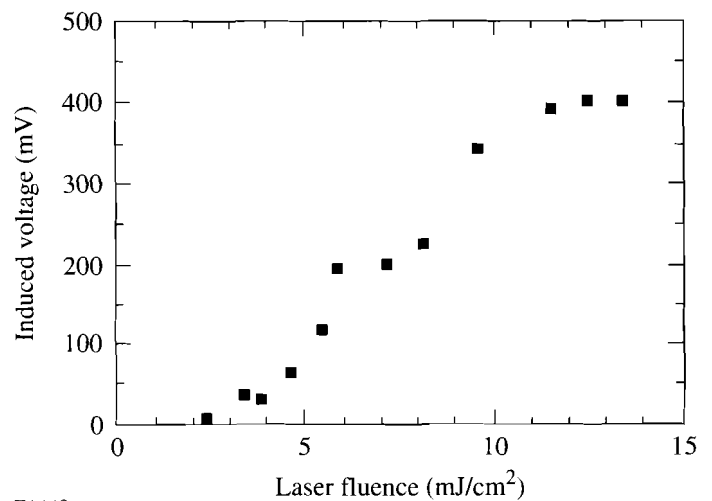


Fig. 54.11  
Photoinduced switching observed in the switch of Fig. 54.10 showing the induced voltage at the secondary coil for varying laser fluence. The temperature is 76 K, and the laser trigger occurs at  $\approx 140$  ns.

of the film. The coupled flux (and hence the induced voltage) increased as the film was heated through the transition regime before saturating (Fig. 54.12). The saturation indicates that the film was fully in the normal state. The maximum induced voltage for optical triggering is approximately 400 mV. The rise times are 40 to 60 ns.

In these preliminary experiments we used the same multiturn coils for the primary coil and the secondary coil. With a 100-turn primary and a single-turn secondary,  $L_1$  and  $L_2$  will be 50  $\mu\text{H}$  and 5 nH, respectively. The output time constant will be  $5 \text{ nH}/50 \Omega = 100 \text{ ps}$ . This switch is based on a derivative effect. Therefore, the output current and voltages will also be much higher, as discussed in the previous section.



Z1449

Fig. 54.12

Peak of the photoinduced voltage as a function of laser fluence. Saturation above 12 mJ/cm<sup>2</sup> indicates complete transition of the film to the normal-conducting state under optical illumination.

### Conclusion

The superconducting, inductively coupled opening switch is a new approach to the switching problem. The superconducting film does not have any electrical contacts and acts as a flux screen isolating the load. The switch can be operated repetitively without any degradation of its performance. Optical triggering provides accurate timing and fast heating of the film. We have demonstrated the operation of this switch. The dependence of the optically induced secondary voltage on the laser fluence has been investigated. Rise times of 50 ns have been observed with multiturn secondary coils. For an optimally designed secondary coil, the switching time is predicted to be shorter, and since the switch is based on a derivative effect, the load current is also expected to be much higher.

## ACKNOWLEDGMENT

This work was supported by SDIO/IST through ONR Contract #N00014-92-J-1993, NSF #DMR-8913524, Rochester Gas and Electric, and New York State Energy Research and Development Authority.

## REFERENCES

1. D. Gupta, W. R. Donaldson, K. Kortkamp, and A. M. Kadin, in *Optically Activated Switching II* (SPIE, Bellingham, WA, 1992), Vol. 1632, p. 190.
2. S. K. Dhali and M. Mohsin, *Rev. Sci. Instrum.* **63**, 220 (1992).
3. T. Burke, J. Carter, M. Weiner, and N. Winsor, "Analysis of Current Multiplication Circuit Utilizing Programmed Inductive Elements (PIE)" (private communication); also presented at the IEEE's High Voltage Workshop, Monterey, CA, March 1988.
4. P. H. Ballentine, J. P. Allen, A. M. Kadin, and D. S. Mallory, *J. Vac. Sci. Technol. A* **9**, 1118 (1991).
5. J. H. Claasen, M. E. Reeves, and R. J. Soulen, Jr., *Rev. Sci. Instrum.* **62**, 996 (1991).
6. D. Gupta, W. R. Donaldson, K. Kortkamp, and A. M. Kadin, "Optically Triggered Switching of Optically Thick YBCO Films," presented at the 1992 Applied Superconductivity Conference, Chicago, IL, 23–28 August 1992, and to be published in *IEEE Transactions on Applied Superconductivity*.

## 2.D Strong $K_{\alpha}$ Emission in Picosecond Laser-Plasma Interactions

Since the development of ultrashort ( $\leq 1$ -ps), high-peak-power laser systems, it has been possible to produce plasma with the picosecond duration of x-ray emission.<sup>1,2</sup> A picosecond x-ray source may provide a useful probe of time-resolved phenomena with high temporal resolution. In ultrashort laser-plasma interactions, the relatively low x-ray conversion efficiency has been of particular concern. An increase of the conversion efficiency has been reported for the case of the laser pulse interacting with a preformed plasma, which has been created either by a small prepulse<sup>3,4</sup> or a substantial level of amplified spontaneous emission (ASE).<sup>5</sup> However, streak-camera measurements have shown that for a preformed plasma the x-ray pulse duration is much longer than in the case of a high-intensity-contrast laser pulse, i.e., no preformed plasma.<sup>1,6</sup> A plasma produced by a p-polarized, high-intensity-contrast laser pulse is a promising candidate for an ultrashort x-ray source with high efficiency since it absorbs as much as 60% to 70% of the incident laser light.<sup>2,7</sup> Measurements of the fast-ion blowoff indicated that a high fraction of the laser energy was carried by fast electrons.<sup>8</sup> Hot electrons penetrating the target may induce  $K_{\alpha}$  emission. Recently,  $K_{\alpha}$  emission induced by hot electrons has indeed been observed in ultrashort laser-plasma interactions.<sup>9,10</sup>

In this article details of  $K_{\alpha}$  emission observed in the interaction of a picosecond, high-intensity-contrast, p-polarized laser pulse with a Si substrate coated with 0.2  $\mu\text{m}$  to 2.5  $\mu\text{m}$  Al are reported. Hot electrons are found to be the dominant source for  $K_{\alpha}$  emission. The x-ray-source characteristics were inferred from high-resolution x-ray spectra, measurements of duration of emission, and source size. The analysis suggests that the  $K_{\alpha}$  emission may have the potential to generate shorter x-ray pulses than, for example, resonance line emission since its temporal evolution depends on mechanisms like hot-electron generation rather than on recombination and cooling processes in the plasma.

### Experimental Conditions

A chirped-pulse amplification and compression (CPAC) laser system<sup>11</sup> was used to generate 13-mJ, 1.3-ps, 1.05- $\mu\text{m}$  pulses. Recent improvements in the laser design,<sup>12</sup> including the installation of a saturable dye cell (Kodak 2595 dye) after the compression gratings, have increased the intensity contrast from  $10^3$  to  $5 \times 10^5$ . The duration of the prepulse is around 100 ps. The p-polarized laser light was focused onto the target at an angle of  $60^\circ$ . Because of the oblique incidence, the focal spot of the laser is elliptical with an area of  $12 \mu\text{m} \times 24 \mu\text{m}$  (1/e intensity), leading to an irradiance of  $4 \times 10^{15} \text{ W/cm}^2$  with a prepulse fluence of  $0.8 \text{ J/cm}^2$ . The target material consisted of polished Si bulk material coated with 0.2  $\mu\text{m}$  to 2.5  $\mu\text{m}$  Al. The x-ray yield was measured with x-ray positive-intrinsic-negative (PIN) diodes filtered with 6  $\mu\text{m}$  Al or 250  $\mu\text{m}$  Be. The PIN diodes filtered with Al are sensitive to photon energies in the range of 0.9 keV to 1.56 keV and 2.5 keV to 15 keV, the PIN diodes filtered with Be to photon energies in the range of 2.5 keV to 15 keV. The PIN diodes were mounted at  $0^\circ$  to  $20^\circ$  with respect to the target normal. It was crucial to shield the PIN diodes with magnetic fields; otherwise, hot electrons would contribute substantially to the PIN-diode signal. The x-ray spectra were recorded with a von Hamos crystal spectrograph,<sup>13</sup> which used a cylindrical pentaerythritol (PET) crystal with a 2-in. radius of curvature. The spectrograph collected the x-ray emission of the plasma at an angle of  $40^\circ$  with respect to the target normal. The calibration of the PET crystal and the Kodak double exposure film (DEF) was taken from published data.<sup>14,15</sup> The signal of the PIN diodes agreed within 20% with the calibration of the spectrograph, provided that (consistent with an aged crystal) a Bragg reflection integral close to the Darwin zero extinction limit<sup>14</sup> was assumed. About 30 shots were accumulated to obtain a single spectrum.

The duration of the x-ray emission was measured with an x-ray streak camera, which had a cathode made of a 2000- $\text{\AA}$  parylene layer coated with 500  $\text{\AA}$  Au and 1200  $\text{\AA}$  CsI. X-ray filters, i.e., 1.5  $\mu\text{m}$  Mylar, 6  $\mu\text{m}$  Al, and 25  $\mu\text{m}$  Be, were mounted in front of the streak-camera slit to get three channels with different spectral sensitivity. The Mylar channel detected soft x rays with photon energies exceeding 0.1 keV, the Be channel harder x rays above 1 keV, and the Al channel x rays from 0.9 keV to 1.56 keV and above 2.5 keV, respectively. Since no experimental value for the temporal resolution is currently available and an accurate calculation of the streak-camera response to short x-ray pulses is beyond the scope of this work, a somewhat simplified model, which assumes that the various broadening mechanisms are independent of each other and that the pulse shapes and secondary electron-energy distributions are Gaussian,<sup>16</sup> was adapted. The finite slit width and the secondary-electron energy distribution of

$\text{CsI}^{17}$  are predicted to limit the temporal resolution of the streak camera to  $\sim 7$  ps. Space charge effects, especially for high current densities at the cathode, will further increase this value. Better resolution would require a higher extraction field, a higher sweep speed, and a cathode material with a smaller secondary-electron energy distribution, for example,  $\text{KBr}$ .<sup>1</sup>

The source size of the x-ray emission was obtained from x-ray shadowgraphy, using a knife-edge technique.<sup>18</sup> A razor blade was placed between the plasma and a DEF film filtered with  $25 \mu\text{m}$  Be. The film was uniformly exposed, except for the region where the x-ray source was partially or completely covered by the razor blade. The derivative of the intensity distribution yielded the spatial-intensity profile of the x-ray source. An advantage of this setup is that for a fairly good signal-to-noise ratio a high spatial resolution can be achieved. In the experiment, the resolution was around  $2 \mu\text{m}$  and was mostly limited by the smoothing of the raw data, which was performed in the numerical analysis of the x-ray shadowgraph.

## Results and Discussion

### 1. X-Ray Yield

In the case of an Si target coated with  $0.2 \mu\text{m}$  Al and a high-intensity-contrast laser pulse, i.e., a prepulse irradiance below  $10^{10} \text{ W/cm}^2$ , resonance line emission ( $\text{He}_\alpha$ ), as well as strong  $\text{K}_\alpha$  emission from both target materials, is present (Fig. 54.13). The Al  $\text{K}_\alpha$  line from low ionization states of Al ( $\text{Al}^{1+} - \text{Al}^{4+}$ ) is at  $8.34 \text{ \AA}$ , and the “shifted” Al  $\text{K}_\alpha$  lines from  $\text{Al}^{5+} - \text{Al}^{10+}$  are seen between  $7.85 \text{ \AA}$  and  $8.32 \text{ \AA}$ . The  $\text{He}_\alpha$  line from He-like Al ( $\text{Al}^{11+}$ ) is at  $7.76 \text{ \AA}$ . In the range  $6.64 \text{ \AA}$  to  $7.13 \text{ \AA}$ , similar to Al lines, are the Si  $\text{K}_\alpha$  lines (shifted and unshifted) and the Si  $\text{He}_\alpha$  line. The Al  $\text{He}_\alpha$  line is emitted from the hot plasma ( $k_B T_e \sim 300 \text{ eV}$ ) on the target surface. The Si and Al  $\text{K}_\alpha$  emissions originate from colder material inside the target.

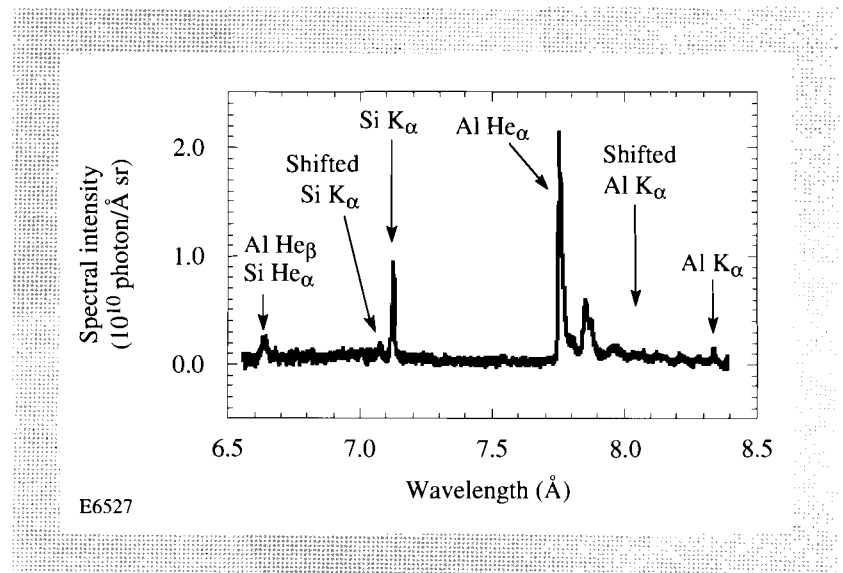


Fig. 54.13

Spectrum from an Si target coated with  $0.2 \mu\text{m}$  Al, taken with a high-intensity-contrast laser pulse.

The  $K_{\alpha}$  emission accounts for 55% of the emission into the spectral range from 6.5 Å to 8.5 Å. The total x-ray conversion efficiency into this range is  $2 \times 10^{-3}\%/sr$ . The Si  $K_{\alpha}$  emission contributes  $3 \times 10^{-4}\%/sr$ . The conversion efficiency for the Al  $He_{\alpha}$  line of  $8 \times 10^{-4}\%/sr$  is somewhat lower than the value of  $8 \times 10^{-3}\%/sr$  recently measured for a laser system with an ASE intensity below  $10^{10} \text{ W/cm}^2$ .<sup>5</sup> We believe that this may be caused by the shorter wavelength (0.248 μm) of this laser system, i.e., higher critical density, which may enhance collisional absorption of laser light, and a higher irradiance ( $10^{17} \text{ W/cm}^2$ ), which may result in a higher temperature and thus a higher fraction of He-like Al ions in the plasma.

The PIN diode filtered with 6 μm Al is mostly sensitive to Al  $K_{\alpha}$  emission and 2.5-keV to 15-keV continuum emission since the Al  $He_{\alpha}$  line and the Si  $K_{\alpha}$  emission are strongly absorbed in the filter. Figure 54.14 shows the signal of this diode as a function of angle of incidence and polarization of laser light for a laser energy of 13 mJ and an Si target coated with 2.5 μm Al. The contribution of the 2.5-keV to 15-keV continuum emission to the detected x-ray signal was measured with a PIN diode filtered with 250 μm Be and was found to be 30%. Most of the x-ray signal is therefore caused by Al  $K_{\alpha}$  emission; in Fig. 54.14 one unit of the y axis corresponds approximately to  $3 \times 10^6 \text{ keV/sr}$  of Al  $K_{\alpha}$  emission.

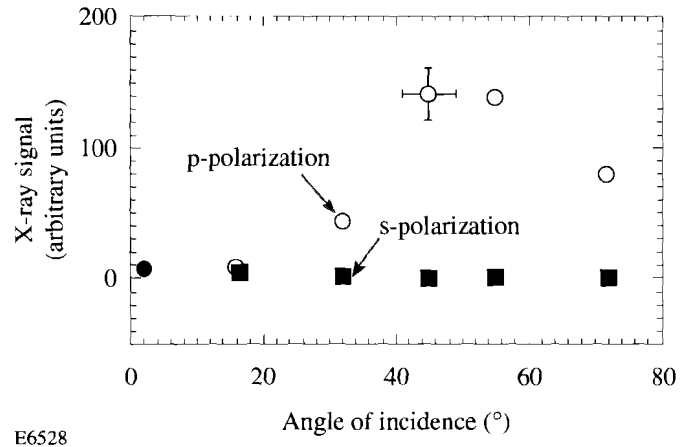


Fig. 54.14  
Signal of a PIN diode filtered with 6 μm Al as a function of angle of incidence and polarization for high-intensity-contrast, 13-mJ laser pulses and an Si target coated with 2.5 μm Al. One unit on the y axis corresponds approximately to  $3 \times 10^6 \text{ keV/sr}$  of Al  $K_{\alpha}$  radiation.

The x-ray emission is seen to be maximum for p-polarized light at angle of incidence of around 50°. For s-polarized light, maximum x-ray emission is observed at perpendicular incidence. Nevertheless, the yield for s-polarization is more than one order of magnitude lower than the maximum yield observed for p-polarization. The strong polarization dependence at 50° is consistent with absorption measurements, which showed that 50% of p-polarized and 20% of s-polarized light are absorbed, respectively.<sup>7</sup>

The spectrum and the PIN diode filtered with 25 μm Be indicate that approximately  $10^9 \text{ keV/sr}$  of x rays with photon energies above the binding energy of an Si K-shell electron are emitted. From this we estimate that the

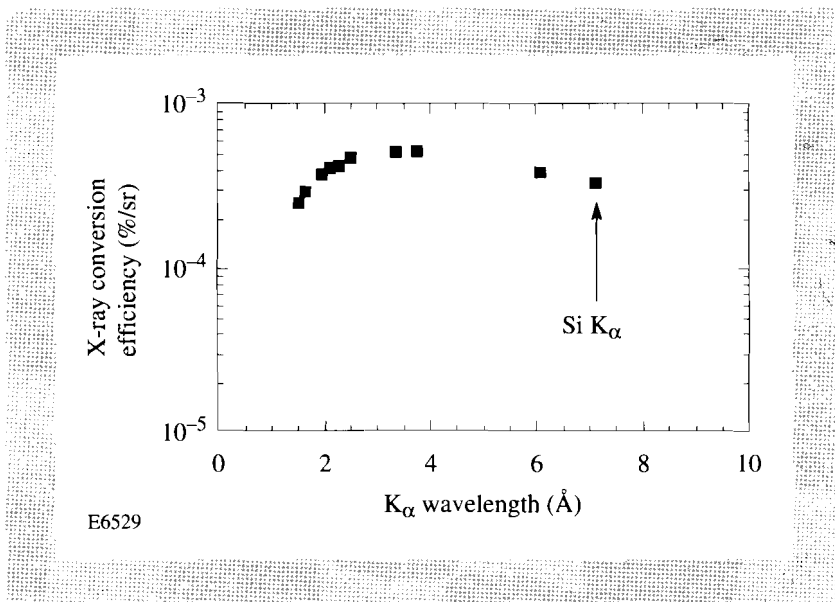
radiation-induced Si  $K_{\alpha}$  yield is at most 10% of the measured value. Therefore, hot electrons appear to be the dominant source for the  $K_{\alpha}$  emission. A Monte Carlo code was adapted to predict the  $K_{\alpha}$  yield per electron as a function of angular distribution and energy distribution of the hot electrons, the thickness of the Al layer, and the  $Z$  number of the substrate material.<sup>19</sup> In the simulations, backscattered electrons were recycled, i.e., they were made to reenter the target from the front, consistent with the reflection of hot electrons in the plasma sheath. It was further assumed that the target was a neutral solid. This limits, to some extent, the applicability of the predictions to measured data since the shifted  $K_{\alpha}$  emission indicates (especially in the case of Al) that the material is partially ionized (Fig. 54.13). The hot-electron distribution may be characterized by comparing the code predictions to the observed dependence of the Si  $K_{\alpha}$  yield on the thickness of the Al layer. In a previous experiment we found that a beamlike monoenergetic electron source as well as a plane-isotropic electron source with a Maxwellian energy distribution results in a good fit to the experimental data.<sup>10</sup> Nevertheless, in the following analysis we will mostly concentrate on a Maxwellian energy distribution. This is reasonable since our measurements of the fast-ion blowoff of the plasma indicated Maxwellian-distributed electrons with a temperature scaling like  $k_B T_h \sim 1.77 \times 10^{-5} I^{0.35}$  with  $k_B T_h$  in keV and the irradiance  $I$  in  $\text{W}/\text{cm}^2$ .<sup>8</sup> A similar scaling law is predicted in particle-in-cell (PIC) simulations for resonantly heated electrons and  $L/\lambda \sim 0.1$ , where  $L$  is the density scale length and  $\lambda$  is the laser wavelength.<sup>20</sup> A process like resonance absorption may also explain the strong dependence of the Al  $K_{\alpha}$  emission on angle of incidence and polarization of laser light observed in our experiment (Fig. 54.14). Recently, a similar dependence of the x-ray yield, integrated over a much wider spectral range, has been observed and attributed to a process with the characteristics of resonance absorption.<sup>2</sup>

For an estimate of the hot-electron temperature  $k_B T_h$  we will use the scaling law obtained from our fast-ion measurements<sup>8</sup> and PIC simulations<sup>20</sup> rather than the value recently measured from the slope of the Si  $K_{\alpha}$  yield versus Al thickness<sup>10</sup> since the latter experiment was done with slightly different experimental parameters. For an irradiance of  $4 \times 10^{15} \text{ W}/\text{cm}^2$  we calculate  $k_B T_h \sim 5 \text{ keV}$ . By matching the predicted Si  $K_{\alpha}$  yield per electron to the measured yield, we estimate that for electrons with a temperature of 5 keV, 25% of the laser energy is deposited into the target. For 10-keV electrons 15% is calculated. On the other hand, measurements of the ion blowoff also showed that less than 5% of the laser energy appeared in the fast ions. This indicates that most of the hot-electron energy is deposited into the target.

For substrates with a higher  $Z$  number the  $K_{\alpha}$  emission shifts toward shorter wavelength. Figure 54.15 shows the x-ray conversion efficiency predicted by Monte Carlo simulations for various  $Z$ -substrates coated with  $0.2 \mu\text{m}$  Al as a function of  $K_{\alpha}$  wavelength. In the simulation, 5-keV electrons carrying 25% of the laser energy were assumed for all target configurations since the characteristics of the hot electrons are predominantly determined by the interaction of the laser pulse with the Al layer. It can be seen that at  $1.5 \text{ \AA}$ , i.e., for Cu  $K_{\alpha}$  emission, the x-ray conversion efficiency is still above  $2 \times 10^{-4} \text{ %/sr}$  and thus comparable to the value for the Si  $K_{\alpha}$  emission.

Fig. 54.15

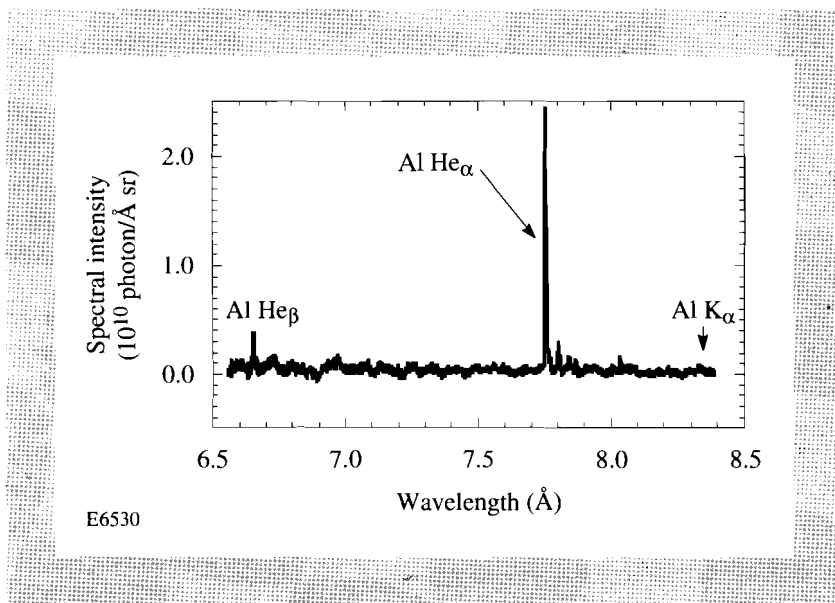
Predicted x-ray conversion efficiency into  $K_{\alpha}$  emission as a function of  $K_{\alpha}$  wavelength. The substrate materials are coated with  $0.2 \mu\text{m}$  Al. 25% of the laser energy is absorbed by hot electrons with a temperature of 5 keV.



The spectrum taken for a low-intensity-contrast laser pulse, i.e., a prepulse irradiance of  $\sim 4 \times 10^{12} \text{ W/cm}^2$ , shows mostly Al  $\text{He}_{\alpha}$  emission but hardly any Al and Si  $K_{\alpha}$  emission (Fig. 54.16). The  $\text{He}_{\alpha}$  line is approximately 10% higher than in the case of a high-intensity-contrast laser pulse (Fig. 54.13), but the total x-ray emission into the spectral range of  $6.5 \text{ \AA}$  to  $8.5 \text{ \AA}$  is 60% lower. Since a low-intensity contrast will result in a preformed plasma, the scale length of the plasma interacting with the main pulse is longer than for a high-intensity-contrast laser pulse. In long-scale-length plasma resonance absorption is expected to be less efficient at the relatively large angle of incidence chosen in this experiment.<sup>21</sup> In addition, other absorption mechanisms, like inverse bremsstrahlung absorption that does not generate significant numbers of hot electrons, may be dominant. Therefore the  $K_{\alpha}$  production shows a strong dependence on the level of prepulse.

Fig. 54.16

Spectrum from an Si target coated with  $0.2 \mu\text{m}$  Al, taken with a low-intensity-contrast laser pulse.



## 2. Temporal Evolution of X-Ray Emission and X-Ray Source Size

The streak-camera recordings of the x-ray emission from an  $\text{SiO}_2$  target coated with  $0.6 \mu\text{m Al}$  are shown in Fig. 54.17 for a high-intensity-contrast laser pulse. From the PIN-diode measurements and the spectral sensitivity of  $\text{CsI}^{22}$  we estimate that  $\sim 80\%$  of the signal of the Al channel is caused by Al  $\text{K}_\alpha$  emission, and  $\sim 50\%$  of the signal of the Be channel is caused by Al  $\text{He}_\alpha$  emission. The streak-camera measurements indicate a duration of 10 ps (FWHM) for the Be channel and 8 ps for the Al channel. The actual duration of emission may well be shorter than 10 ps and 8 ps, respectively, since a temporal resolution of the streak camera of around 7 ps will broaden the detected signal. The Mylar channel indicates that the soft x-ray emission lasted around 20 ps. In the case of a low-intensity-contrast laser pulse both the Be channel and the Mylar channel show a longer duration of emission, i.e., 13 ps and 70 ps, respectively. The Al channel detected no signal, consistent with the low levels of Al  $\text{K}_\alpha$  emission observed in the spectrum for a low-intensity-contrast laser pulse (Fig. 54.16).

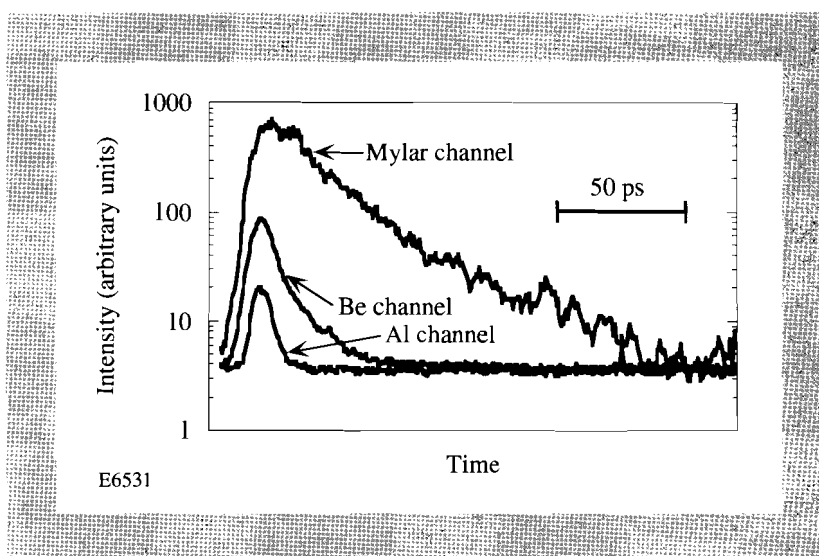


Fig. 54.17  
Streak-camera trace from an  $\text{SiO}_2$  target coated with  $0.6 \mu\text{m Al}$ , taken with a high-intensity-contrast laser pulse. The temporal evolution of the Mylar, Be, and Al channels is shown.

Even for a high-intensity contrast the duration of the  $\text{He}_\alpha$  line is longer than the laser-pulse duration itself; it depends on recombination processes and the cooling of the plasma. On the other hand, the duration of the  $\text{K}_\alpha$  emission is determined by time scales of processes, such as hot-electron production, energy deposition, and lifetime of excited ions. In the case of hot electrons generated by wavebreaking, an upper limit for the time elapsed between the end of the laser pulse and the end of hot-electron production may be estimated from the damping time of the plasma wave. For collisional damping, the damping rate roughly equals the electron-ion collision frequency,<sup>23</sup> which is around  $10^{14} \text{ s}^{-1}$  at critical density for a 300-eV temperature. Hot electrons are thus probably generated only during the interaction of the laser pulse with the plasma. For hot electrons penetrating the target, the time scale of the energy deposition may be estimated in the nonrelativistic case from the stopping time in the target.<sup>24</sup> Electrons with a temperature of 5 keV are predicted to have an average stopping time of 0.2 ps.

The excited states involved in the  $\text{K}_\alpha$  emission process have a short lifetime (femtosecond range).<sup>25</sup> Therefore, the duration of the  $\text{K}_\alpha$  emission is probably

dominated by the time scale of the hot-electron generation and should be below a few picoseconds, consistent with the duration of the measured signal in the Al channel. Nevertheless, the effect of self-generated magnetic fields, especially at higher irradiance, on the x-ray pulse duration may require further investigations to explain the duration of Al  $K_{\alpha}$  emission recently observed in other experiments.<sup>26</sup>

The x-ray shadowgraph indicated that the plasma region emitting x rays above  $\sim 1$  keV is approximately equal to the focal spot of the laser. No direct evidence for substantial  $K_{\alpha}$  emission from a much larger area, as would be expected for lateral transport, could be found.

### Conclusions

We have observed strong  $K_{\alpha}$  emission in high-intensity-contrast, picosecond, p-polarized laser-plasma interactions. The  $K_{\alpha}$  emission was found to be induced by hot electrons. The strong dependence of the  $K_{\alpha}$  emission on angle of incidence and polarization of laser light is consistent with hot electrons generated by resonance absorption. With a duration of emission of  $\leq 8$  ps, a source area of  $1.6 \times 10^{-6} \text{ cm}^2$ , and an x-ray yield at  $7.1 \text{ \AA}$  of  $1.5 \times 10^8$  photon/sr, a radiance of  $\geq 3 \times 10^9 \text{ W/cm}^2 \text{ sr}$  is calculated. This value is three orders of magnitude lower than the radiance of the Al  $L_{\alpha}$  line recently reported for a  $0.3\text{-}\mu\text{m}$ , 290-fs laser system at a much higher irradiance of  $5 \times 10^{18} \text{ W/cm}^2$ .<sup>27</sup> Nevertheless,  $K_{\alpha}$  emission has the potential to generate shorter x-ray pulses than, for example, resonance line emission because its duration of emission depends on processes such as hot-electron production and energy deposition rather than on recombination and cooling processes in the plasma.

The  $K_{\alpha}$  emission is a promising candidate to obtain an efficient, ultrashort x-ray source at short wavelength. The analysis suggested that, for example, Cu  $K_{\alpha}$  emission ( $\lambda \sim 1.5 \text{ \AA}$ ) may be obtained at an irradiance of  $4 \times 10^{15} \text{ W/cm}^2$ . By choosing the appropriate fluor material and laser intensity, the x-ray conversion efficiency as well as the  $K_{\alpha}$  wavelength may be further optimized.

### ACKNOWLEDGMENT

This work is supported by the U.S. Department of Energy Office of Inertial Confinement Fusion under Cooperative Agreement No. DE-FC03-92SF19460 and the University of Rochester and by the Swiss National Science Foundation. The support of the DOE does not constitute an endorsement by DOE of the views expressed in this article.

### REFERENCES

1. M. M. Murnane, H. C. Kapteyn, and R. W. Falcone, *IEEE J. Quantum Electron.* **25**, 2417 (1989).
2. U. Teubner *et al.*, *Phys. Rev. Lett.* **70**, 794 (1993).
3. H. W. K. Tom and O. R. Wood II, *Appl. Phys. Lett.* **54**, 517 (1989).
4. U. Teubner, G. Kühnle, and F. P. Schäfer, *Appl. Phys. Lett.* **59**, 2672 (1991).
5. J. A. Cobble *et al.*, *J. Appl. Phys.* **69**, 3369 (1991).
6. J. C. Kieffer, *Bull. Am. Phys. Soc.* **37**, 1468 (1992).
7. S. Uchida, H. Chen, Y.-H. Chuang, J. A. Delettrez, and D. D. Meyerhofer, *Bull. Am. Phys. Soc.* **36**, 2304 (1991).

8. D. D. Meyerhofer, H. Chen, J. Delettrez, B. Soom, S. Uchida, and B. Yaakobi, to be published in *Physics of Fluids B*.
9. P. Audebert *et al.*, *Europhys. Lett.* **19**, 189 (1992).
10. H. Chen, B. Soom, B. Yaakobi, and D. D. Meyerhofer, submitted to *Physical Review Letters*.
11. P. Maine, D. Strickland, P. Bado, M. Pessot, and G. Mourou, *IEEE J. Quantum Electron.* **24**, 398 (1988).
12. Y.-H. Chuang, D. D. Meyerhofer, S. Augst, H. Chen, J. Peatross, and S. Uchida, *J. Opt. Soc. Am. B* **8**, 1226 (1991).
13. B. Yaakobi, R. E. Turner, H. W. Schnopper, and P. O. Taylor, *Rev. Sci. Instrum.* **50**, 1609 (1979).
14. R. Hall *et al.*, *X-Ray Spectrom.* **8**, 20 (1979).
15. B. L. Henke *et al.*, *J. Opt. Soc. Am. B* **3**, 1540 (1986).
16. M. M. Murnane, H. C. Kapteyn, and R. W. Falcone, *Appl. Phys. Lett.* **56**, 1948 (1990).
17. B. L. Henke, J. Liesegang, and S. D. Smith, *Phys. Rev. B* **19**, 3004 (1979).
18. Ph. Alaterre *et al.*, *Opt. Commun.* **49**, 140 (1984).
19. B. Luther-Davies, A. Perry, and K. A. Nugent, *Phys. Rev. A* **35**, 4306 (1987).
20. P. Gibbon and A. R. Bell, *Phys. Rev. Lett.* **68**, 1535 (1992).
21. K. G. Estabrook, E. J. Valeo, and W. L. Kruer, *Phys. Fluids* **18**, 1151 (1975).
22. B. L. Henke, J. P. Knauer, and K. Premaratne, *J. Appl. Phys.* **52**, 1509 (1981).
23. W. L. Kruer, *The Physics of Laser Plasma Interactions* (Addison-Wesley, Redwood City, CA, 1988), Vol. 73.
24. B. Soom, H. Chen, and D. D. Meyerhofer, in *Short-Pulse High-Intensity Lasers and Applications II* (SPIE, Bellingham, WA, 1993), Vol. 1860, to be published.
25. T. W. Tunnell, C. Can, and C. P. Bhalla, *J. Quant. Spectrosc. Radiat. Transfer* **27**, 405 (1982).
26. J. C. Kieffer, in *Short-Pulse High-Intensity Lasers and Applications II* (SPIE, Bellingham, WA, 1993), Vol. 1860, to be published.
27. G. A. Kyrala *et al.*, *Appl. Phys. Lett.* **60**, 2195 (1992).

## 2.E Angular Distributions of High-Order Harmonics from Low-Density Gas Targets

High-order harmonics have been observed during laser-atom interactions at a number of different laser wavelengths with short-pulse, high-intensity laser systems. Harmonics with frequencies in excess of 100 times the laser frequency have been reported.<sup>1-3</sup>

Most high-order, harmonic-generation experiments to date have used gas target pressures in excess of 10 Torr. These high pressures have been used to enhance the harmonic signal, which increases quadratically with the pressure. The phase-mismatch factors (caused by both neutral and ionized media) increase with the pressure as does the effect of refraction of the incident laser when the medium becomes ionized. Very few measurements of the angular distributions of the high-order harmonics have been reported.<sup>3</sup> The far-field pattern can provide additional insight into the laser propagation, phase matching, and the atomic response.

Phase-matching effects have been extensively studied by L'Huillier and co-workers.<sup>1,4-7</sup> They have made many detailed comparisons of their calculations with their experiments and have found excellent agreement. Their studies have included the effect of the intensity, pressure, and focusing characteristics (both confocal parameter and jet position relative to the focus) on the spatially and temporally integrated harmonic output. Faldon *et al.*<sup>8</sup> have been able to explain the temporal history of the harmonic emission by considering the effects of ionization and phase matching.

In this article, observations of the angular (far-field) distribution of high-order harmonic generation with a low-density gas target with gas pressures of the order of 0.5 Torr are presented. With the  $f/70$  focal system and 1-mm-thick target, the phase-mismatch factors from neutral gas, free electrons, and geometric effects are all less than  $\pi$ . Thus, in these experiments, the high-order harmonics are generated under conditions where the effects of phase mismatch on the harmonic generation should be minimized. The goal of this work is to separate the atomic response from the effects of phase matching. In the experiments presented in this article, the far-field distribution of the 11th to 21st harmonics of the incident laser radiation has been observed. The article is organized as follows: The laser system and the detector are described first, followed by the onset of refraction, which constrains the experimental conditions. Next, the angular distributions of the high-order harmonics are presented, followed by a comparison of the measurements with the predictions of lowest-order perturbation theory. Finally, the conclusions are presented. (The gas target is described in Sec. 2.F.)

### Experimental Conditions

The high-order harmonics are observed by focusing a 1- $\mu\text{m}$ , 1.5-ps laser into a moderate-density gas target ( $p \sim 0.5$  Torr, thickness  $\sim 1$  mm) and then detecting the harmonics with a transmission grating coupled to an MCP-phosphor image intensifier. A schematic of the experiment is shown in Fig. 54.18. The various

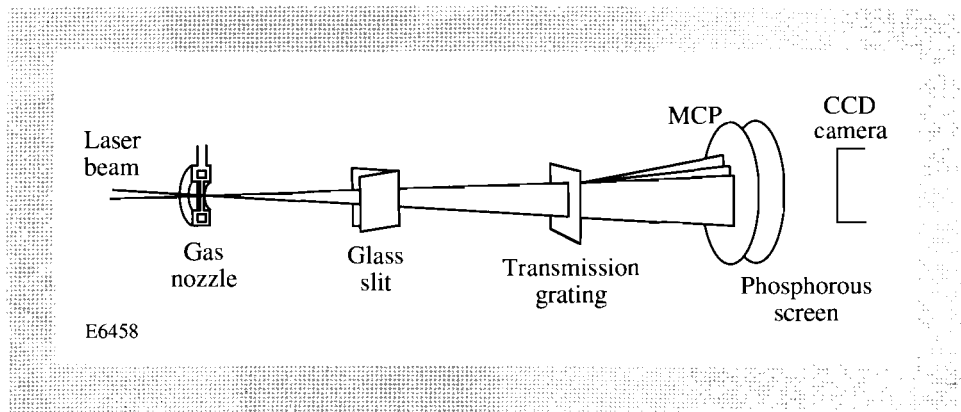


Fig. 54.18  
Schematic of the experimental setup, including the gas target and the angularly resolved spectrometer.

components of the experimental setup are discussed in this section, as is the effect of refraction on the operating conditions.

The 1- $\mu\text{m}$ , 1.5-ps laser pulses used to generate the harmonics are generated with an Nd:glass, chirped-pulse-amplification laser system,<sup>9,10</sup> which has been described in detail elsewhere.<sup>11</sup> We have recently upgraded the energy capability and focusing quality of the system.

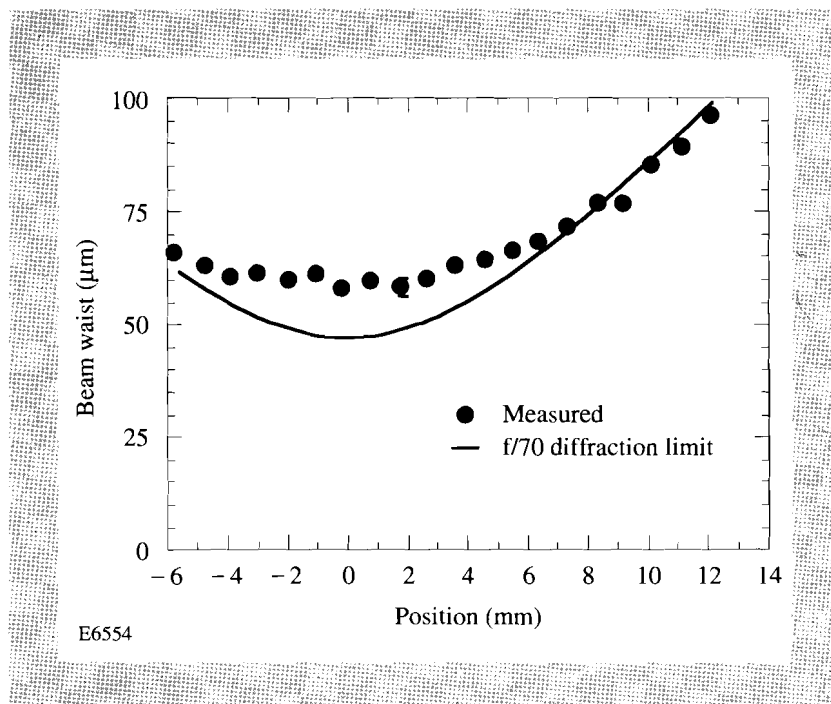
For these experiments, a long Rayleigh range is desired to minimize the geometric phase-matching effects on the high-order harmonics. To increase the  $f$ -number of the focusing system, a smaller-than-usual, 1.1-cm-radius beam is produced by the laser system. Under these conditions, the laser energy is limited to less than 300 mJ to avoid  $B$ -integral effects and to operate significantly below the compression-grating damage threshold. This beam is focused with a 153-cm lens to produce an  $f$ -number of 70. While the use of the long-focal-length lens sacrifices peak field intensity, the system is still able to achieve  $3 \times 10^{15}$  W/cm<sup>2</sup> with relatively large focal volumes and low field gradients. The experiments are currently limited to much lower energies because of plasma formation in the spectrometer.

The focal spot diameter is 1.2 times diffraction limited. The focal characteristics of the laser were measured by direct imaging, with 4X magnification, onto a CCD camera. The focal-spot radius as a function of the axial distance along the focus is shown in Fig. 54.19, as is the calculated radius for a diffraction-limited  $f/70$  beam.

The spectrometer used in these experiments consists of a slit with approximate dimensions of  $500 \mu\text{m} \times 2.5 \text{ cm}$  followed by a bare gold wire transmission grating, consisting of 0.5- $\mu\text{m}$ -diam gold wires, separated by 1  $\mu\text{m}$  (center to center). The slit is aligned parallel to the grating wires. Following the grating is a microchannel-plate (MCP), image-intensified phosphor screen (Galileo model 8081). The microchannel-plate intensifier is not UV enhanced so it cannot detect harmonics lower than the ninth. The light incident on the slit and grating is dispersed by the grating and produces spectral lines on the phosphor screen. The different harmonic orders are separated in the direction perpendicular to the grating lines, and their angular distributions are observed parallel to the slit. Thus information about the far-field pattern as well as the spectral content of the harmonics is obtained simultaneously. At this time, the spectrometer is not

Fig. 54.19

Plot of the measured laser-beam waist as a function of axial position along the focus, showing that the beam is 1.2 times diffraction limited with  $f/70$  optics.



absolutely calibrated so only relative levels of harmonic emission are presented. In all cases, the same relative units are used. The relatively large slit allows a larger photon flux to reach the detector at the cost of reduced spectral resolution. In the configuration used for the experiments presented in this article, the harmonic lines begin to overlap with the 23rd harmonic.

The gas target is designed to create well-characterized, narrow gas distributions at low densities (1–2 Torr or less with backing pressures up to 5–10 Torr).<sup>12</sup> This low-density regime is desirable to reduce the phase-matching effects during the harmonic generation<sup>5</sup> and the effects of refraction of the focused laser beam. Also, the low backing pressure has the advantage of reducing the possibility of dimer formation in gases such as Xe.<sup>13</sup>

The target and its calibration are described in more detail in the next article in this volume. The gas target is 1 mm thick and typically operated at pressures of 1 Torr or less. One important goal of the experiments is to operate in a regime where the laser propagation through the target is unaffected by the medium. This makes the interpretation of the experimental results easier. A laser propagating through an ionized medium may undergo refraction or self-focusing. The laser was focused through the gas target and imaged onto a CCD camera with various xenon gas pressures in the target and with various peak laser intensities. The results are shown in Fig. 54.20. Figures 54.20(a)–54.20(c) show the change in effective focal spot with increasing laser intensity at 0.6-Torr pressure. At the highest intensity xenon is fully ionized within the focal volume.<sup>14</sup> At this low pressure, the focal spot is identical to that observed in the vacuum. When the pressure is increased to 2 Torr as in Figs. 54.20(d)–54.20(f), an apparent decrease in the focal volume is observed. This is caused by refraction, which decreases the  $f$ -number of the laser as it leaves the gas target. Preliminary calculations of the refraction under these conditions are consistent with the observed results.

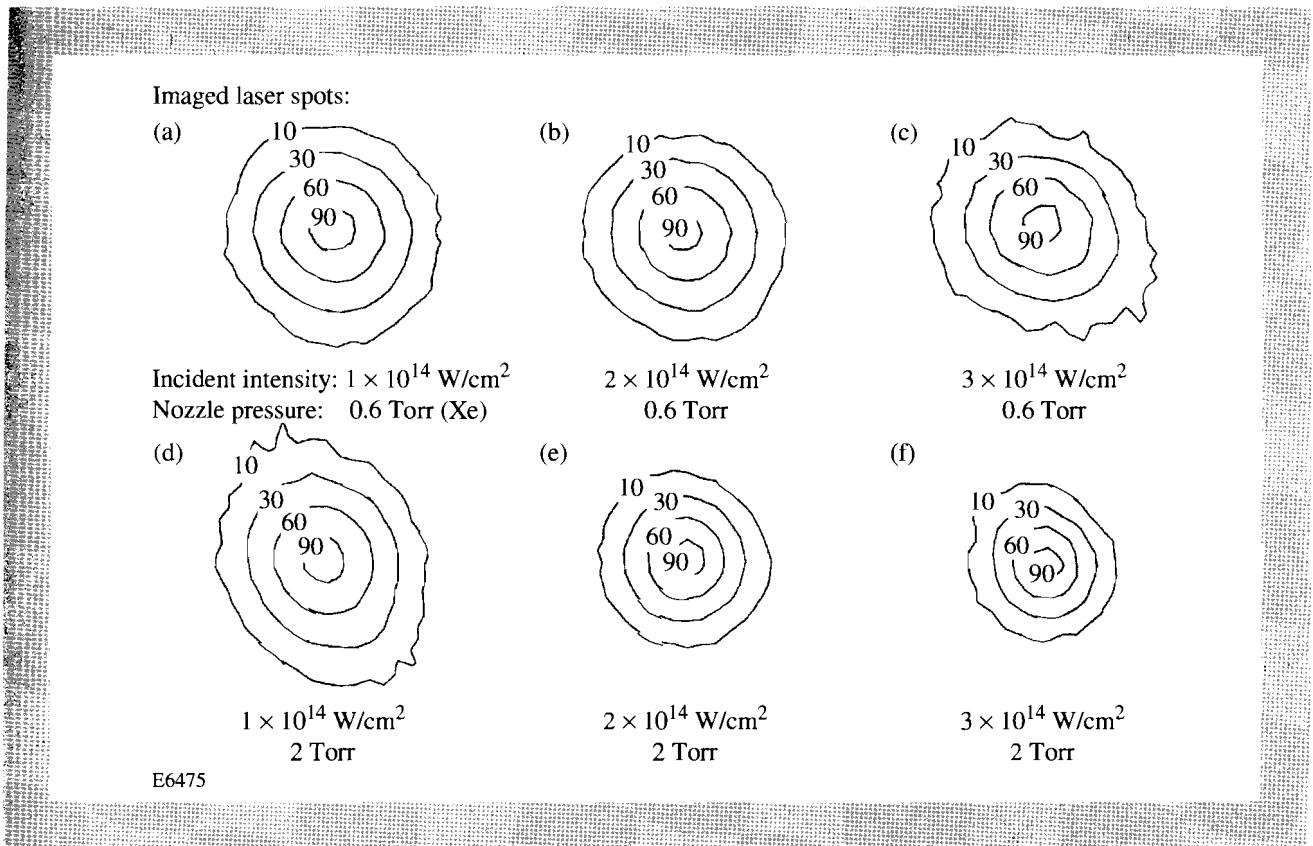


Fig. 54.20

Images of the laser focus as a function of laser intensity and gas target pressure. Figures 54.20(a)–54.20(c) show increasing laser intensity at 0.6 Torr of xenon pressure, and Figs. 54.20(d)–54.20(f) show the same for 2 Torr of xenon.

**Harmonic Far-Field Distributions**

The experimental conditions previously described have been chosen to minimize the phase-mismatch factors.<sup>5</sup> The combination of  $f/70$  focusing and a thin gas target (1 mm) means that the target thickness is much less than the 12-mm confocal parameter. In addition, the low gas pressures of  $\sim 0.5$  Torr mean that the phase mismatch from neutral Xe and free electrons is minimal. Table 54.I shows that the phase-mismatch factors for various harmonic orders are less than or of the order of 1 rad.

Table 54.I: Phase-mismatch factors  $\Delta kL$  (radians).

Harmonic order	9	13	17	21
Neutral Xe	0.08	-0.05	-0.08	-0.08
Free electrons	0.50	0.70	0.90	1.10

E6543

Figure 54.21 shows the far-field (angular) distribution of the 11th to 21st harmonics of the laser at an intensity of  $9 \times 10^{13} \text{ W/cm}^2$  and a gas target peak pressure of 0.3 Torr xenon. These results are typical of the harmonic profiles under these conditions. Most of the high-order harmonics have a very narrow angular structure. For xenon under these conditions, large-scale shoulder structures appear on the 13th harmonic. The shoulders are also observed on the 15th harmonic in krypton and the 17th in argon. While the strongest shoulders are observed on the 13th harmonic in xenon, recent, more sensitive experiments have shown shoulders on other harmonics as well.

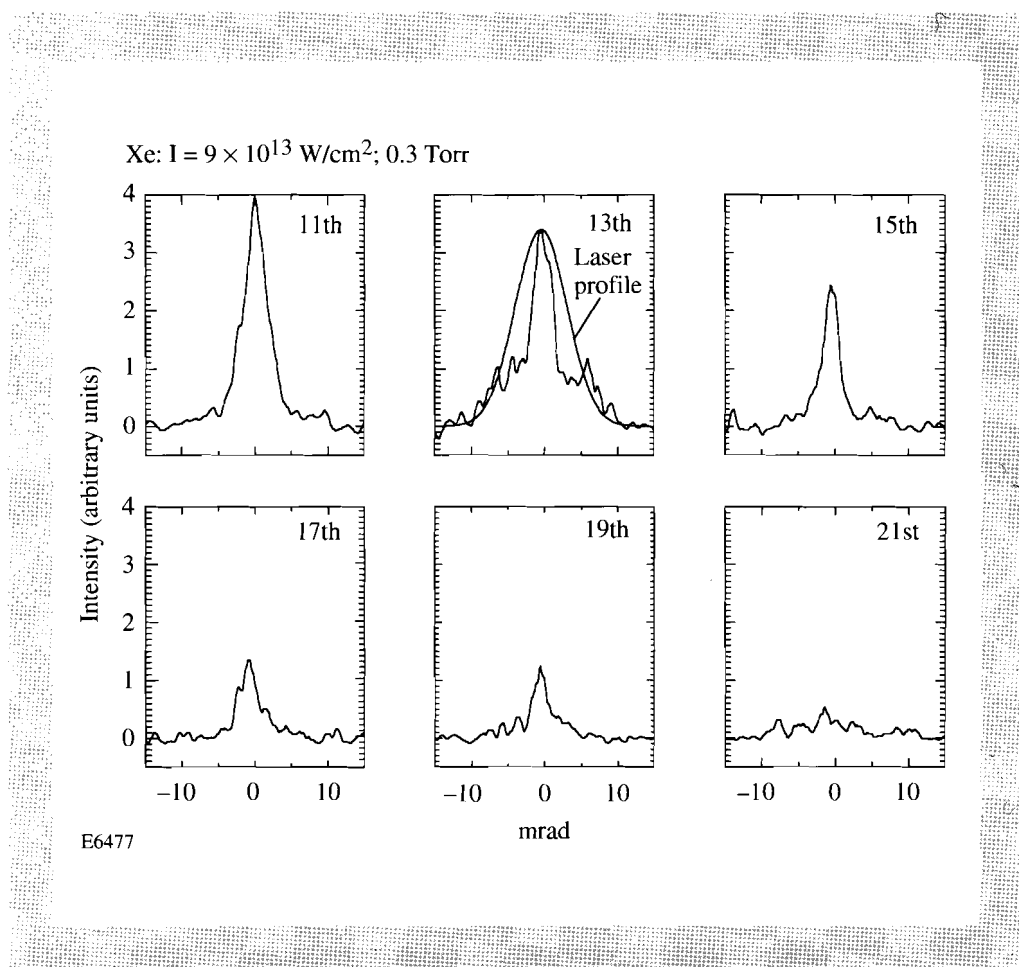


Fig. 54.21

Typical far-field distribution of the 11th to 21st harmonic observed for 0.3 Torr of xenon at  $9 \times 10^{13} \text{ W/cm}^2$ .

The relative energy in the different harmonics is determined by integrating the harmonic emission radially, taking the circularly symmetric nature of the emission into account:

$$E_q = \int_0^{\infty} 2\pi I(r) r dr .$$

The emission is symmetric around the peak signal level. Figure 54.22 shows the relative energy in the 11th to 23d harmonics in xenon at a gas pressure of 0.5 Torr for three different intensities. The development of a plateau in the harmonic emission with increasing intensity is evident.

Under perfect phase-matching conditions, the integrated harmonic intensity should scale as  $N^2$ , where  $N$  is the number of atoms in the focal volume for a fixed intensity. Figure 54.23 shows the integrated energy for the 11th to 21st harmonic in xenon at  $9 \times 10^{13} \text{ W/cm}^2$  at four different gas pressures. The overall shape of the harmonic-energy spectrum is maintained, and the energy of each harmonic scales quadratically with pressure as expected.

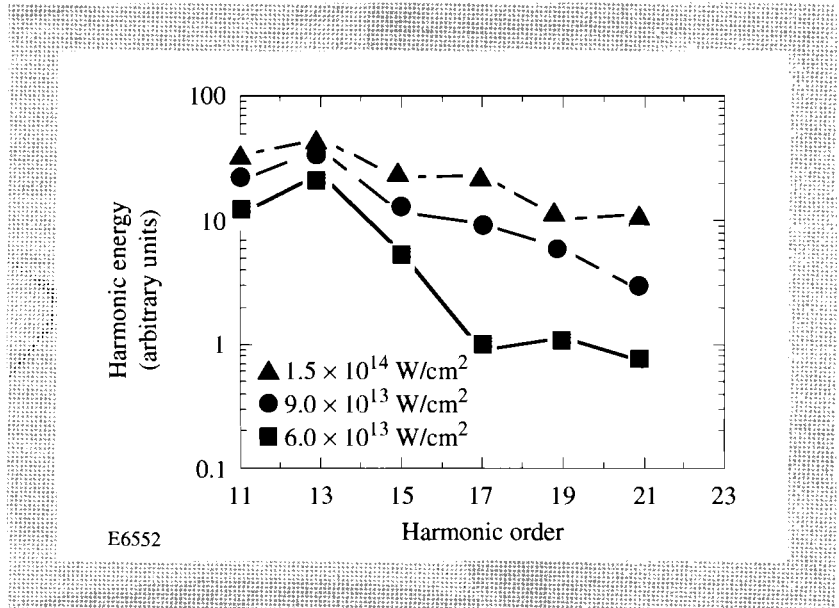


Fig. 54.22

Relative-harmonic energy in the 11th to 21st harmonic in xenon at 0.5 Torr and three different intensities.

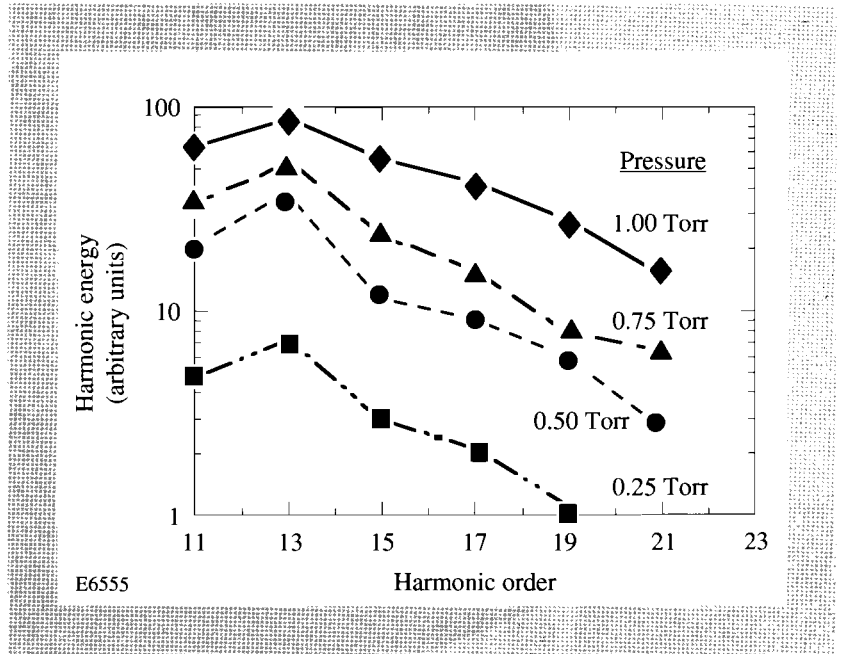


Fig. 54.23

Integrated energy for the 11th through 21st harmonic for xenon at  $9 \times 10^{13} \text{ W/cm}^2$  for four different gas pressures.

One of the features common to all of the low-pressure, far-field distributions is the development of significant shoulders, which appear most pronounced on one particular harmonic first. This is evident in the 13th harmonic in xenon in Fig. 54.21. The far-field emission for Xe, Kr, and Ar is shown in Fig. 54.24. For Kr and Ar, the shoulders appear on the 15th and 17th harmonics, respectively. In this case, the intensity is approximately the barrier suppression ionization threshold (BSI),<sup>15</sup> and the gas target density has been scaled so that the level of emission is similar in each case. At the BSI threshold, the ionization probability has been observed to be approximately 1% for 1.5-ps, 1- $\mu\text{m}$  laser pulses.<sup>14,15</sup> It is important to note the similarities among the far-field patterns of the different harmonics. Each of the harmonics shows the same shapes. In fact, the angular distributions are almost identical. The primary difference is the harmonic on which the shoulders first appear. These results are summarized in Table 54.II. The pronounced structure appears on the harmonic, which is one order ( $2\omega_L$ ) higher than the first with energy greater than the field-free atomic ionization potential.

### Comparisons with Lowest-Order Perturbation Theory

Fig. 54.24  
Comparison of the far-field emission for Xe, Kr, and Ar with the intensity at the BSI threshold.

With the exception of the harmonic, which shows the shoulder-like structure, the far-field patterns are quite narrow and seem to get narrower with increasing harmonic order. We can compare the far-field widths with the predictions of

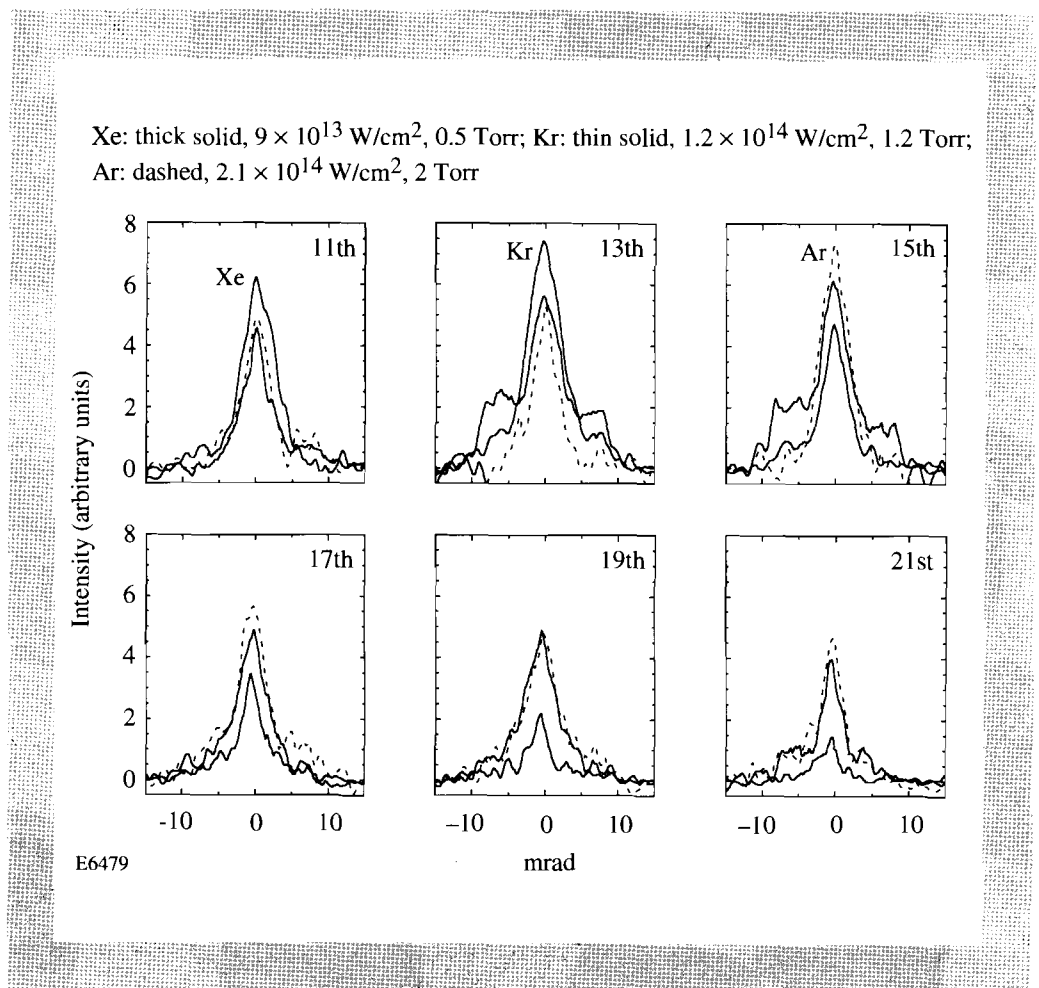
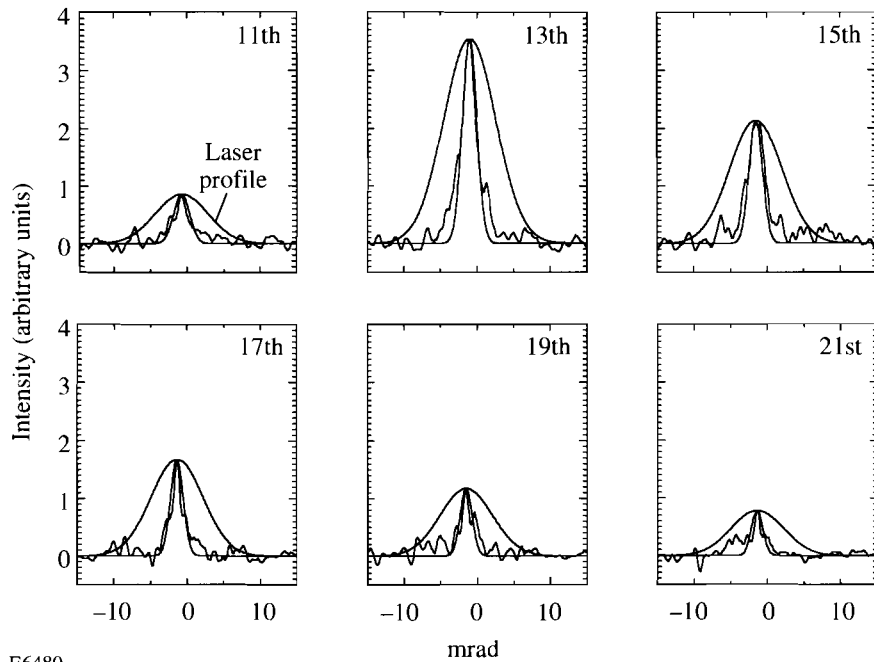


Table 54.II: Comparison of harmonic structure in different target gases.

Target Gas	BSI Intensity <sup>15</sup>	Experimental Intensity	First Harmonic Showing Structure
Xenon	$8.6 \times 10^{13} \text{ W/cm}^2$	$9 \times 10^{13} \text{ W/cm}^2$	13
Krypton	$1.5 \times 10^{14} \text{ W/cm}^2$	$1.2 \times 10^{14} \text{ W/cm}^2$	15
Argon	$2.5 \times 10^{14} \text{ W/cm}^2$	$2.1 \times 10^{14} \text{ W/cm}^2$	17

E6544

lowest-order perturbation theory (LOPT). The harmonic intensity is assumed to vary as  $I^q$ . The angular width of the harmonics is then expected to vary as  $\delta\theta_0 / \sqrt{q}$ , where  $\delta\theta_0$  is the angular distribution of the laser. The observed harmonic emission for Kr at 0.5 Torr and  $10^{14} \text{ W/cm}^2$  is compared with the LOPT predictions in Fig. 54.25. Good agreement with the far-field patterns of all the harmonics is observed. It should be noted though, that the relative intensity of each harmonic does not scale with intensity as LOPT would predict.



E6480

Fig. 54.25 Comparison of the far-field emission for Kr at 0.5 Torr and  $1 \times 10^{14} \text{ W/cm}^2$  with the predictions of lowest-order perturbation theory.

## Conclusion

The far-field pattern of high-order harmonics has been observed under conditions where the geometric and propagation phase-mismatch factors should be negligible. Under these conditions, we find that the far-field pattern (though not the intensity scaling) is consistent with lowest-order perturbation theory, except for one harmonic (the 13th in xenon, the 15th in Kr, and the 17th in Ar). The harmonic emission scales quadratically with the pressure and, even under these low-pressure conditions, a plateau develops, as has been observed in many other experiments.

## ACKNOWLEDGMENT

This work is supported by the National Science Foundation under contract PHY-9200542. Additional support was provided by the U.S. Department of Energy Office of Inertial Confinement Fusion under Cooperative Agreement No. DE-FC03-92SF19460 and the University of Rochester. The support of DOE does not constitute an endorsement by DOE of the views expressed in this article.

## REFERENCES

1. A. L'Huillier and Ph. Balcou, *Phys. Rev. Lett.* **70**, 774 (1993).
2. J. J. Macklin, J. D. Kmetec, and C. L. Gordon III, *Phys. Rev. Lett.* **70**, 766 (1993).
3. R. A. Smith *et al.*, "Recent Ultra-High Harmonic Generation Experiments with Picosecond Laser Pulses," to be published in the *Proceedings of the NATO Workshop on Super-Intense, Laser-Atom Physics*, edited by B. Piraux, Han-sur-Lesse, Belgium, 8–14 January 1993.
4. A. L'Huillier, K. J. Schafer, and K. C. Kulander, *Phys. Rev. Lett.* **66**, 2200 (1991).
5. A. L'Huillier, K. J. Schafer, and K. C. Kulander, *J. Phys. B: At. Mol. Opt. Phys.* **24**, 3315 (1991).
6. A. L'Huillier, P. Balcou, and L. A. Lompré, *Phys. Rev. Lett.* **68**, 166 (1992).
7. A. L'Huillier *et al.*, *Phys. Rev. A* **46**, 2778 (1992).
8. M. E. Faldon *et al.*, *J. Opt. Soc. Am. B* **9**, 2094 (1992).
9. D. Strickland and G. Mourou, *Opt. Commun.* **56**, 219 (1985).
10. P. Maine, D. Strickland, P. Bado, M. Pessot, and G. Mourou, *IEEE J. Quantum Electron.* **24**, 398 (1988).
11. Y.-H. Chuang, D. D. Meyerhofer, S. Augst, H. Chen, J. Peatross, and S. Uchida, *J. Opt. Soc. Am. B* **8**, 1226 (1991).
12. J. Peatross and D. D. Meyerhofer, submitted to *Review of Scientific Instruments*.
13. L. A. Lompré *et al.*, *J. Appl. Phys.* **63**, 1791 (1988).
14. S. Augst, D. D. Meyerhofer, D. Strickland, and S. L. Chin, *J. Opt. Soc. Am. B* **8**, 858 (1991).
15. S. Augst, D. Strickland, D. D. Meyerhofer, S. L. Chin, and J. H. Eberly, *Phys. Rev. Lett.* **63**, 2212 (1989).

## 2.F Novel Gas Target For Use in Laser Harmonic Generation

Generation of high-order harmonics from laser-atom interactions is complicated because it involves both the single-atom response to the driving laser field and the collective-atom enhancement or deterioration of the signal caused by the phase matching of the emitted harmonic light. Much theoretical work has been done toward understanding the single-atom, harmonic-generation reaction, and phase-matching effects are understood in principle.<sup>1</sup> Experimental work in this field has shown good agreement with theory;<sup>2,3</sup> however, a number of unanswered questions remain. To interpret the experimental results, both the laser and gas distribution must be well characterized. The gas-distribution geometry strongly affects the production of the harmonic light. For physical interest, the distribution of the gas ideally would be as narrow and as low density as possible to reduce the role of phase matching so that the single-atom response in harmonic generation is more apparent. This is particularly true if free electrons are created by ionization during the interaction. In the case of free electrons, a severe phase mismatching can occur if the gas pressure is too high, i.e., 1- $\mu\text{m}$  light traveling 1 mm through free electrons at 10 Torr will undergo a phase shift that is equal to a phase shift of  $7\pi$  for the 21st harmonic.

High-order, harmonic-generation experiments traditionally have been carried out by focusing a laser into a gas jet.<sup>1-5</sup> The gas jet relies on the principles of fluid flow to propel gas from its orifice in a thin stream where the laser can intersect with the narrow distribution of gas. Lompré *et al.*<sup>6</sup> measured the characteristics of such a gas jet. They were able to produce a 1-mm gas distribution with a peak pressure of 25 Torr. A gas jet must operate at a sufficiently high pressure to ensure a narrow stream of flow. Typically the backing pressure of the jet is hundreds of torr while the usable region of the jet is of the order of tens of torr. A lower pressure causes a more diffuse gas distribution in the plume, making the phase matching in the experiment more difficult.<sup>1</sup> In any case, the density of the gas expelled from a jet varies as a function of distance from the orifice, the distribution becoming broader as the distance increases. This can make the systematic alignment of the intersection between the laser and the gas jet a somewhat difficult and tedious task.

Details of a gas target designed to create well-characterized, narrow gas distributions at low densities (1–2 Torr or less with backing pressures up to 5–10 Torr) are presented. This low-density regime is desirable to reduce the phase-matching effects during the harmonic generation.<sup>1</sup> Also, the low backing pressure has the advantage of reducing the possibility of dimer formation in gases such as Xe.<sup>6</sup> High-order, harmonic-generation results using this target are described in the previous article in this volume.

The gas target is a small cylindrical hole through which the focused laser passes and inside of which gas enters from the middle. Because the laser beam goes through the target, the alignment of the device is comparatively simple. The gas target operates on the principle of molecular flow instead of the principle of

fluid flow, as does the gas jet. Since the flow rate is relatively low, the target can be operated in a continuous rather than a pulsed mode. The density of the gas within the hole remains relatively high while the gas outside the hole disperses quickly (inverse square of the distance from the hole edge). The target operation is limited to low densities just as the gas jet is limited to high densities. If the gas in the target hole is at too high a pressure, plumes may develop out its ends that would lie on top of the incoming and outgoing laser beam. The jet and the target are thus complementary in the sense that they operate in opposite ranges of pressure.

The gas distribution in the target is characterized experimentally. It is perhaps more difficult to characterize than the jet since the gas densities are much lower, and the off-axis line of sight to the interaction region is obstructed by the target itself. However, the gas-density profile can be measured in the region just inside the target opening and outward. There is good agreement between the measurement and a calculation of the gas distribution using a Monte Carlo computer simulation of free molecular flow. The same calculation also predicts the gas-flow rate from the target. The flow rate has been measured for two gas-target designs. In both cases, there is good agreement between the predicted and the measured gas-flow rates.

### **Gas-Target Design**

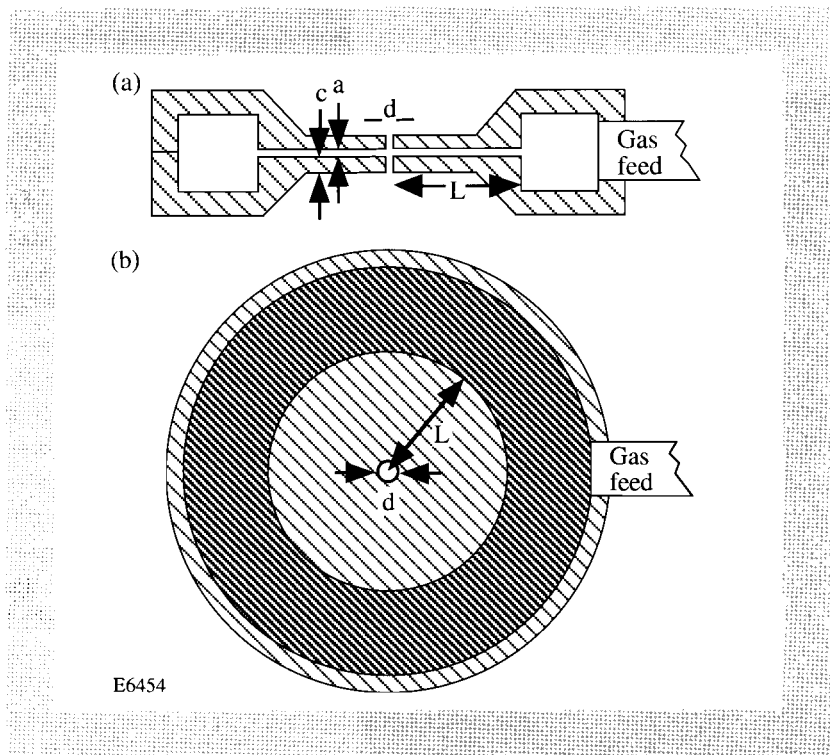
The gas target consists of two identically machined, cylindrical aluminum pieces glued together with a thin layer of vacuum epoxy. Aluminum is chosen because of its ease of machining. Figure 54.26(a) shows a cut-away portion of the two pieces (upper and lower) already attached around the outer rim. Figure 54.26(b) shows the inside of a single piece so that the cylindrical symmetry is observable. Gas flows from the outer ring-shaped pocket into the gap between the thinly spaced plates and toward the hole at the center. The gas then escapes out both ends of the hole. When gluing the pieces together, the drill bit that made the holes is inserted through both pieces to ensure alignment. As shown in Fig. 54.26,  $a$  is the separation of the plates,  $c$  is the thickness of the plates,  $d$  is the hole diameter, and  $L$  is the length from the hole center to the inside edge of the outer gas pocket. Typical values for these are  $a = 0.2$  mm,  $c = 0.4$  mm,  $d = 0.5$  mm, and  $L = 4$  mm.

### **Molecular-Flow Range**

A gas that flows within a boundary such as a pipe or some other confining shape is in the molecular-flow range if the collisional mean free path of the particles is longer than the characteristic dimension of the boundary, such as a pipe diameter. Knudsen's number ( $Kn$ ) is the ratio of a gas particle's collisional mean free path to a typical dimension of the boundary. Pure molecular flow begins when  $Kn > 1$ . This regime of gas flow is the best understood. The flow of gas in this range is completely determined by the geometry of the walls and can be calculated numerically using a Monte Carlo averaging technique.<sup>7,8</sup> The standard assumption is that a gas particle travels in a straight path until encountering a wall, where it is re-emitted at some new angle. Because of the molecular coarseness of almost any surface, the new direction of the particle has virtually no correlation with the incident direction. Therefore, when the particle strikes a surface, it is as likely to go back toward where it came from as it is to

Fig. 54.26

(a) A cutaway view of the two cylindrical gas-target pieces glued together at their outer rims. Gas is fed into the outer ring-shaped pocket. (b) An inside view of a single gas-target piece showing the ring-shaped pocket from which the gas flows across the thin plate toward the center hole.



continue forward through the system. The distribution of the rebound is generally taken to go as the cosine to the surface normal. This assumption has been experimentally verified for various geometries.<sup>8</sup> The problem is usually treated in terms of throughput; that is, for a given system, how likely is a particle that enters one end of the system to emerge out the other end? Harmonic-generation experiments often employ the noble gases. The room-temperature mean free paths of the lighter noble gases are 2 mm, 1 mm, 0.8 mm, 0.6 mm, and 0.4 mm for He, Ne, Ar, Kr, and Xe, respectively, at 0.1-Torr pressure.<sup>8</sup> For the purposes of this article, these numbers should be compared with the typical dimension of the gas-target center (0.5 mm). The mean free path scales inversely with pressure.

The fluid flow regime begins when  $Kn < 0.01$ . The flow of the gas in this range behaves very differently from molecular flow. In the fluid flow regime the intraparticle collisions rather than particle-wall collisions dominate the flow of the gas. The regime in between fluid and molecular flow is not well understood. In this case both types of collisions have importance; however, if the value of  $Kn$  is nearer to one or the other of the flow ranges, the properties of the flow should be qualitatively similar. Therefore, it is likely that much of the dispersive nature of molecular gas flow is preserved even with  $Kn$  as low as 0.1.

### Calculation of Trajectories in a Monte Carlo Simulation

This section describes the details necessary for numerically simulating molecular flow through the target. The particles are assumed to move in straight lines between encounters with the target walls. Intraparticle collisions are ignored. Particles enter the region between the thinly spaced plates of the target from the ring-shaped gas pocket at a distance  $L$  from the center [refer to Fig. 54.26 throughout this section]. When particles hit the target walls, they rebound in

some new direction, and their trajectory paths are recorded. Each particle propagates until it either exits the target opening or returns to the ring-shaped gas pocket.

The various straight segments of a particle's trajectory are represented by equations of straight lines. The more natural coordinate system for straight lines is Cartesian, wherein the equations for a straight line in three dimensions can be written as  $x = m_x z + b_x$  and  $y = m_y z + b_y$ . The azimuthal symmetry of the target also requires the use of cylindrical coordinates, which are obtained with the transformations  $r = \sqrt{x^2 + y^2}$  and  $\phi = \tan^{-1}(y/x)$ , where  $\phi \rightarrow \phi + \pi$  if  $x < 0$ . The  $z$  axis is chosen to lie along the target axis of symmetry, and the origin is taken to be the target center. When the particle encounters the planar surface of the interior of one of the thinly spaced plates, the position of impact is found from  $z' = \pm a/2$ . The standard assumption at this point is that the particle leaves the surface with a Lambertian distribution.<sup>8</sup> This is the same distribution as produced by an ideal gas escaping from a small hole in a thin-walled container. Under the diffuse-rebound assumption, the slopes for the new line emerging from the point on the planar surface are given by

$$m'_x = \tan \alpha \cos \beta \quad \text{and} \quad m'_y = \tan \alpha \sin \beta, \quad (1)$$

where  $\alpha$  and  $\beta$  are given by  $\alpha = \sin^{-1}(Rnd_1)$  and  $\beta = 2\pi(Rnd_2)$ .  $Rnd_1$  and  $Rnd_2$  indicate two independent random numbers that have values between 0 and 1. The new  $z$ -plane intercepts are calculated by

$$b'_x = b_x + (m_x - m'_x)z' \quad \text{and} \quad b'_y = b_y + (m_y - m'_y)z'. \quad (2)$$

This completes the cycle, and the equations for the new particle flight path are defined. These are then used to find the next point of impact with the target wall.

A collision of the particle with the interior of the target's cylindrical hole is more complicated. The  $z$ -value at the point of impact is given by

$$z' = \frac{-(m_x b_x + m_y b_y) \pm \sqrt{(m_x b_x + m_y b_y)^2 - (m_x^2 + m_y^2)(b_x^2 + b_y^2 - (d/2)^2)}}{m_x^2 + m_y^2}; \quad (3)$$

recall that  $d$  is the hole diameter. The azimuthal coordinate of the point of impact is

$$\phi = \tan^{-1} \frac{m_y z' + b_y}{m_x z' + b_x}, \quad \text{where} \quad \phi \rightarrow \phi + \pi \quad \text{if} \quad m_x z' + b_x < 0. \quad (4)$$

The slopes for the new line emerging from this point under the diffusive rebound assumption is calculated by

$$m'_x = \frac{\sin \phi \tan \alpha \cos \beta - \cos \phi}{\tan \alpha \sin \beta} \quad \text{and} \quad m'_y = -\frac{\cos \phi \tan \alpha \cos \beta + \sin \phi}{\tan \alpha \sin \beta}, \quad (5)$$

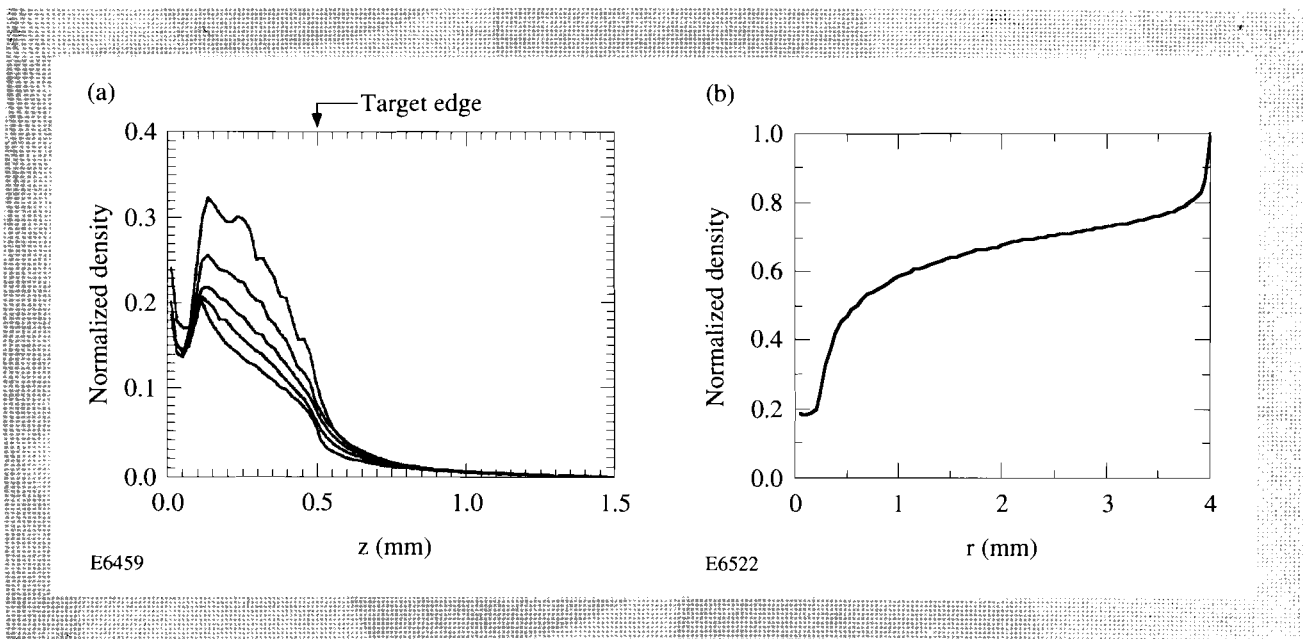
where  $\alpha$  and  $\beta$  are given the same as before, following Eq. (1). Again, the new  $z$ -plane intercepts are calculated by Eq. (2), and the cycle is complete. The trajectory for the particle leaving the point of impact is defined, and the process can be repeated.

The initial position for a particle's trajectory is at the inside edge of the ring-shaped pocket at  $r = L$ , where the gas density is assumed to be known. The direction of the initial path is distributed randomly over the half-sphere that points toward the target center. The slopes for this path are calculated by Eq. (5) but with  $\alpha = \cos^{-1}(R/d_1)$ . Because of azimuthal symmetry it is not essential to randomly choose  $\phi$ , but for conceptual completeness we take  $\phi = 2\pi R/d_3$ . The starting  $z$ -position is given by  $z_0 = a(R/d_4 - 1/2)$ , and the  $z$ -plane intercepts are determined by  $b_x = L \cos \phi - m_x z_0$  and  $b_y = L \sin \phi - m_y z_0$ . Each particle propagates from the input position until it either goes out the target hole or returns to the ring-shaped gas pocket at radius  $L$ . The flow rate of the particles can be determined from the ratio of the number of particles that successfully exit the target to the total number of trial particles. The density of the gas as a function of position is obtained by summing over the intersections of all the particle trajectories with each elemental volume of the target.

**Calculation of Gas Density within the Gas Target**

The gas distribution in a target has been calculated using the Monte Carlo computer simulation of free molecular flow described in the previous section. The dimensions of the target in the simulation were  $a = 0.2$  mm,  $c = 0.4$  mm,  $d = 0.5$  mm, and  $L = 4$  mm (see Fig. 54.27). The number of particles propagated through the system was such that 10,000 successfully exited the hole. The throughput probability for an individual particle was 0.014, which later will be used to find the gas-flow rate. This small number indicates that very few particles entering the system actually exit the target opening before returning to the starting point (1 in 70). This can be understood in part by the relative sizes of the

Fig. 54.27  
 (a) The density of the gas as a function of  $z$  (the cylindrical axis) for five different radii uniformly spaced inside the target hole. The origin is at the target center. The density is relative to the density of gas backing the device. (b) The distribution of gas particles in the target as a function of radius ( $z = 0$ ) from the target center out to the inside edge of the gas pocket ( $r = 4$  mm), where the density is assigned a value of 1. The target hole's cylindrical wall is at  $r = 0.25$  mm.



entrance and exit areas (a factor-of-16 difference). Figure 54.27(a) shows the density of the gas as a function of  $z$  (the cylindrical axis) for five different radii uniformly spaced inside the center hole. The density is normalized to the density at the inside edge of the ring-shaped gas pocket (length  $L$  from the center), where the backing pressure is known. As can be seen, the density is only weakly dependent on radius. Along the  $z$  axis, the density falls off sharply at the edge of the hole (located at 0.5 mm). The reason for this sharp drop is that the particles within the hole tend to have a strong radial component to their velocity so that when they exit the hole into the free vacuum, they quickly spread away from the  $z$  axis. Figure 54.27(b) shows the particle density as a function of radius for  $z = 0$ . Again the density is normalized to that in the ring-shaped pocket, so that at a radius of 4 mm (the boundary with the pocket) the density is 1. From there, the density continually drops until inside the target opening ( $r < 0.25$  mm), where the density on average is  $\sim 0.2$ .

### Gas-Flow Rate

The flow rate of gas through the target can be derived from the throughput probability calculated using the Monte Carlo technique previously described. The number of particles that exit the nozzle per time is

$$\dot{N} = \rho (A\delta) \left( \frac{v_{mf}}{4\delta} \right) \gamma, \quad (6)$$

where  $\rho$  is the backing particle density,  $A$  is the entrance area at the edge of the ring-shaped gas pocket ( $2\pi aL$ ),  $v_{mf}$  is the mean-free velocity of the particles, and  $\gamma$  is the throughput probability. Introduced here briefly for conceptual convenience,  $\delta$  is a small thickness that when multiplied onto the entrance area creates an element of volume. The factor of 4 in the denominator comes about since only half the particles within the volume element are moving in a direction that will take them into the plates, and their component of velocity normal to the entrance is on average one-half the mean-free velocity. Replacing  $\rho$  by  $N/V$ , where  $V$  is the fixed backing volume, and solving the differential equation yields

$$N = N_0 \exp \left\{ - \frac{A\gamma v_{mf}}{4V} t \right\}. \quad (7)$$

Since pressure is proportional to the number of particles, Eq. (7) applies as well to pressure. A useful term for comparison with experimental measurement is the time it takes for the pressure to drop by a factor of 2. The half-life of the pressure is

$$t_{\text{half}} = \frac{4 \ln 2 V}{\gamma A v_{mf}}. \quad (8)$$

This theoretical result can be compared with experimental measurements as a check of the model.

A gas target with the same dimensions as used in the numerical simulations has been tested. The half-lives of the backing pressure in our system predicted by Eq. (8) for He, Ar, and Xe were 6 s, 19 s, and 35 s, respectively; we measured 9 s, 25 s, and 45 s. The measurements were taken at the pressures where the molecular flow range was expected to begin for the various gases. The backing pressures were 1 Torr, 0.5 Torr, and 0.3 Torr, respectively. Recall that the pressure at the target center is a factor of 5 below the backing pressure (see Fig. 54.27). For each gas, the flow rate approximately doubled when four times the backing pressure was applied. Higher backing pressures produced faster flow rates since intraparticle collisions began to reduce the randomness to the direction in which the particles drifted through the target. However, these pressures were still very far below the viscous flow regime. At lower pressures, the gas flow slowed because the walls and tubes in our backing system began to play a significant role.

To further test the accuracy of the model, a different gas target with the dimensions of  $a = 0.12$  mm,  $c = 0.17$  mm,  $d = 0.35$  mm, and  $L = 3.0$  mm (see Fig. 54.26) was tested. The calculated throughput probability was 0.013, which for our system predicted a pressure half-life of 43 s for Ar; the measured half-life was 35 s. The good agreement between predicted and measured flow rates lends confidence to the accuracy of the model.

### Sensitivity of Gas Flow and Density to the Nature of the Surfaces

The question arises—how sensitive is the flow of gas in the target to the material nature of the walls. In other words, how good is the assumption that the particles rebound from the walls of the target with a Lambertian distribution. To answer the question, the Monte Carlo simulation was modified to allow a fraction of the particle-surface rebounds to be specular or mirror-like. For a specular reflection with the planar surface, the new slopes, rather than those of Eq. (1), are given simply by  $m'_x = -m_x$  and  $m'_y = -m_y$ . For a specular reflection off the interior surface of the cylindrical hole, the new slopes, rather than those of Eq. (5), are given as  $m'_x = (2 \sin^2 \phi - 1)m_x - \sin(2\phi)m_y$  and  $m'_y = -\sin(2\phi)m_x - (2 \sin^2 \phi - 1)m_y$ . The Monte Carlo simulations with up to half the interior particle-surface collisions treated as specular reflections showed that there is very little effect on the gas distribution except for an increase in the gas-flow rate (40%). The model therefore seems only mildly sensitive to the nature of the surfaces.

### Experimental Measurement of Gas Density

The gas distribution for a target with the same dimensions as previously described ( $a = 0.2$  mm,  $c = 0.4$  mm,  $d = 0.5$  mm, and  $L = 4$  mm) was measured. The distribution of gas from the target opening out into the region in front is characterized using a 45°-off-axis imaging system that observes the recombination light from laser-induced ionization of Xe. The imaging system employs a lens, a slit, and a photomultiplier tube, which observes recombination light from a ~500- $\mu$ m section of the laser beam. The gas target is positioned at various distances away from the location. Figure 54.28 shows the experimental setup for the measurement. The laser beam was a 1- $\mu$ m, 1-ps pulse focused with  $f/70$  optics to a peak intensity of  $2 \times 10^{14}$  W/cm<sup>2</sup>. Figure 54.29 shows the effect of the spatial

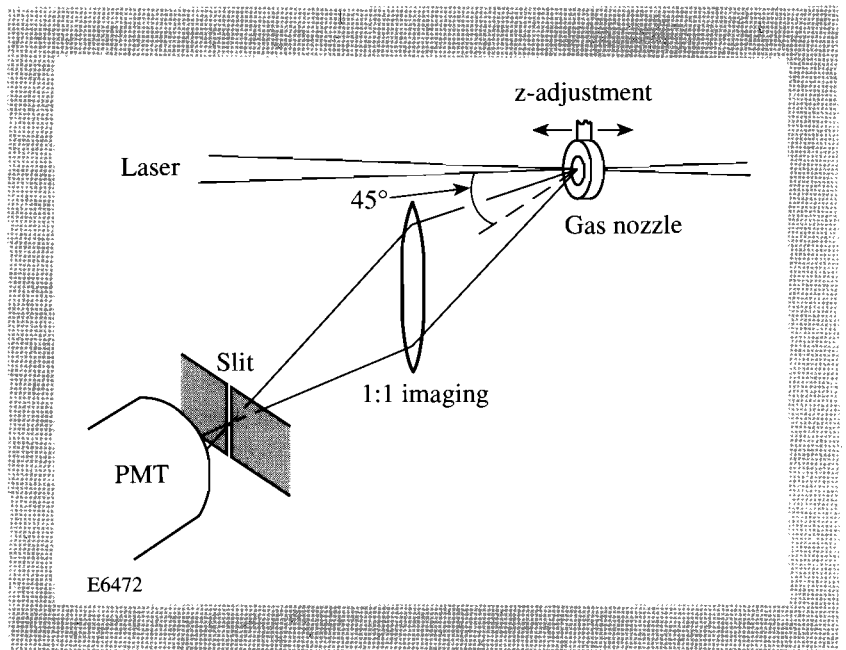


Fig. 54.28  
The experimental setup for measuring the gas density just inside the target opening and outward along the  $z$  axis.

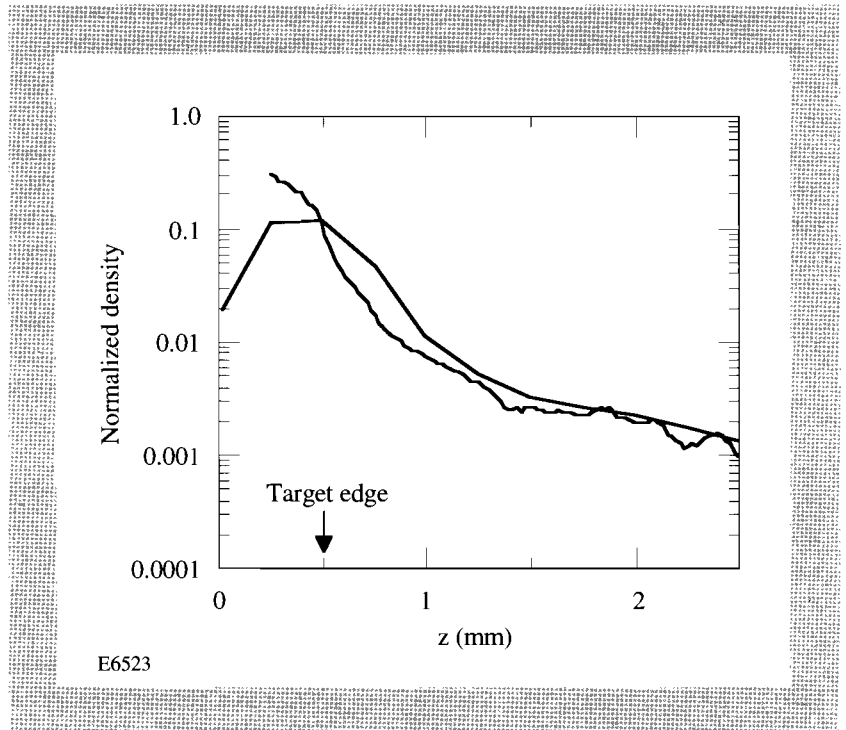


Fig. 54.29  
The calculated density of the gas as a function of  $z$  along the cylindrical axis [see Fig. 54.27(a)] compared with its convolution with the detector resolution.

resolution of the detection scheme on the calculated density. The figure shows the axial gas distribution taken from Fig. 54.27(a) along with its convolution with the experimental resolution. The measured gas density must be compared to this convolved curve to assess agreement with the calculated density.

The experimental results agree well with the theoretical predictions, especially at lower pressures. Figure 54.30 shows a comparison in absolute pressure between the predicted and measured gas density for a backing pressure of 1.7 Torr. Again, it should be noted that the results are convolved by the experimental resolution. As seen in Fig. 54.29, this causes the peak density to appear a factor of 2 below the actual value. The density was normalized by comparing the results to the signal obtained when back-filling the vacuum chamber (target removed) to a known pressure (0.1 Torr). A low pressure had to be used for calibration to avoid significant refraction of the laser before it arrived to the imaged position. It was assumed that the gas density was proportional to the square root of the instantaneous (time scale of the order of tens of nanoseconds) recombination signal.<sup>9</sup>

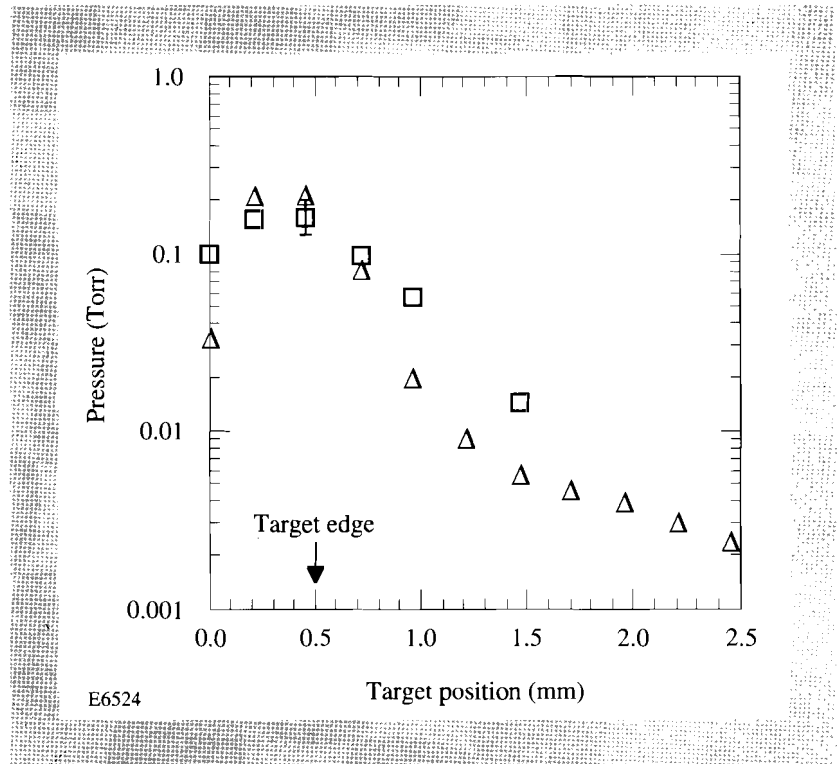


Fig. 54.30  
A comparison between the predicted- and measured-gas-density profiles for a backing pressure of 1.7 Torr.

Figure 54.31 shows the results obtained for a wide variety of backing pressures. The gas density decreases rapidly outside the target hole along the laser axis even for pressures up to ten times the molecular-flow-range cutoff. In the molecular-flow range (backing pressure of 0.5 Torr), the gas density fell by more than a factor of 10 at a distance of 1 mm from the target opening. With backing pressures of 3 Torr and 10 Torr applied to the target, the density dropped by a factor of 10 and 5, respectively, at 1 mm. These comparisons neglected the convolution effect of the experimental resolution. Inclusion of this effect

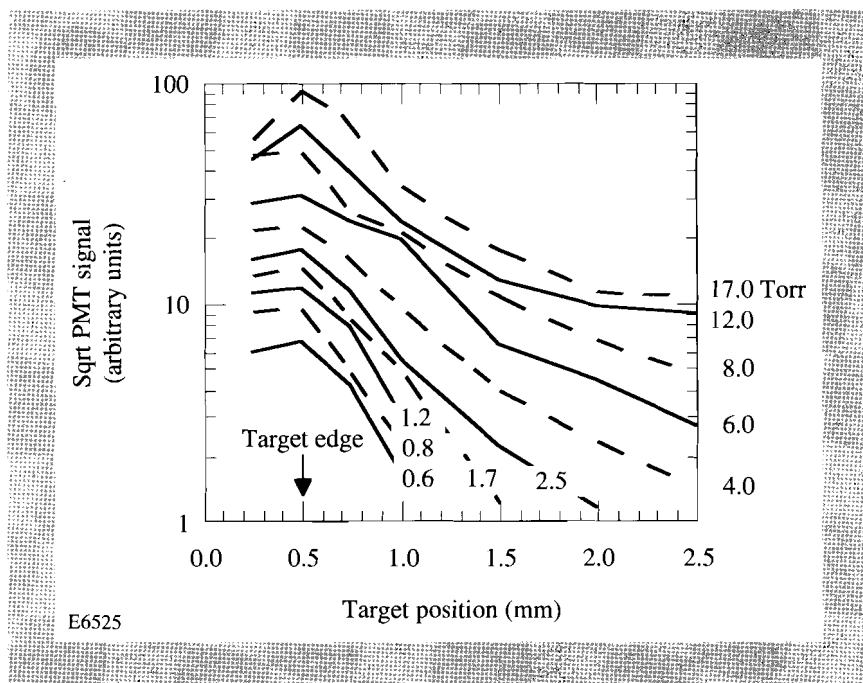


Fig. 54.31

The measured density of the gas as a function of  $z$  (the cylindrical axis) for ten different backing pressures: 0.6, 0.8, 1.2, 1.7, 2.5, 4, 6, 8, 12, and 17 Torr.

improves the contrast by about a factor of 2. The experiment thus shows that the gas target is capable of exceeding the molecular-flow regime to  $Kn$  as low as 0.1 without serious distortion of the gas distribution. It was also found that over this range of pressure the density in the target hole scales roughly with the backing pressure. Figure 54.32 shows the measured density in the target opening plotted against the backing pressure. On the log-log plot, the points should follow a slope of 1 for them to behave like pure molecular flow. The deviation from a slope of 1 shows that the gas-density profile may have a slight pressure dependence with the target operating above the molecular-flow range.

### Summary

A gas target for use in laser-atom harmonic-generation experiments has been developed. It consists of a small, cylindrical, double-ended hole through which the laser passes. Gas enters the hole along the center of its cylindrical wall and quickly disperses as it emerges out either end of the hole. The target is able to produce a narrow, low-density gas distribution that can be easily intersected by a focused laser. The distribution is well characterized both theoretically and experimentally. Recently, the target has been employed successfully in high-harmonic-generation experiments. The low-density, narrow profile of the gas is advantageous in reducing the role of phase matching and refraction in the experiment.<sup>10</sup>

To date, harmonic-generation experiments have typically employed a pulsed gas jet. The gas jet relies on the principles of viscous flow to propel gas from the orifice in a thin stream where a laser can intersect with the narrow distribution of gas. In contrast, the gas target relies on the principles of molecular flow to disperse the gas quickly once outside the central hole. Both systems are restricted to operating in their respective flow regimes to ensure the narrowest-possible gas distribution. The two systems are thus complementary in the sense that they operate in opposite pressure ranges.

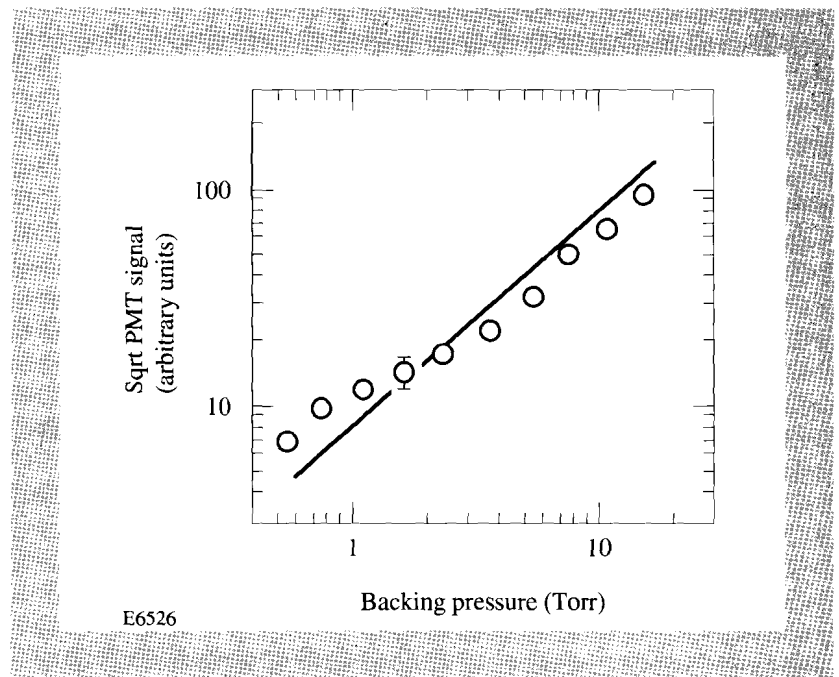


Fig. 54.32

The measured density in the target opening plotted against the backing pressure. The solid line, shown for comparison, has a slope of 1.

#### ACKNOWLEDGMENT

This work is supported by the National Science Foundation under contract PHY-9200542. Additional support was provided by the U.S. Department of Energy Office of Inertial Confinement Fusion under Cooperative Agreement No. DE-FC03-92SF19460 and the University of Rochester. The support of DOE does not constitute an endorsement by the DOE of the views expressed in this article.

#### REFERENCES

1. A. L'Huillier, K. J. Schafer, and K. C. Kulander, *J. Phys. B* **24**, 3315 (1991).
2. A. L'Huillier, K. J. Schafer, and K. C. Kulander, *Phys. Rev. Lett.* **66**, 2200 (1991).
3. Ph. Balcou and A. L'Huillier, to be published in *Physical Review A*.
4. J. F. Reintjes, *Nonlinear Optical Parametric Processes in Liquids and Gases* (Academic Press, New York, 1984).
5. A. McPherson *et al.*, *J. Opt. Soc. Am. B* **4**, 595 (1987).
6. L. A. Lompré *et al.*, *J. Appl. Phys.* **63**, 1791 (1988).
7. G. A. Bird, *Molecular Gas Dynamics* (Clarendon Press, Oxford, 1976).
8. J. F. O'Hanlon, *A User's Guide to Vacuum Technology* (Wiley, New York, 1980).
9. H. R. Griem, *Plasma Spectroscopy* (McGraw-Hill, New York, 1964).
10. D. D. Meyerhofer and J. Peatross, "Angular Distributions of High-Order Harmonics," to be published in the *Proceedings of the NATO Workshop on Super-Intense, Laser-Atom Physics*, edited by B. Piraux, Han-sur-Lesse, Belgium, 8–14 January 1993.



# PUBLICATIONS AND CONFERENCE PRESENTATIONS

## Publications

J. J. Armstrong and T. J. Kessler, "Holographic Recording of Large-Aperture, High-Efficiency, High-Damage-Threshold, Transmission Diffraction Gratings," in the *Proceedings of SPIE's 1992 International Symposium on Optical Applied Science and Engineering*, San Diego, CA, 19–24 July 1992.

C. Bamber, W. R. Donaldson, E. Lincke, and A. C. Melissinos, "Electron Acceleration Using Laser-Driven Photoconductive Switching," *Nucl. Instrum. & Methods Phys. Res. A* **327**, 227 (1993).

Y.-H. Chuang, L. Zheng, and D. D. Meyerhofer, "Propagation of Light Pulses in a Chirped-Pulse-Amplification Laser," *IEEE J. Quantum Electron.* **29**, 270 (1993).

W. R. Donaldson and L. Mu, "The Effects of Doping on Photoconductive Switches as Determined by Electro-Optic Imaging," in *Optically Activated Switching II*, edited by G. M. Loubriel (SPIE, Bellingham, WA, 1992), Vol. 1632, pp. 81–87.

E. M. Epperlein and R. W. Short, "Comment on 'Modification of Stimulated Brillouin, Saturated Raman Scattering and Strong Langmuir Turbulence by Nonlocal Heat Transport'," *Phys. Fluids B* **4**, 4190 (1993).

J. Glanz, M. V. Goldman, D. L. Newman, and C. J. McKinstrie, "Electromagnetic Instability and Emission from Counterpropagating Langmuir Waves," *Phys. Fluids B* **5**, 1101 (1993).

T. Gong, P. M. Fauchet, J. F. Young, and P. J. Kelly, "Subpicosecond Hot-Hole Dynamics in Highly Excited GaAs," *Appl. Phys. Lett.* **62**, 522 (1993).

D. Gupta, W. R. Donaldson, K. Kortkamp, and A. M. Kadin, "Optically Activated Opening Switches," in *Optically Activated Switching II*, edited by G. M. Loubriel (SPIE, Bellingham, WA, 1992), Vol. 1632, pp. 190–195.

W. Kula and Roman Sobolewski, "Measurements of Low Magnetic Field Microwave Absorption in 110-K Superconducting Bi-Sr-Ca-Cu-O Thin Films," *IEEE Trans. Appl. Supercon.* **3**, 1446 (1993).

J. C. Lambropoulos, S. D. Jacobs, S. J. Burns, and L. Shaw-Klein, "Effects of Anisotropy, Interfacial Thermal Resistance, Microstructure, and Film Thickness on the Thermal Conductivity of Dielectric Thin Films," in *Fundamental Issues in Small Scale Heat Transfer* (ASME, New York, 1992), Vol. 227, pp. 37–49.

Y. Lin and T. J. Kessler, "Raman Scattering in Air: A Four-Dimensional System Analysis," in *Design, Modeling and Control of Laser Beam Optics*, edited by Y. Kohanzadeh, G. N. Lawrence, J. McCoy, and H. Weichel (SPIE, Bellingham, WA, 1992), Vol. 1625, pp. 158–166.

R. L. McCrory, "Laser-Driven ICF Experiments," in *Nuclear Fusion by Inertial Confinement: A Comprehensive Treatise*, edited by G. Velarde, Y. Ronen, and J. M. Martinez-Val (CRC Press, Boca Raton, FL, 1993), Chap. 22, pp. 555–596.

C. J. McKinstrie and M. V. Goldman, "Three-Dimensional Instabilities of Counterpropagating Light Waves in Homogeneous Plasmas," *J. Opt. Soc. Am. B* **9**, 1778 (1992).

J. Peatross, B. Buerke, and D. D. Meyerhofer, "Sequential Ionization in  $^3\text{He}$  with a 1.5-ps, 1- $\mu\text{m}$  Laser Pulse," *Phys. Rev. A* **47**, 1517 (1993).

S. Skupsky, T. J. Kessler, S. A. Letzring, and Y.-H. Chuang, "Laser-Beam Pulse Shaping Using Spectral Beam Deflection," *J. Appl. Phys.* **73**, 2678 (1993).

R. Sobolewski, W. Xiong, and W. Kula, "Patterning of Thin-Film, High- $T_c$  Circuits by the Laser-Writing Method," *IEEE Trans. Appl. Supercon.* **3**, 2986 (1993).

## Forthcoming Publications

S. Alexandrou, R. Sobolewski, C.-C. Wang, and T. Y. Hsiang, "Subpicosecond Electrical Pulse Generation in GaAs by Nonuniform Illumination of Series and Parallel Transmission-Line Gaps," to be published in the *Proceedings of Ultrafast Electronics & Optoelectronics*, San Francisco, CA, 25–27 January 1993.

S. Alexandrou, C.-C. Wang, T. Y. Hsiang, M. Y. Liu, and S. Y. Chou, "A 75-GHz Silicon Metal-Semiconductor-Metal Schottky Photodiode," to be published in *Applied Physics Letters*.

S. Alexandrou, C.-C. Wang, R. Sobolewski, and T. Y. Hsiang, "Generation of Subpicosecond Electrical Pulses by Nonuniform Illumination of GaAs Transmission Line Gaps," to be published in the *IEEE Journal of Quantum Electronics*.

J. J. Armstrong and T. J. Kessler, "Large-Aperture, High-Efficiency Holographic Gratings for High-Power Laser Systems," to be published in the *Proceedings of SPIE's OE/LASE '93*, Los Angeles, CA, 16–23 January 1993.

C. Bamber, W. R. Donaldson, E. Lincke, and A. C. Melissinos, "A Pulsed-Power Electron Accelerator Using Laser-Driven Photoconductive Switches," to be published in the *Proceedings of the Third Advanced Accelerator Concepts Workshop*, Port Jefferson, NY, 15–19 June 1992.

R. Betti and J. P. Freidberg, "Destabilization of the Internal Kink by Energetic-Circulating Ions," to be published in *Physical Review Letters*.

X. D. Cao and C. J. McKinstrie, "Solitary-Wave Stability in Birefringent Optical Fibers," to be published in the *Journal of the Optical Society of America B*.

X. D. Cao and D. D. Meyerhofer, "Soliton Collisions in Optical Birefringent Fibers," to be published in *Optics Letters*.

W. R. Donaldson and L. Mu, "Transmission-Line Modeling of Photoconductive Switches," to be published in the *Proceedings of SPIE's OE/LASE '93*, Los Angeles, CA, 16–23 January 1993.

W. R. Donaldson and A. C. Melissinos, "A Novel High Brilliance Electron Source," to be published in the *Proceedings of the Third Advanced Accelerator Concepts Workshop*, Port Jefferson, NY, 15–19 June 1992.

H. E. Elsayed-Ali, J. W. Herman, and E. A. Murphy, "Ultrafast Laser Superheating of Metal Surfaces," to be published in the *Materials Research Society Symposia Proceedings*.

H. E. Elsayed-Ali and T. Juhasz, "Femtosecond Time-Resolved Thermomodulation of Thin Gold Films with Different Crystal Structures," to be published in *Physical Review B*.

E. M. Epperlein, "Fokker-Planck Modeling of Electron Transport in Laser-Produced Plasmas," to be published in *Laser & Particle Beams*.

E. M. Epperlein, "Implicit and Conservative Difference Scheme for the Fokker-Planck Equation," to be published in the *Journal of Computational Physics*.

P. M. Fauchet, D. Hulin, A. Mourchid, and R. Vanderhaghen, "Ultrafast Thermal Nonlinearities in Amorphous Silicon," to be published in *Ultrafast Laser Probe Phenomena in Semiconductors and Superconductors*.

P. M. Fauchet, "Picosecond Spectroscopy in Solids with a Free-Electron Laser," to be published in *Spectroscopic Characterization Techniques for Semiconductor Technology IV* (invited paper).

P. M. Fauchet and T. Gong, "Femtosecond Dynamics of Hot Carriers in GaAs," to be published in the *Proceedings of SPIE's 1992 Symposium on Compound Semiconductor Physics and Devices*, Somerset, NJ, 22–26 March 1992 (invited paper).

D. Fried, J. D. B. Featherstone, D. Glena, B. Bordin, and W. Seka, "The Light-Scattering Properties of Dentin and Enamel at 543, 632, and 1053 nm," to be published in the *Proceedings of the OSA Annual Meeting*, Toronto, Canada, 3–8 October 1993.

T. Gong, K. B. Ucer, L. X. Zheng, G. W. Wicks, J. F. Young, P. J. Kelly, and P. M. Fauchet, "Femtosecond Carrier-Carrier Interactions in GaAs," to be

published in the *Proceedings of the Eighth International Conference on Ultrafast Phenomena*, Antibes-Juan-Les-Pins, France, 8–12 June 1992.

T. Gong, L. X. Zheng, K. B. Ucer, J. F. Young, P. J. Kelly, G. W. Wicks, and P. M. Fauchet, “The Role of Carrier-Carrier Interactions in Relaxation of Hot Carriers Excited at 2 eV in GaAs,” to be published in *Physical Review B*.

T. Gong and P. M. Fauchet, “Carrier-Carrier Interactions in GaAs Investigated by Femtosecond Spectroscopy,” to be published in the *Proceedings of SPIE's OE/LASE '93*, Los Angeles, CA, 16–23 January 1993.

T. Gong, L. X. Zheng, W. Xiong, W. Kula, R. Sobolewski, and P. M. Fauchet, “Femtosecond Optical Response of Y-Ba-Cu-O Thin Films: The Dependence on Optical Frequency, Excitation Intensity, and Electric Current,” to be published in *Physical Review B*.

T. Gong, L. X. Zheng, Y. Kostoulas, W. Xiong, W. Kula, K. B. Ucer, R. Sobolewski, and P. M. Fauchet, “Ultrafast Optical and Optoelectronic Response of Y-Ba-Cu-O Thin Films,” to be published in the *Proceedings of Ultrafast Electronics & Optoelectronics*, San Francisco, CA, 25–27 January 1993.

T. Gong, L. X. Zheng, W. Xiong, W. Kula, R. Sobolewski, P. M. Fauchet, J. P. Zheng, H. W. Kwok, and J. R. Gavaler, “Femtosecond Spectroscopy of Y-Ba-Cu-O Thin Films,” to be published in the *Proceedings of the 6th Annual Conference on Superconductivity and Applications*, Buffalo, NY, 15–17 September 1992.

T. Gong, Y. Kostoulas, L. X. Zheng, W. Xiong, W. Kula, R. Sobolewski, and P. M. Fauchet, “Femtosecond Optical Nonlinearities in  $\text{YBa}_2\text{Cu}_3\text{O}_{7-x}$ ,” to be published in the *Proceedings of SPIE's OE/LASE '93*, Los Angeles, CA, 16–23 January 1993.

D. Gupta, W. R. Donaldson, K. Kortkamp, and A. M. Kadin, “Optically Triggered Switching of Optically Thick YBCO Films,” to be published in *IEEE Transactions on Applied Superconductivity*.

D. Gupta, W. R. Donaldson, and A. M. Kadin, “Fast Optically Triggered Superconducting Opening Switches,” to be published in the *Proceedings of SPIE's OE/LASE '93*, Los Angeles, CA, 16–23 January 1993.

D. Gupta, W. R. Donaldson, and A. M. Kadin, “High-Temperature Superconducting Opening Switches,” to be published in the *Proceedings of the Fifth SDIO/ONR Pulse Power Meeting '92*, College Park, MD, 17–19 August 1992.

J. W. Herman, H. E. Elsayed-Ali, and E. A. Murphy, “Time-Resolved Structural Study of Pb(100),” to be published in *Physical Review Letters*.

S. D. Jacobs, A. Lindquist, M. J. Cumbo, B. A. Feltz, W. Czajkowski, D. Golini, J. Greivenkamp, D. T. Moore, and H. M. Pollicove, “Technical Advances in Process Science Research at the Center for Optics Manufacturing,” to be published in the *Proceedings of the 7th International Precision Engineering Seminar*.

A. M. Kadin, D. Gupta, D. D. Mallory, M. Takahashi, W. R. Donaldson, and J. K. Truman, “Fabrication, Properties, and Applications of *In-Situ* Sputtered YBCO Films,” to be published in the *Proceedings of the 6th Annual Conference on Superconductivity and Applications*, Buffalo, NY, 15–17 September 1992.

H. Kim, J. M. Soares, and P. C. Cheng, "Confocal Microscopic Characterization of Laser-Fusion Target," to be published in the *Proceedings of the 39th AVS National Symposium and Topical Conferences*, Chicago, IL, 9–13 November 1992.

H. Kim and M. D. Wittman, "Interferometric Microscopy—An Overview of the Optical Characterization of Inertial-Fusion Targets," to be published in *Multidimensional Microscopy*.

L. E. Kingsley and W. R. Donaldson, "Numerical Analysis of Electric Field Profiles in High-Voltage GaAs Photoconductive Switches and Comparison to Experiment," to be published in *IEEE Transactions on Electron Devices*.

E. M. Korenic, S. D. Jacobs, J. K. Houghton, F. Kreuzer, and A. Schmid, "Nematic Polymer Liquid-Crystal Waveplate for High-Power Lasers at 1054 nm," to be published in *Applied Optics*.

W. Kula and R. Sobolewski, "Influence of the Crystalline Structure of Critical Current Density of Bi(Pb)-Sr-Ca-Cu-O Thin Films Superconducting above 100K," to be published in the *Proceedings of the 6th Annual Conference on Superconductivity and Applications*, Buffalo, NY, 15–17 September 1992.

Y. Lin and T. J. Kessler, "Raman Scattering: A Four-Dimensional System," to be published in *Applied Optics*.

## Conference Presentations

The following presentations were made at the 2nd Israeli International Conference on "High  $T_c$  Superconductivity," Eliat, Israel, 4–7 January 1993:

W. Lang, G. Heine, C. Sekirnjak, P. Schwab, X. Z. Wang, D. Bauerle, W. Kula, and R. Sobolewski, "Transport Properties of Y-Ba-Cu-O and Bi-Sr-Ca-Cu-O Thin Films in the Thermodynamic Fluctuation Range."

R. Sobolewski, "Ultrafast High  $T_c$  Optoelectronics" (Invited).

---

D. D. Meyerhofer, B. Buerke, and J. Peatross, "Sequential Ionization of  $^3\text{He}$  with 1.5-ps, 1- $\mu\text{m}$  Laser Pulses," SILAP III, Belgium, 8–14 January 1993.

---

The following presentations were made at SPIE's OE/LASE '93, Los Angeles, CA, 16–23 January 1993:

J. J. Armstrong and T. J. Kessler, "Large-Aperture, High-Efficiency Holographic Gratings for High-Power Laser Systems."

Y.-H. Chuang, T. J. Kessler, and S. Skupsky, "Laser Beam Pulse Shaping Using Dispersive Spectral Filtering."

W. R. Donaldson and L. Mu, "Transmission-Line Modeling of Photoconductive Switches."

T. Gong and P. M. Fauchet, "Carrier-Carrier Interactions in GaAs Investigated by Femtosecond Spectroscopy."

T. Gong, Y. Kostoulas, L. X. Zheng, W. Xiong, W. Kula, R. Sobolewski, and P. M. Fauchet, "Femtosecond Optical Nonlinearities in  $\text{YBa}_2\text{Cu}_3\text{O}_{7-x}$ ."

D. Gupta, W. R. Donaldson, and A. M. Kadin, "Fast, Optically Triggered Superconducting Opening Switches."

T. J. Kessler, Y. Lin, J. J. Armstrong, and B. Velazquez, "Phase Conversion of Lasers with High-Efficiency Distributed Phase Plates."

Y. Lin, T. J. Kessler, and J. J. Armstrong, "Laser System Power Balance Effects from Stimulated Rotational Raman Scattering in Air."

M. D. Skeldon and S. T. Bui, "Temporal Pulse-Width Control of a Regenerative Amplifier with Intracavity Etalons."

S. Skupsky and T. J. Kessler, "Strategies for Ultra-High Laser Uniformity Using Zero-Correlation Phase Masks."

B. Soom, X. D. Cao, H. Chen, S. Uchida, B. Yaakobi, and D. D. Meyerhofer, "Efficient  $K_\alpha$  Emission in High-Contrast, Short-Pulse, Laser-Plasma Interactions."

---

The following presentations were made at Ultrafast Electronics & Optoelectronics, San Francisco, CA, 25–27 January 1993:

S. Alexandrou, R. Sobolewski, C.-C. Wang, and T. Y. Hsiang, "Subpicosecond Electrical Pulse Generation in GaAs by Nonuniform Illumination of Series and Parallel Transmission-Line Gaps."

A. Denysenko, S. Alexandrou, C.-C. Wang, R. Sobolewski, T. Hsiang, W. R. Donaldson, and D. K. Bradley, "Dielectric Determination of a Microstrip Channel Plate by Picosecond Electro-Optic Sampling."

T. Gong, L. X. Zheng, Y. Kostoulas, W. Xiong, W. Kula, K. B. Ucer, R. Sobolewski, and P. M. Fauchet, "Ultrafast Response of Y-Ba-Cu-O Thin Films."

---

E. A. Murphy, H. E. Elsayed-Ali, and J. W. Herman, "Superheating of Bi(0001)," American Physical Society (APS), Seattle, WA, 22–26 March 1993.

---

J. Peatross and D. D. Meyerhofer, "Measurement of the Angular Distribution of High-Order Harmonics Emitted from Rare Gases," Short Wavelength V: Physics with Intense Laser Pulses, San Diego, CA, 29–31 March 1993.

#### ACKNOWLEDGMENT

The work described in this volume includes current research at the Laboratory for Laser Energetics, which is supported by New York State Energy Research and Development Authority, the University of Rochester, the U.S. Department of Energy Office of Inertial Confinement Fusion under Cooperative Agreement No. DE-FC03-92SF19460, and other agencies.

UNIVERSITY OF  
**ROCHESTER**